

# Observation of Cooper Pair Splitting and Andreev Bound States in Carbon Nanotubes

Inauguraldissertation

zur  
Erlangung der Würde eines Doktors der Philosophie  
vorgelegt der  
Philosophisch-Naturwissenschaftlichen Fakultät  
der Universität Basel

von

**Jens Oliver Schindele**  
aus Deutschland



Basel, 2014

Genehmigt von der Philosophisch-Naturwissenschaftlichen Fakultät  
auf Antrag von  
Prof. Dr. C. Schönenberger  
Prof. Dr. A. Levy Yeyati  
Dr. T. Kontos

Basel, 18.02.14

Prof. Dr. Jörg Schibler  
Dekan

# Contents

<b>1. Introduction</b>	<b>1</b>
<b>2. Carbon nanotube quantum dots</b>	<b>7</b>
2.1. Electronic structure of carbon nanotubes . . . . .	8
2.1.1. Different forms of carbon . . . . .	8
2.1.2. From graphene to CNTs . . . . .	9
2.2. Metallic contacts to Carbon nanotubes . . . . .	13
2.2.1. Schottky barriers . . . . .	14
2.2.2. Character of the chemical bonding . . . . .	18
2.2.3. Contact to metallic CNTs . . . . .	20
2.3. Carbon nanotube quantum dots . . . . .	20
2.3.1. Discrete energy spectrum . . . . .	20
2.3.2. Coulomb blockade and single electron tunnelling . . . . .	21
2.3.3. Coulomb diamonds . . . . .	24
2.3.4. Co-tunnelling and excited states . . . . .	25
<b>3. Quantum dots coupled to superconductors</b>	<b>29</b>
3.1. Superconductivity . . . . .	30
3.1.1. Basic phenomena . . . . .	30
3.1.2. Cooper pairs . . . . .	30
3.1.3. The energy gap . . . . .	32
3.1.4. Proximity effect and Andreev reflections . . . . .	36



7.1.2. Non-local spectroscopy of ABS . . . . .	97
7.2. Experiment . . . . .	98
7.2.1. Device and measurement set-up . . . . .	98
7.2.2. Local transport measurements . . . . .	100
7.2.3. Non-local conductance correlations . . . . .	100
7.3. Model . . . . .	104
7.3.1. Rate equation . . . . .	105
7.3.2. Model results and comparison with experiment . . . . .	108
7.4. Discussion and Conclusion . . . . .	109
<b>8. Summary and outlook</b>	<b>111</b>
<b>A. Detailed fabrication recipes</b>	<b>127</b>
A.1. Wafer characteristics . . . . .	127
A.2. Wafer cleaning . . . . .	127
A.3. CVD catalyst . . . . .	127
A.4. CVD growth . . . . .	128
A.5. E-beam lithography . . . . .	129
<b>B. Solution for the CPS master equation model</b>	<b>131</b>
<b>C. Additional data to Chapter 7</b>	<b>135</b>
<b>Curriculum Vitae</b>	<b>137</b>
<b>Publications</b>	<b>139</b>
<b>Acknowledgements</b>	<b>141</b>



## Introduction

*Okay, I still get nervous with it.  
And therefore, some of the younger students...*

*You know how it always is, every new idea,  
it takes a generation or two until it becomes obvious  
that there's no real problem.*

*It has not yet become obvious to me  
that there's no real problem.*

*I cannot define the real problem,  
therefore I suspect there's no real problem,  
but I'm not sure there's no real problem.*

*So that's why I like to investigate things.*

Richard P. Feynman, [1]

Decision making can be hard work, mainly because of the anticipation of possible consequences. Quantum mechanics allows the tiny objects which build up our world to be indecisive: particles may be delocalized, occupy several energy states simultaneously or possess a unidirectional magnetic moment that points in two directions at the same time. However, this schizophrenic indecisiveness, known as quantum superposition, has consequences, too; predictable consequences that are observable in experiments (e.g. as interference patterns that appear on a screen). Despite the predictive success of quantum mechanics, the counterintuitive behaviour of its objects is a hard pill to swallow and there is a native temptation to view quantum superpositions merely as mathematical constructs, instead of

something that occurs for real in nature. In other words, quantum mechanics correctly predicts measurement outcomes, but does it also provide an adequate description of the physical reality? The answer to this question is well hidden by another feature of quantum mechanics, named the wavefunction collapse. Any attempt to observe the superposition itself, instead of its consequences, will force the quantum object into a decision and destroy the signature of the indecisiveness.

In 1935 Albert Einstein, Boris Podolsky and Nathan Rosen (EPR) set up a famous *gedankenexperiment*, aiming to lift the epistemic curtain that hides the true nature of quantum superposition states [2]. Instead of just one particle, they considered two particles in a common superposition state. According to the rules of quantum mechanics a measurement on one of the particles instantaneously forces both particles into a decision, thus determining the state of the second particle. One says, the two particles are entangled. But what if the entangled particles are spatially separated from each other? EPR felt that the laws of special relativity would be broken. Special relativity seems to demand that any action on, say, particle A, can affect particle B only after a finite time has passed. Thus, if the predictions of quantum mechanics are correct – and in this respect EPR seemed to have no doubts –, it follows that the state of particle B was unambiguously determined already before the measurement on particle A was performed. In this case, the description of the particle by a superposition state reflects our lack of knowledge about the particle, rather than an inherent uncertainty of the particle's properties. Accordingly, EPR expressed their hope that quantum mechanics may emerge from some deeper theory. A theory that contains no such elements as the schizophrenic indecisiveness of quantum objects; a theory that allows a straightforward connection to the elements of an objective reality.

However, the EPR paper could not convince the community of quantum physicists. Many researchers took a viewpoint that is nicely summarized in a wording by Pascual Jourdan [3]: "Observations not only disturb what has to be measured, they produce it (...)." So why couldn't the EPR argument persuade this group of people? EPR assumed that a measurement at point A can not "in any way" disturb instantaneously a physical system at point B [2]. But this criterion is too harsh when applied to quantum mechanics. Quantum mechanics allows a physical quantity at B to instantaneously acquire a definite value by virtue of a measurement at A. After a famous Einstein quote, this non-local element of quantum mechanics is often nicknamed the spooky action at a distance ("*spukhafte Fernwirkungen*"). As an advocate of Jourdan's viewpoint one can turn the table: because the spooky actions at a distance do merely act on the elements of quantum theory, and *not* on the elements of an objective reality, they do not violate the laws of

---

special relativity.

Shortly after the publication of EPR's work Niels Bohr wrote a reply where he stated that EPR's assumption of no action at a distance can not be applied to quantum mechanics [4]. However, Bohr's point was not to disprove EPR's belief in the existence of a measurement independent reality. His point was to reveal it as a belief that can not be backed up empirically. The opposite view, as expressed by Jourdan, has to be treated as a belief in the same manner. Bohr clarifies [4]: "(...) there can be no question of any unambiguous interpretation of the symbols of quantum mechanics other than that embodied in the well-known rules which allow to predict the results (...) [of a given experiment]". Thus, we are back at our starting point. The fact that we can only observe the consequences of quantum mechanics demands abstinence with respect to statements about the true nature of quantum superpositions.

**Bell's inequality.** Bohr drew a clear line between questions that can be answered by a physics experiment and questions that must be discussed in a philosophical debate. Nevertheless, the story has a third chapter. In 1964 John S. Bell published a modification of EPR's thought experiment that allows to cross this line [5]. Bell also considered pairwise entangled particles that are separated in space. But he treated the more general case where the measurements on both particles are performed along two non-collinear measurement bases. The measurement outcome, which consists of two long columns of random numbers, is plugged into a correlation function. This correlation function is a bit nested, but to follow its construction step-by-step is no big effort. The crux is, one can calculate this correlation function also for a whole class of theories, so-called hidden variable theories that are local and deterministic. Of course one can not obtain a specific expectation value without even knowing the concrete form of the respective theory, but one obtains an upper bound for the possible values of the correlation function. As it turns out, the quantum mechanical expectation value lies above this threshold. Thus, all the discomfort EPR had with quantum mechanics boils down to the question if one number is larger than another.

**What does it all mean?** One feature of the Bell test is, that it is sufficiently abstract to shrug of almost any attempt to develop an intuition for it. If Bell's inequality is violated in a thoroughly conducted experiment, it means there can't be any deterministic theory that is based on local hidden variables. One can fairly assume that EPR had exactly this type of theory in mind when they developed their *gedankenexperiment*. Ironically, it is an adaptation of their own experiment that allows to falsify the hypothetical

existence of such a theory.

Of course, there was an enormous effort to carry out the thought experiment in an actual laboratory. In the early 1980s Alain Aspect and co-workers succeeded to violate Bell's inequality with polarization-entangled photon pairs [6]. Later experiments also violated Bell's inequality with massive beryllium ions [7] and in a solid-state environment with superconducting Josephson phase qubits [8]. Experiments with photons became very well developed (entangled photons have, for example, been sent from the Canary Island of La Palma to a telescope in Tenerife [9]). However, a Bell test with individual electrons, the fundamental particles of electronics, is still missing. Moreover, researchers found potential applications for entangled particles in quantum cryptography [10], in quantum teleportation [11] and in quantum computing [12, 13], where entanglement is the fuel that speeds up algorithms [14].

### **What has it to do with this thesis?**

The initial motivation for this PhD project was to build an electronic device that converts an incoming electrical current into a continuous stream of pairwise entangled electrons. This device is called a Cooper pair splitter and its basic idea is to exploit the pairwise entanglement that naturally occurs in the ground state of a conventional superconductor. Such an on-chip source of entanglement can potentially be used to perform a Bell test with the spins of individual electrons, or it could play a key role in a future quantum processor, where it could be used to synchronize the quantum circuits or to teleport a qubit across the chip. Not that I believe a Bell test with electrons would convince a hard-boiled sceptic of the impossibility to describe nature by a local hidden variable theory, or at least ease somebodies discomfort with quantum mechanics. My pessimistic temper also has serious doubts that such a device will be implemented in some practical application sometime soon. My motivation was to become a quantum engineer. Somebody who creates and manipulates these strange superposition states *on purpose*, instead of worrying about their true ontological nature. In the end, all measurements in modern laboratories are converted into electrical signals. Hence, there is a special appeal to directly use individual electrons in an electronic circuit as quantum objects to play with.

In practice, of course, it turns out rather challenging to control and manipulate electrons (and Cooper pairs) to the degree that we would like to. The thing is that every advantage also poses a disadvantage, eventually. In principle it is rather simple to control electrons. Unlike photons they carry a charge and therefore they react to electric fields. At the same time, this makes electrons very sensitive to all kind of disorder and inhomogeneities

---

that are usually present in solid-state materials. We chose to guide the electrons through carbon nanotubes (CNTs). CNTs are a very unique material: tiny cylinders, about  $\sim 0.5 - 3$  nm in diameter and up to several tens of micrometers long, that are entirely made of carbon atoms ordered in a very simple hexagonal structure. From a CNT one can easily form a quantum dot (QD), the key element of all devices in this thesis. One can impose tunnel barriers, which define a QD, simply by the patterning of metal electrodes on the CNT. The electrodes at the same time act as source-drain contacts, which allows to couple QDs to superconductors – an endeavour that is much more challenging in other material systems. The drawback of this simplicity is that it is very hard to gain control over these tunnel barriers. This list of advantages and disadvantages could surely be continued, but we leave it to the amiable reader to add some more items...

The thesis is structured as follows. In Chapter 2 we introduce the basics of CNT based QDs and in Chapter 3 we discuss some of the phenomena that can occur when superconducting electrodes are connected to a QD. In Chapter 4 we explain how the devices are fabricated and introduce the measurement set-up. Chapter 5 is dedicated to approaches to improve the device quality. In this chapter we also present some measurement results from which we judge the quality of the devices. The main results of this thesis are contained in Chapter 6 and Chapter 7. In Chapter 6 we demonstrate Cooper pair splitting (CPS) in a CNT with near ideal efficiency. In Chapter 7 we discuss a device with a very similar geometry, but the device is operated in a coupling regime that is not suitable for high CPS efficiencies. Instead this distinct coupling regime allows to observe Andreev bound states (ABSs) and probe them by local and non-local conductance measurements. An ABS is a special type of energy level that emerges from the superconducting proximity effect. The ABS can be viewed as a state which entangles a QD with a superconductor: the system is in a superposition of a state where a Cooper pair occupies the QD and a state where this Cooper pair is in the superconductor. Of course this configuration allows not to separate the entangled objects. Nevertheless, the physics we encounter is quite beautiful and closely related to the concepts of entanglement and superposition. Chapter 8 briefly summarizes the results and provides an outlook.



## Carbon nanotube quantum dots

Quantum dots (QDs) are quasi zero dimensional electronic elements: solid state systems that are shrunk so small that quantum mechanics allows only certain standing wave solutions for the wave function of an electron (or a hole) confined inside. Consequently QDs possess a discrete energy spectrum that gave them their nickname *artificial atoms* [15]. However, in contrast to real atoms QDs can be connected easily to source and drain electrodes, as well as to electrostatic gates that control the dot potential. In such a transistor-like geometry the energy spectrum of the QD can be probed by charge transport measurements at low temperatures (typically  $\sim 10$  mK to  $\sim 10$  K).

QDs can be realized in many different material systems, e.g. two dimensional electron gases in semiconductor heterostructures, semiconducting nanowires, self-assembled systems, graphene or carbon nanotubes (CNTs). Many QD properties can be regarded as universal, while some others depend on the host material. A prime example for a universal QD property is Coulomb blockade: any QD can be seen as a small capacitive island that requires a charging energy  $e^2/C$  for the addition of one electron. On the other hand, shell filling effects or spin orbit interactions are determined by the physics in the host material.

The topic of this thesis are low temperature transport experiments carried out with CNT QDs. This chapter gives a brief introduction into this field. We first discuss CNTs and their electronic structure (Sec. 2.1). In Sec. 2.2 we turn to the contact formation between metals and CNTs. Section 2.3 is devoted to CNTS QDs.

## 2.1. Electronic structure of carbon nanotubes

### 2.1.1. Different forms of carbon

Carbon is a particular versatile material. Its atoms have four electrons in their outer shells which are able to bond to either two, three or four other atoms. The flexibility of the valence electrons also results in a wealth of carbon allotropes. Besides the two main crystallographic configurations – diamond and graphite – more exotic forms of carbon were discovered, the most prominent ones being graphene, carbon nanotubes and  $C_{60}$  bucky-balls (Fig. 2.1).

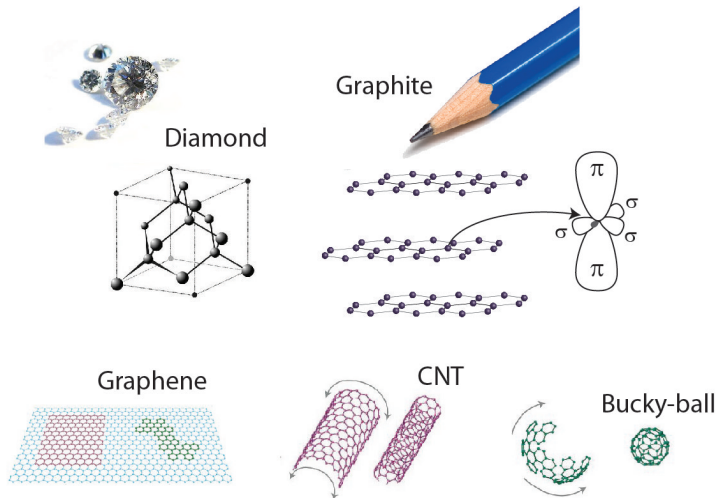


**Figure 2.1.:** Different forms of carbon: Although diamond and graphite are both composed from carbon they have very different properties due to the different crystal lattices. that result from have very different properties adapted from [16, 17].

Although these materials consist all of carbon, their properties, emerge from the underlying atomic lattice and differ strongly. Diamond, for example, is extremely hard and a large band gap insulator. Responsible for these properties is the diamond lattice, in which all four valence electrons are involved in the formation of strong  $\sigma$ -bonds with a rather localized electron wavefunctions. Graphite, in contrast, is a very soft material with an electrical conductivity comparable to that of some metals. In graphite

each carbon atom forms only three  $\sigma$ -bonds that lie within one plane. This  $sp^2$  hybridization results in a layered structure where each C atom leaves one residual  $\pi$ -electron in the  $p_z$  orbital (Fig. 2.1). Electrical conductivity emerges from the overlapping orbitals of weakly localized  $\pi$ -electrons and the weak binding between different layers accounts for the softness of graphite (a property frequently used when writing with a pen on a paper).

When a single layer of graphite is sufficiently isolated from its environment – be it in the laboratory or just in a thought experiment – it is referred to as graphene. The history of graphene started in 1947, when P.R. Wallace used the theoretical concept as an approximation to calculate the electronic band structure of graphite [18]. A CNT can be thought of as a single graphene sheet rolled up into a seamless cylinder.  $C_{60}$  bucky-balls are their spherical analogues.

### 2.1.2. From graphene to CNTs

The concept of graphene is the natural starting point when one strives to understand the electronic structure of CNTs [19] (or  $C_{60}$  bucky-balls [20]). The angle between two  $\sigma$ -bonds in the graphene sheet is  $120^\circ$ , leading to the characteristic hexagonal honeycomb lattice, shown in Fig. 2.2(a). The graphene unit cell contains two atoms (A and B) and the primitive vectors  $\mathbf{a}_1$  and  $\mathbf{a}_2$  span the lattice. The first Brillouin zone and the reciprocal lattice vectors  $\mathbf{b}_1$  and  $\mathbf{b}_2$ , defined by  $\mathbf{a}_i \mathbf{b}_j = 2\pi \delta_{ij}$ , are shown in Fig. 2.2(b). The band structure of graphene can be calculated by applying the tight binding method to the overlapping wavefunctions of neighbouring  $\pi$ -electrons [18, 21]. Figure 2.2(c) shows the result of this calculation, which we use as a starting point of our discussion. The conduction and the valence band touch at the 6 corners of the Brillouin zone, labelled K and K', making graphene a semi-metal with zero density of states at the Fermi level. Close to the touching points the bands have the shapes of cones and the dispersion relation can be written as

$$E(\mathbf{k}) = \pm \hbar v_F |\mathbf{k}|, \quad (2.1)$$

where  $\mathbf{k}$  is measured from the K (K') point at the center of the respective cone and  $E$  is measured with respect to the Fermi energy.  $v_F$  is the Fermi velocity, which is about  $8.2 \times 10^5$  m/s [22]. Due to their linear dispersion, which mimics the behaviour of relativistic photons, the cones are often called Dirac cones. Only one third of each Dirac cone lies within the the first Brillouin zone: we can consider two complete cones, one at K and one at K', instead of six partial cones. These two irreducible cones add a new degree of freedom called valley or iso-spin: the wavevector  $\mathbf{k}$  can be defined in the K or the K' valley. The two states with wavevectors  $\mathbf{k} + \mathbf{K}'$  and

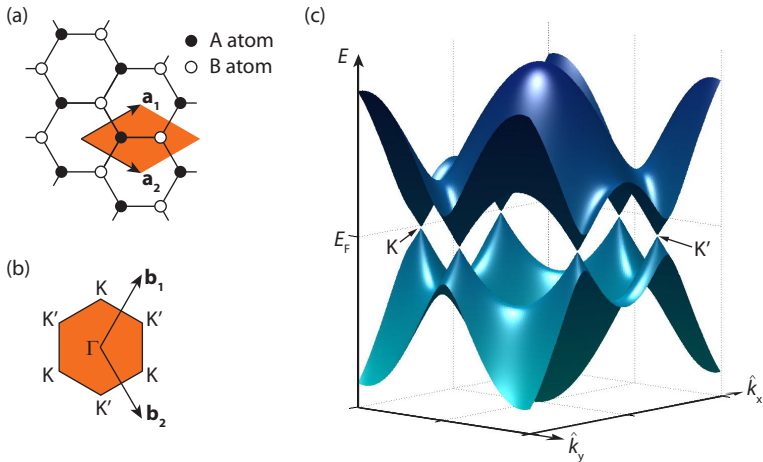


**Figure 2.2.:** (a) The hexagonal lattice of graphene in real space. The primitive lattice vectors  $\mathbf{a}_1$  and  $\mathbf{a}_2$  span the unit cell which contains two atoms labelled A and B. (b) The first Brillouin zone for the graphene lattice. The vectors  $\mathbf{b}_1$  and  $\mathbf{b}_2$  point to the reciprocal lattice points. The reciprocal lattice vectors also connect the three corners labelled K and the three corners labelled K'. Therefore only two of the six corners are distinguishable. (c) Band structure of graphene calculated from a standard tight binding model (see e.g. [18, 19, 21]). The low-energy properties of graphene and CNTs can sufficiently be understood by considering two Dirac cones around the points K and K'.

$\mathbf{k} + \mathbf{K}$  are inequivalent but energetically degenerate. Here  $\mathbf{K}$  ( $\mathbf{K}'$ ) denotes the vector pointing from  $\Gamma$  to K ( $\mathbf{K}'$ ).

To calculate the band structure of a CNT one rolls a graphene sheet into a seamless cylinder by imposing additional periodic boundary conditions on the electron wavefunction. In this so-called zone folding approximation the momentum component along the CNT,  $k_{\parallel}$ , remains unaffected, while the component in circumferential direction,  $k_{\perp}$ , becomes quantized and can only change in steps given by

$$\Delta k_{\perp} \pi d = 2\pi, \quad (2.2)$$

where  $d$  is the tube diameter. This condition cuts 1-dimensional subbands out of the Dirac cones:

$$E^l(k_{\parallel}) = \pm \hbar v_F \sqrt{(k_{\parallel})^2 + (k_{\perp}^l)^2}. \quad (2.3)$$

Here  $l \in \mathbb{Z}$  labels the respective subband with the quantized momentum component  $k_{\perp}^l = k_{\perp}^0 + l\Delta k_{\perp}$ . The tiny diameters of the nanotubes pushes

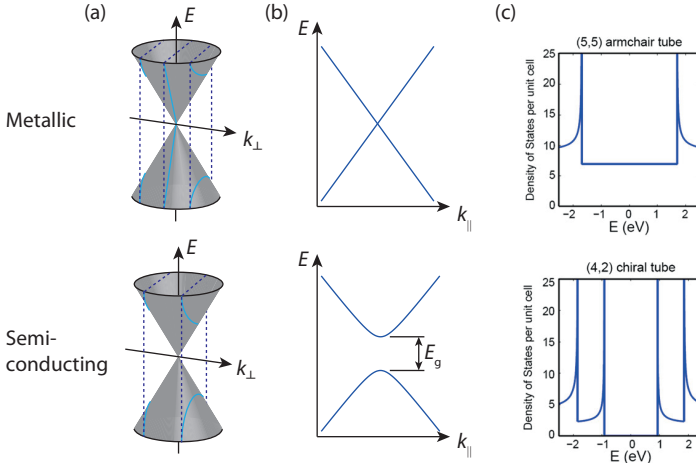


**Figure 2.3.:** (a) The quantization of the wavevector  $k_{\perp}$  cuts slices out of the Dirac cones. When such a slice contains the tip of the cone, where conduction and valence band meet, the CNT is metallic (upper panel), otherwise the CNT is semiconducting (lower panel). (b) 1-dimensional band structure of CNTs. Shown is the lowest 1D subband for the metallic and semiconducting case. (c) Density of states per unit cell for a metallic (5,5) and a semiconducting (4,2) CNT from [23]. The peaks are van Hove singularities when the energies where a higher 1D subband becomes available.

the excitation energy of these subbands to the eV range. Already at room temperature only the lowest 1D subband ( $l = 0$ ) is populated.

### Metallic and semiconducting CNTs

It turns out that there are two types of CNTs: those where the lowest 1D subband cuts through the tip of the Dirac cone,  $k_{\perp}^0 = 0$ , and those where the cut misses the tip of the cone and the circumferential wavevector retains a finite value,  $k_{\perp}^0 \neq 0$ , even for  $l = 0$ . The CNTs with  $k_{\perp}^0 = 0$  are classified as metallic, whereas those with  $k_{\perp}^0 \neq 0$  are semiconductors with a band gap  $E_g = 2\hbar v_F k_{\perp}^0$ . Figure 2.3 illustrates the two cases.

To understand the origin of these two different types we have to be more explicit in the formulation of the periodic boundary conditions. By multiplying the lattice vectors with integer numbers  $m$  and  $n$  a chiral vector  $\mathbf{C} = n\mathbf{a}_1 + m\mathbf{a}_2$  can be defined [Fig. 2.4(a)]. The chiral vector describes the direction along which the CNT is rolled up, i.e.  $|\mathbf{C}| = \pi d$ . The indices  $m$  and  $n$  uniquely determine the structure of a CNT. Figure 2.4(b) shows three examples: tubes with  $n = m$  are called armchair (C–C bonds lie par-

allel to  $\mathbf{C}$ ), those with  $n = 0$  or  $m = 0$  are called zigzag (C–C bonds lie perpendicular to  $\mathbf{C}$ ), all other cases are denoted chiral.

The chiral vector can be conveniently used to express the periodic boundary conditions for the electron wavefunction:

$$\psi(\mathbf{r} + \mathbf{C}) = e^{i\mathbf{C}(\mathbf{k}+\mathbf{K})}\psi(\mathbf{r}) = \psi(\mathbf{r}). \quad (2.4)$$

The scalar product  $\mathbf{C} \cdot \mathbf{K}$  can only become zero if  $(n - m) = 3p$ , where  $p$  is a integer number [19]. This condition is graphically illustrated in Fig. 2.4(a), where it holds for all chiral vectors that connect two atoms with the same color. If  $\mathbf{C} \cdot \mathbf{K}$  can become zero, then  $k_{\perp}^0 = 0$  is also a solution to the boundary conditions and the tube is metallic. Those chiral vectors in Fig. 2.4(a) that map two atoms with different colors onto each other imply  $(n - m) \neq 3p$ . In this case the wavefunction at the K point acquires a phase difference  $\pm \frac{2\pi}{3}$  between the points  $\mathbf{r}$  and  $\mathbf{r} + \mathbf{C}$ . The momentum vector has to be displaced by  $k_{\perp}^0$  from the K point to fulfil the boundary conditions and the CNT becomes semiconducting. The displacement from the K point is given by  $\pi dk_{\perp}^0 = \pm \frac{2\pi}{3}$  (the sign depends on the values of  $n$  and  $m$ ). This condition implies that the energy gap of a semiconducting CNT, which can be calculated from Eq.(2.3), is inversely proportional to the tube diameter:

$$E_g = 2 \cdot \hbar v_F k_{\perp}^0 = \frac{4\hbar v_F}{3d} \approx \frac{0.7 \text{ eV}}{d[\text{nm}]}. \quad (2.5)$$

An early triumph in CNT research was the experimental confirmation of the connection between CNT chirality and electronic structure by means of scanning tunnelling microscopy (STM). Wilder, *et al.* [25] could extract the chiral indices of CNTs from STM images and correlate it with the density of states, also measured by STM. Later on, transport measurements on insulating substrates showed that also nominally metallic CNTs have small energy gaps with a magnitude of  $\sim 10 - 100$  meV [26, 27]. These additional gaps are often attributed to mechanical perturbations, e.g. due to strain, twists or curvature, which will displace  $k_{\perp}^0$  from the Dirac point [19]. In a simple non-interacting picture one would expect that it is possible to realign  $k_{\perp}^0$  with the K point by applying a magnetic field parallel to the CNT (the electrons acquire an additional Aharonov-Bohm phase which adds to the phase  $\mathbf{C} \cdot \mathbf{K}$  and shifts the position of the cuts  $k_{\perp}^l$  [19]). However, Deshpande *et al.* [27] found that this non-interacting picture fails and it is not possible to close the small energy gaps by applying parallel  $B$  fields. Instead the authors propose that a Mott insulating state forms around half filling in nominally metallic tubes.

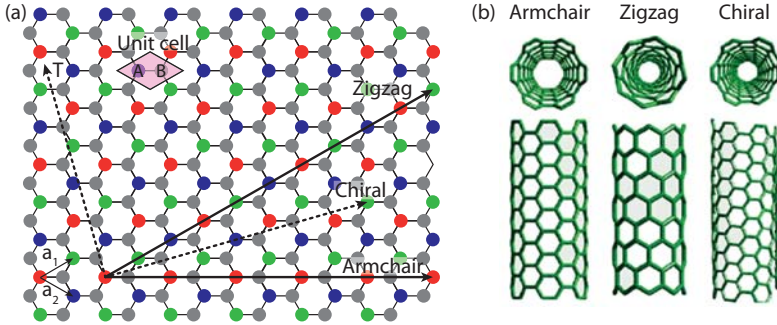


**Figure 2.4.:** (a) The structure of CNTs is classified by the chiral vector  $\mathbf{C} = n\mathbf{a}_1 + m\mathbf{a}_2$ . The color coding of the A atoms visualizes the condition  $n - m = 3p$  (where  $n, m$  and  $p$  are integer numbers) for metallic CNTs. Chiral vectors connect two atoms with the same colors wrap the graphene into a metallic CNT (1/3 of all cases). Chiral vectors that connect two atoms with different colors produce semiconducting CNTs (2/3 of all cases). The same argument can be made for the B atoms. Adapted from reference [24]. (b) Examples of the different CNT structures. Image from reference [23].

### Mean free path

The mean free path in CNTs can be up to  $\sim 10 \mu\text{m}$  for metallic CNTs and up to several  $\mu\text{m}$  for semiconducting CNTs [24]. These long mean free path are also rooted in the 1-dimensionality of the CNT: since electrons can only scatter backward or forward the scattering probability is lower than in 3D where scattering in all directions is allowed [23]. The measurements in this thesis were performed at low temperatures and on rather short devices ( $\sim 300 \text{ nm}$ ). These conditions allow to treat the CNTs as ballistic conductors.

## 2.2. Metallic contacts to Carbon nanotubes

To use CNTs as building blocks in electronic devices the CNTs have to be connected to source and drain contacts. The "traditional" way to contact a CNT uses a lithographically patterned resist mask through which a metallic film is deposited onto the CNT by physical vapour deposition (usually evaporation or sputtering). For a fully transparent metal-CNT interface a contact resistance of  $h/4e^2$ , corresponding to the four conductance channels provided by spin and valley degeneracy, is expected. However, real devices often exhibit two-terminal resistances above this ideal value due to the formation of tunnel barriers at the metal-CNT interface. For transport experiments at low temperatures these contact barriers prove very useful:

they confine the charge carriers along the CNT segment between two contacts, enabling the fabrication of quantum dots simply by the patterning of source and drain electrodes. At the same time, these naturally formed tunnel barriers are also a major obstacle for the fabrication of more advanced quantum electronic devices: they provide too little control over contact resistance.

Unfortunately, a thorough understanding of the metal-CNT contact has not evolved yet [23]. In the following we discuss some of the factors which are believed to determine the contact resistance. Section 2.2.1 focuses on Schottky barriers, which can form at the interface between a metal and a semiconducting CNT. In Sec. 2.2.2 we discuss the influence of the chemical bonding between CNT and metal. In Sec. 2.2.3 we briefly comment on the contact formation to metallic CNTs. Another crucial factor, the cleanliness of the metal-CNT interface which is certainly a prerequisite for a "good" contact, is discussed in Sec. 4.2 among the device fabrication.

### 2.2.1. Schottky barriers

#### The Schottky-Mott rule for barrier heights

When a metal is placed in contact with a semiconductor electrons flow across the interface to balance the mismatch between the different Fermi levels of both materials. This process is associated with an electric field across the metal-semiconductor interface and builds up a surface charge at the interface. The high carrier density in the metal allows to screen electric fields on typical length scales below one Ångstrom. Hence, the field penetration into the metal might be neglected. In contrast, the considerably lower carrier density in semiconductors will allow the electric field to enter: In the region close to the interface positive charges accumulate, given that metal work function  $\phi_m$  is larger than  $E_{vac} - E_F$  of the semiconductor, as shown in Fig. 2.5(a). This charge layer at the interface bends the energy bands of the semiconductor, constituting a so-called Schottky barrier for the injection of electrons and holes [Fig. 2.5(b)]. The barrier height  $\phi_{SB}$  is given by the Schottky-Mott rule [28]. For electron injection the Schottky-Mott rule states

$$\phi_{SBe} = \phi_m - \chi, \quad (2.6)$$

where  $\chi$  is the electron affinity of the semiconductor, i.e. the energy difference between the bottom of the conduction band and vacuum level. The corresponding barrier height for holes is given by

$$\phi_{SBh} = I - \phi_m, \quad (2.7)$$

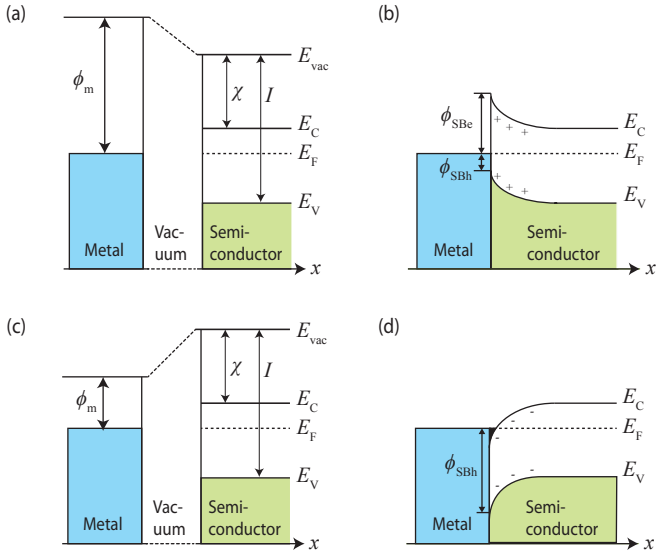


**Figure 2.5.:** (a) Energy band diagram of a metal and a weakly n-doped semiconductor. The different distances between Fermi level,  $E_F$ , and vacuum level,  $E_{vac}$ , cause a potential drop across the vacuum gap. (b) When contact is made the Fermi levels physically equilibrate. The energy levels are bent until the vacuum levels of both materials match. In the depicted case Schottky barriers for electrons and holes are formed. (c,d) For  $\phi_m < \chi$  a Ohmic contact to the conduction band forms. The black area indicates free electrons at the interface.

where  $I = \chi + E_g$  is the ionisation potential of the semiconductor which corresponds to the energy gain when a vacuum electron is added to the top of the valence band.

When the Fermi level of the metal lies in the band gap of the semiconductor a Schottky barrier for the injection of electrons and holes is formed, i.e.  $\phi_{\text{SBe}} > 0$  and  $\phi_{\text{SBh}} > 0$  as depicted in Fig. 2.5(b). The case  $\phi_m < \chi$  is illustrated in Fig. 2.5(c). The Fermi level of the metal lies above the conduction band and  $\phi_{\text{SBe}}$  becomes negative. The conduction band is bent below the Fermi edge of the metal. Free electrons enter a thin layer at the semiconductor surface and provide an Ohmic contact to the conduction band [Fig. 2.5(d)]. However, the interface electrons locally fill the empty states in the valence band. Consequently there is a large Schottky barrier for the injection of holes. For metals with a work function larger than ionisation potential of the semiconductor the argument is inverted, resulting in a p-type behaviour with Ohmic contact to the valence band and a large barrier to the conduction band.

For conventional semiconductors the Schottky-Mott rule usually fails [28]. The barrier height depends much weaker on the metal work function than expected and a considerable barrier is formed even if  $\phi_m < \chi$  or  $I < \phi_m$ . The deviations from the Schottky-Mott rule are commonly explained by chargeable defects at the semiconductor surface which pin the Fermi level of the metal inside the band gap [28]. For 1-dimensional semiconductors, such as a CNTs, electrostatic models predict that Fermi level pinning plays only a minor role in the contact formation [29, 30] and that the Schottky-Mott rule should apply.

### Schottky barriers in CNTs

In the absence of chemical doping the Fermi level of the CNT lies in the middle of the band gap and the barrier heights are given by

$$\phi_{\text{SBe}} = \phi_m - (\phi_{\text{CNT}} - E_g/2) \quad (2.8)$$

and

$$\phi_{\text{SBh}} = (\phi_{\text{CNT}} + E_g/2) - \phi_m, \quad (2.9)$$

where  $\phi_{\text{CNT}}$  and  $E_g$  denote the work function and the band gap of the CNT.  $\phi_{\text{CNT}}$  was measured by photoemission spectroscopy [31] and derived from scanning Kelvin probe measurements [32]. It lies in the range  $\phi_{\text{CNT}} \approx 4.7 - 4.8 \text{ eV}$ , which is about  $0.1 - 0.2 \text{ eV}$  larger than the work function of Graphite. The band gaps of semiconducting CNTs vary with the tube diameter,  $E_g \propto 1/d$ , and are statistically distributed with typical values between  $0.4$  and  $2.0 \text{ eV}$  [25, 33]. However, smaller values  $E_g \approx 0.1 - 0.3 \text{ meV}$

have also been reported [34], implying a continuous crossover from the gap size of semiconducting CNTs with large diameter to quasi-metallic tubes with small diameters, for which typical energy gaps from 10 to 100 meV were found [27].

Numerous publications support the validity of the Schottky-Mott picture for metal-CNT contacts. In 2002 an IBM group proposed that CNT devices operate as unconventional Schottky barrier FETs whenever there is a substantial Schottky barrier at the contact [35]. The switching of the transistor primarily occurs because the electric field tunes the width of the Schottky barrier until tunnelling through the barrier sets in. This mechanism, which differs from conventional FETs where the switching is tuned by the channel conductance and not by the contact resistance, allowed to explain many experimental findings, such as the differences between n and p-channel conductances. In 2003 the group of Hongjie Dai succeeded to fabricate near-ideal CNT FETs with Ohmic contact to the p-channel by using palladium ( $\phi_{\text{Pd}} \approx 5.1 \text{ eV}$ ) as contact material [36]. In 2005 the same group established rhodium ( $\phi_{\text{Rh}} \approx 5.0 \text{ eV}$ ) as alternative material for p-type Ohmic contacts [37]. The fabrication of CNT transistors with Ohmic contacts to the n-channel remained a challenge for some more years. In 2007 the group of Lian-Mao Peng succeeded with scandium ( $\phi_{\text{Sc}} \approx 3.3 \text{ eV}$ ) as contact material [38]. Shortly afterwards the same group found that the much cheaper material yttrium also forms Ohmic contacts to the conduction band [39].

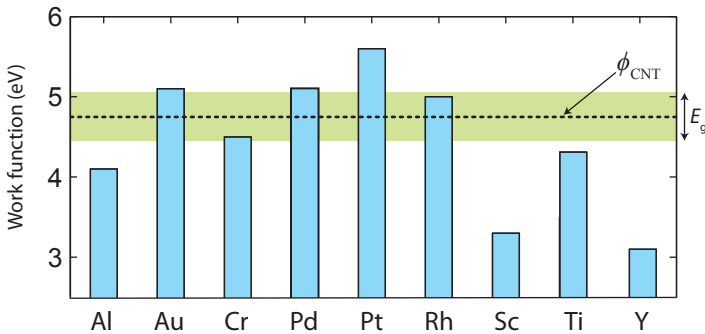


**Figure 2.6.:** Work functions of selected metals [36, 38–40]. The dashed line corresponds to the CNT work function. The green corridor exemplifies the band gap of a CNT with  $E_g = 0.5 \text{ eV}$ .

Figure 2.6 lists the tabulated work functions of selected metals and compares them to the CNT work function. The green corridor corresponds to

the band gap of a tube with  $E_g = 0.5$  eV, which is a realistic value for CNT with large diameter. According to the Schottky-Mott rule all metals with work functions that lie either above or below the band gap should make Ohmic contact to the CNT.

This is unfortunately not the case. Platinum, for example, has a significantly higher work function than palladium, but makes only very poor electrical contact to CNTs [36]. Aluminium should make a nice n-type contact, but the on-currents of aluminium contacted CNT transistors are on average about two orders of magnitude lower than the on-currents of palladium devices [33]. According to its work function titanium should form n-type contacts. But in practice Ti contacts often yield ambipolar characteristics [see Fig. 5.5(a)] or even p-type doping [34]. Therefore, the Schottky-Mott rule can't be the only factor that determines the contact resistance.

The deviations from a simple Schottky-Mott behaviour might be attributed to deviations between the tabulated work functions and the real work functions, at least to some extent. In the fabrication process the metal work functions can be modified, e.g. due to adsorption [32] or by oxidation from water residues on the substrate. The latter mechanism might be especially important for many of the highly reactive metals which could potentially make n-type contacts (Ti, Al, etc.). However, chemical doping and the underlying mechanisms remain a controversially debated issue: most authors explain the device sensitivity to environmental changes by modifications of the metal work function [32, 35, 36, 41], but Chen and Fuhrer challenge this view and claim that in some cases doping of the CNT is the relevant mechanism [42]. Non-controversial is the experimental fact that CNT transistors are sensitive to the ambient environment, which sometimes even results in a change from p-type to n-type behaviour as the device is brought from air into vacuum [41]. However, in many cases (e.g. Pt or Al) the discrepancies between the Schottky-Mott picture and the experimental reality is so large that they can hardly be explained by chemical doping.

### 2.2.2. Character of the chemical bonding

Metals with very similar work functions yield CNT devices with very different contact resistances. This fact, which we briefly discussed above, motivated a number of first principle studies that go beyond simple electrostatics [43–47]. These studies use density functional theory to calculate the charge distribution at the metal-CNT contact on a microscopic scale. The computationally demanding calculations highlight the importance of the metal's wetting properties and of the electronic hybridization between the metal and the CNT.

Vitale *et al.* showed that Al forms only few bonds to the cylindrical CNT

surface, while Pd atoms arrange themselves in a way that maximizes the number of possible bonds, resulting in a uniform wetting of the CNT [45]. Similar results were obtained in Ref. [44], where a simulated Au contact barely formed bonds to the CNT, whereas Pd formed many bonds. Vitale *et al.* also investigated the contact formation to the open end of a CNT cylinder. In this case they found that Al binds well to the CNT. The abruptly terminated CNT provides dangling bonds to which Al can bind and a continuous metal cap was formed in the simulation. This suggests that some metals (e.g. Al and Rh) need dangling bonds or other high-energy defects to bind to the CNT, while other metals (e.g. Pd and Ti) are able to bind to the pristine CNT surface. The nucleation of Rh at defect sites was experimentally observed by transmission electron microscopy in one of the few experimental attempts to study contact formation to CNTs [48]. The authors also found that the introduction of additional defects by an oxygen plasma lead to smaller Rh clusters and a more uniform coating of the CNT.

Vitale *et al.* showed that not only the number of bonds, but also their chemical character is crucial for the contact properties [45]: The Pd–C–C angle is about  $90^\circ$ . Hence the Pd atoms do not perturb the  $sp^2$  configuration of the CNT. In C atoms in  $sp^2$  configuration can still provide delocalized  $\pi$ -electrons, which are responsible for the electrical conductivity of the CNT. In contrast, the formed Al bonds have an Al–C–C angle of  $\sim 110^\circ$ , which is not compatible with a pure  $sp^2$  configuration. The involved C atom rehybridizes into  $sp^3$ , implying the formation of a  $\sigma$ -like bond which is strongly localized and acts as potential barrier rather than contributing to the electrical conductivity.

Some results also suggest that CNT sections covered by Pd or Ti become severely distorted in their spatial and electronic structure [43, 46, 47]. Interestingly these models predict that the CNT bandgap becomes filled below the metal contact, turning the CNT locally from a semiconductor into a metal. In this picture the contact resistance of CNT devices is determined by Schottky-barriers that form between a metallic and a semiconducting segment of the CNT. However, this view seems to contradict the experimental results by Franklin and Chen [49], who report that the contact resistances of Pd-contacted CNT transistors scale with the contact area according to the simple relation

$$2R_{\text{contact}} = \frac{h}{4e^2} + \frac{2\rho}{L_c d}. \quad (2.10)$$

where  $L_c$  is the length of the metal contact and  $d$  is the diameter of the CNT and  $\rho$  is the contact resistivity in addition to the quantum resistance, which the authors extract from fits to be  $346 \text{ k}\Omega \text{ nm}^2$ . These results indicate that the charge carriers propagate at least several tens of nanometers under the metal contact.

### 2.2.3. Contact to metallic CNTs

A large part of the literature on metal-CNT contacts is motivated by the potential of CNT FETs to replace Si based transistor technology. As a consequence the contact formation to metallic CNTs received only little interest.

In general metals that form good contacts to semiconducting CNTs, e.g. Pd and Rh, also form good contacts to metallic CNTs [37, 50]. Interestingly metallic devices often exhibit a good gate tunability of the contact resistance (see e.g. reference [50]). For semiconducting CNTs such a gate dependence of the contact resistance is naturally explained by variations of the Schottky barrier width. For metallic CNTs such a natural explanation is missing. An even more surprising fact was discovered by Kim *et al.* [37]: the contact resistances of devices with rhodium contacts show a similar diameter dependence for semiconducting and for metallic CNTs. Again Schottky barriers provide a natural explanation,  $\phi_{\text{SB}}$  depends on  $E_g$  which scales with  $1/d$ , that only applies for semiconducting CNTs.

One may interpret these surprising similarities in one of the following ways. Either the small band gaps in nominally metallic tubes give rise to Schottky-like physics, or the contact resistance is mostly governed by the microscopic details of the chemical bonding which does not depend on the metallic or semiconducting flavour of the tube. Finally, in some cases semiconducting CNTs with a large chemical doping might be misinterpreted as metallic CNTs.<sup>1</sup>

## 2.3. Carbon nanotube quantum dots

### 2.3.1. Discrete energy spectrum

The electron wave function in a CNT is already confined in two dimensions and the electrons can only move along the tube. The momentum component around the CNT is quantized and can only change in steps  $\Delta k_{\perp} \pi d_{\text{CNT}} = 2\pi$ . Contacts that are patterned onto the CNT introduce additional potential barriers. At low temperature the thermal energy does not suffice to overcome these barriers and electrons need to tunnel through them to enter or leave the CNT. When the tunnel resistance of these barriers becomes comparable to the quantum resistance,  $R_t \gtrsim h/e^2$ , the enclosed CNT segment becomes strongly isolated and forms a QD. The CNT segment can be approximated as a 1-dimensional particle-in-a-box problem, where the

<sup>1</sup>In Fig. 5.5(a) we show a device where the CNT band gap is centred around a backgate voltage of  $V_{\text{BG}} = -18\text{V}$ . When only the transport characteristics are studied such devices can easily be misinterpreted as metallic CNTs due to the limitation of the accessible backgate range.

longitudinal wave vector has to fulfil the boundary conditions of standing wave solutions

$$k_{\parallel} = \frac{n\pi}{L} \quad n = \{1, 2, 3, \dots\}, \quad (2.11)$$

with  $L$  being the length of the respective CNT segment [Fig. 2.7(a)]. The electron momenta are now quantized in all 3 dimensions, giving rise to a discrete energy spectrum. Each level can be filled with up to 4 electrons due to spin and valley degeneracy. The spacing between the levels of a metallic CNT is given by Eq.(2.3) and reads

$$\delta E = \hbar v_F \frac{\pi}{L}, \quad (2.12)$$

which also holds for semiconducting CNTs far away from the band gap. Typical devices, like the one shown in Fig. 2.7(b), are a few hundred nanometers long and obey a level spacing on the meV scale. Hence, the quantum nature of such devices starts to play a role already at temperatures below  $\sim 10$  K.

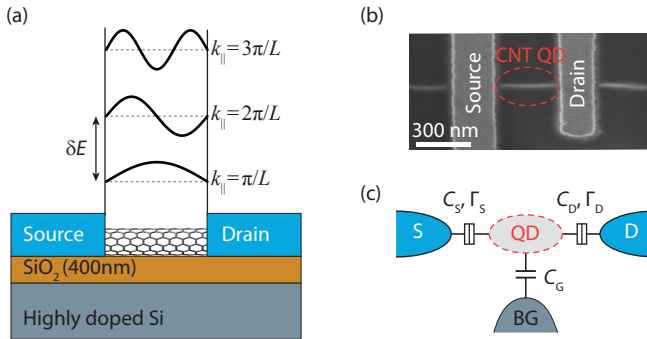


**Figure 2.7.:** Different illustrations of a CNT QD. (a) Source and drain contacts define potential barriers which allow only certain standing wave solutions separated by the quantum mechanical level spacing  $\delta E$ . (b) Scanning electron micrograph of a contacted CNT on  $\text{SiO}_2$  substrate. (c) Capacitance model of a QD. The highly doped substrate serves as backgate (BG) with capacitance  $C_G$ . Source (S) and drain (D) obey tunnel couplings  $\Gamma_S$  and  $\Gamma_D$  in addition to their capacitive couplings  $C_S$  and  $C_D$

### 2.3.2. Coulomb blockade and single electron tunnelling

So far our discussion has neglected the Coulomb interactions between electrons. The effects of Coulomb interactions can be easily included in the framework of the *Constant interaction model* (CIM), which ascribes a single constant capacitance  $C$  to the dot. The CIM further assumes that

the quantum mechanical excitation spectrum remains unaffected by the electron-electron interactions. Despite its conceptual simplicity the CIM proved to be a very successful approximation. Here we follow the discussion of the CIM given in reference [51] with some modifications specific to CNT QDs. In a typical set-up, shown in Fig. 2.7(c), the dot capacitance is the sum the capacitances between the QD and source, drain and gate,  $C = C_S + C_D + C_G$ . One can of course extend the model by adding more capacitances, e.g. from additional gates or from surrounding dielectrics. The total energy of a QD with  $N$  electrons can then be written as

$$E_{\text{tot}}(N) = \frac{(-|e|(N - N_0) + C_S V_S + C_D V_D + C_G V_G)^2}{2C} + \sum_{n=1}^N E_n, \quad (2.13)$$

where  $V_S$ ,  $V_D$  and  $V_G$  are the source, drain and gate voltages and  $N_0$  is the number of dot electrons when all voltages are zero. The first term is simply the electrostatic energy of a capacitor.  $C_G V_G$  can be interpreted as a gate induced charge that allows to shift the dot potential. While the number of electrons on the dot has to change in discrete steps, the gate induced charge can be changed continuously. The terms  $C_S V_S$  and  $C_D V_D$  consider that source and drain contacts also gate the QD. The last term in Eq.(2.13) is the sum over the occupied quantum mechanical energy levels.

The electrochemical potential of the dot, which is the energy required to add one electron to the dot, is defined as

$$\begin{aligned} \mu(N) &= E_{\text{tot}}(N) - E_{\text{tot}}(N - 1) \\ &\propto N \frac{e^2}{C} - \frac{|e|}{C} \sum_i C_i V_i + E_N. \end{aligned} \quad (2.14)$$

This equation describes a "ladder" of electrochemical potential levels illustrated in Fig. 2.8(a,b). The electrochemical potential levels are also referred to as QD resonances. They should not be confused with the energy levels of the QD (each electrochemical potential level describes the difference between two energy levels). In Fig. 2.8(a) the  $\mu(N + 1)$  level is positioned above the lead potentials,  $\mu_S = \mu_D$ . Hence the lead electrons have not enough energy to enter the energy level  $E(N + 1)$ . At the same time the picture assumes that  $\mu(N) < \mu_S = \mu_D$ . This means there are no empty states in the Fermi leads to let the QD relax to  $E(N - 1)$ . The QD is in *Coulomb blockade* with a fixed number of electrons.

To add or remove electrons from the QD one can tune the gate voltage. The complete "ladder" of electrochemical potential levels shifts linearly with

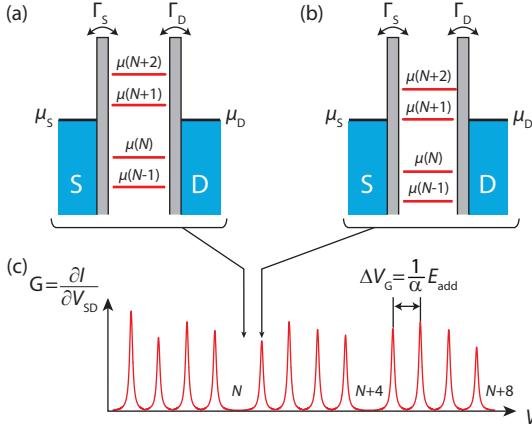


**Figure 2.8.:** (a) Energy diagram of a QD in Coulomb blockade. (b) Energy diagram of QD at resonance. (c) Schematic gate dependence of the differential conductance across a CNT QD with fourfold degenerate energy spectrum.

the gate voltage according to  $\alpha\Delta V_G$ , where  $\alpha = -|e|\frac{C_G}{C}$  is the respective gate efficiency factor also named lever-arm. By increasing  $V_G$  the  $\mu(N+1)$  level can be pushed below the lead potentials and one electron is added to the QD. Figure 2.8(b) shows the situation where the  $\mu(N+1)$ -level is just passing the lead potentials and all three levels are aligned,  $\mu(N+1) = \mu_S = \mu_D$ . When a small thermal broadening of the Fermi leads is assumed there will evidently be electrons with just enough energy to enter  $E(N+1)$ , as well as empty states to let the QD relax back to  $E(N)$ . The QD fluctuates between  $E(N+1)$  and  $E(N)$ . Already a very small voltage across the device,  $V_{SD} = V_S - V_D$ , directs this fluctuations into a current which is carried by electrons that are transferred one-by-one through the QD. When the differential conductance,  $G = \partial I / \partial V_{SD}$ , is measured as a function of  $V_G$  one observes a peak for the gate voltages where the QD is resonant [Fig. 2.8(c)]. The spacing between two such Coulomb peaks is given by the addition energy

$$E_{\text{add}} = \mu(N+1) - \mu(N) = \frac{e^2}{C} + \delta E, \quad (2.15)$$

consisting of an electrostatic part, called charging energy  $U = e^2/C$ , and the quantum mechanical level spacing  $\delta E$  defined in Eq.(2.12). The series of Coulomb peaks directly reflects the fourfold degenerate energy spectrum of

CNTs. The first electron that enters a new CNT shell requires an addition energy  $U + \delta E$ , while the next three electrons must only pay the charging energy  $U$ .

Above we assumed that thermal broadening of Fermi leads plays a dominant role in providing transport electrons. However, the Coulomb peaks have also an intrinsic broadening due to their finite lifetime, i.e. on a short time scale Heisenbergs uncertainty principle allows that electrons with a slightly off-resonant energy enter and leave the QD. The intrinsic lineshape of a QD resonance was calculated by Beenakker [52]:

$$G(\Delta\epsilon) = G_{\max} \frac{\Gamma}{\Delta\epsilon^2 + \Gamma^2/4}, \quad (2.16)$$

where  $\Delta\epsilon \propto \alpha\Delta V_G$  is the detuning from the position of the QD resonance,  $\Gamma = \Gamma_S + \Gamma_D$  is a constant that accounts for the coupling to the source,  $\Gamma_S$ , and the coupling to the drain,  $\Gamma_D$ , and  $G_{\max} = 4 \frac{\Gamma_S + \Gamma_D}{\Gamma_S \Gamma_D}$  gives the maximum of conductance of the Coulomb peak in a fourfold degenerate CNT. The intrinsic lineshape of the QD resonances can only be observed in the regime  $k_B T \ll \Gamma$ , where the Fermi distribution in the leads is sufficiently narrow. If this is fulfilled the full width at half maximum (FWHM) of the Coulomb peaks directly reflects the intrinsic lifetime broadening, which is equivalent to the coupling constant  $\Gamma$ , while the height of the Coulomb peaks can be used to extract the asymmetry between  $\Gamma_S$  and  $\Gamma_D$ .

### 2.3.3. Coulomb diamonds

Coulomb blockade can not only be lifted by gate tuning, but also by the application of an appropriate bias voltage, as illustrated in Fig. 2.9(a-c). Each QD resonance that lies within the bias window constitutes a conductance channel. By measuring the differential conductance as a function of  $V_{SD}$  and  $V_G$  one obtains a so-called *charge stability diagram*. When a QD resonance enters or leaves the bias window the conductance changes abruptly and a peak in differential conductance is measured. The differential conductance is usually encoded as color and the charge stability diagrams show a pattern of diamonds. In Fig. 2.9(d) these diamonds are drawn as red lines imposed on a color scale plot from a measurement of a CNT QD at 4.2 K. Inside the Coulomb diamonds the electron number is fixed and sequential tunnelling is blocked. Outside the diamonds at least one QD resonance lies in the bias window and the blockade is lifted. Along the diamond edges a QD resonance remains aligned with either  $\mu_D$  [lines with negative slope  $s_- = \frac{\Delta V_{SD}}{\Delta V_G}$  in Fig. 2.9(d)] or  $\mu_S$  [lines with positive slope  $s_+ = \frac{\Delta V_{SD}}{\Delta V_G}$  in Fig. 2.9(d)]. The two slopes can easily be calculated. Usually the drain contact is kept at kept at ground,  $\mu_D = 0$ . In this case the gate voltage

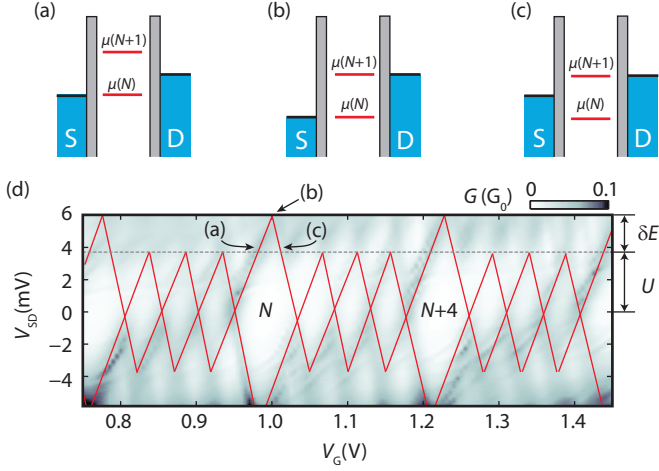


**Figure 2.9.:** (a-c) Energy diagrams of a QD at finite bias. (d) Charge stability diagram,  $G(V_G, V_{SD})$ , of a fourfold degenerate CNT QD measured at 4.2 K. The red lines trace the edges of Coulomb diamonds.

$\Delta V_G$  has to compensate the drag of QD resonance via the source capacitance,  $0 = \frac{C_G}{C} \Delta V_G + \frac{C_S}{C} \Delta V_{SD}$ , which gives the slope  $s_- = -\frac{C_G}{C_S}$ . For the positive slope the QD resonance remains not fixed at  $\mu_D$  but follows  $\mu_S$ , i.e.  $\Delta V_{SD} = \frac{C_G}{C} \Delta V_G + \frac{C_S}{C} \Delta V_{SD}$ , which gives a slope  $s_+ = \frac{C_G}{C - C_S}$ . At the top of the diamond both lines cross and the source drain voltage  $V_{SD}$  corresponds to the spacing between two QD resonances [Fig. 2.9(b)]. This provides a direct measurement of the addition energy, which can be used to extract the gate efficiency factor  $\alpha$ . When a clear shell filling pattern is observable one can separate the charging energy  $U$ , which is 3.8 meV in Fig. 2.9(d), from the level spacing, which is 3.8 meV in the same figure. Furthermore the gate efficiency factor  $\alpha$  and the two slopes  $s_+$  and  $s_-$  allow to calculate the capacitances  $C_S$ ,  $C_G$  and  $C$ .

### 2.3.4. Co-tunnelling and excited states

All QD states we considered so far have been ground states, i.e. the dot electrons could not relax into a lower lying QD state. When the necessary energy  $\delta E$  is provided the  $N^{\text{th}}$  electron may be excited into the  $E_{N+1}$ -level and after some time decay back into  $E_N$ . In the following we denote ground state and the first excited state of the QD with  $N$  electrons as  $\text{GS}(N)$  and

$ES(N)$ . In Fig. 2.10(b) we plot the ground state energies and in addition the energy of the  $ES(N)$  state. Transition between the states are drawn as color-coded arrows. The length of the arrow corresponds to the height chemical potential level in Fig. 2.10(c-f). When an excited state falls into the bias window [Fig. 2.10(c,f)] a new conductance channel becomes available. The onset of the additional conductance channel gives rise to the dotted lines in the stability diagram in Fig. 2.10(a). These lines run parallel to the diamond edges and terminate when the bias drops below  $|e|V_{SD} < \delta E$ . To understand the latter we consider the situation in Fig. 2.10(e). The  $ES(N) \leftrightarrow GS(N+1)$  lies within the bias window and is energetically allowed. But once the QD relaxes from  $ES(N)$  to  $GS(N)$  Coulomb blockade is restored and the current is blocked.

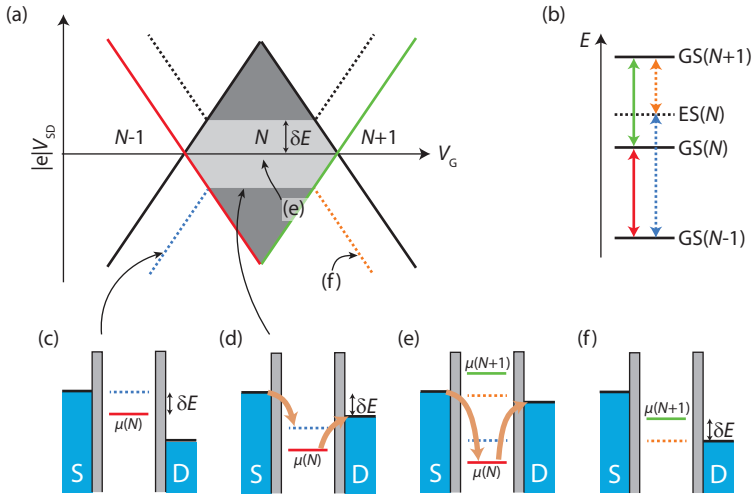


**Figure 2.10.:** (a) Schematic of a stability diagram that also contains sequential transport through excited states (dotted lines), elastic co-tunnelling current (light grey region) and inelastic co-tunnelling current (dark gray region). (b) Schematic of the energy spectrum. The arrows are colour coded and correspond to the transitions in (a) and to the chemical potential levels in (c-f), where we illustrate the following processes: (c) Sequential tunnelling through  $GS(N)$  and  $ES(N)$ . (d) Inelastic co-tunnelling. (e) Elastic co-tunnelling. (f) Sequential tunnelling through  $GS(N+1)$  and  $ES(N)$ .

So far we argued that current flow can only occur via sequential tunnelling where the QD fluctuates between states with  $N$  and  $N+1$  electrons. However, when higher order tunnelling processes are considered this statement is not true anymore. Again the Heisenberg uncertainty principle provides

us with a tolerance margin. In Fig. 2.10(e) we illustrate a second-order process known as elastic co-tunnelling. One electron enters the QD from the source and within the uncertainty time  $\tau \approx \hbar/U$  a second electron leaves the QD to the drain. The corresponding current turns out to be proportional to the bias voltage,  $I_{EC} \propto |e|V_{SD} \frac{\Gamma_S \Gamma_D}{U^2}$  [53] and thus the differential conductance due to elastic co-tunnelling is constant. When the source-drain voltage overcomes the level spacing  $\delta E$  also inelastic co-tunnelling events start to contribute. These inelastic co-tunnelling events leave the QD in an ES. To first approximation the onset of inelastic co-tunnelling yields a step in  $\partial I/\partial V_{SD}$  [54]. This step corresponds to the boarder between the light grey and dark grey regions in Fig. 2.10(a).



## Quantum dots coupled to superconductors

When a quantum dot (QD) is coupled to a superconducting electrode (S) two very distinct phenomena clash: superconductivity arises from the collective behaviour of a large number of electrons, while QDs usually act as turnstiles that let electrons pass only one-by-one. In a superconductor the electrons feel a net attractive interaction that binds them into pairs, while a QD confines electrons in such a small region that the electrons strongly repel each other. The basic physics of QD-S hybrid systems is therefore governed by a competition between attraction and repulsion. This interplay can even be spiced with additional effects, such as Kondo correlations or spin-orbit interactions. Thus, QDs coupled to S-contacts became a fundamental model system that allows to study a large variety of phenomena. Prominent examples are the Josephson effect [55] and the formation of so-called bound states (e.g. Andreev bound states [56], Yu-Shiba-Rusinov bound states [57] and Majorana bound states [58, 59]). On the other hand, the QD-S unit can be viewed as the basic building block of novel quantum electronic devices: supercurrent transistors [60], nano-SQUIDS [56, 61, 62] and Cooper pair splitters [63–66] have already been realized and researchers constantly propose new device ideas (see e.g. Refs. [67–69]).

The diversity of phenomena and device possibilities are overwhelming. Here we focus on two aspects out of this vast spectrum. In Sec. 3.2 we discuss Cooper pair splitters. Those devices have the prospect to act as continuous on-chip sources to generate spatially separated spin-entangled electron pairs. Section 3.3 focuses on Andreev bound states. A new type of energy level that can appear at energies inside the superconducting gap. Since the

recent observation in CNT QDs [56] Andreev bound states received a lot of interest [70–73]. They play a key role for the superconducting proximity effect in mesoscopic systems [74]. But first we give a brief introduction to superconductivity.

## 3.1. Superconductivity

In this section we briefly discuss the electronic properties of superconductors. For a more detailed introduction the reader is referred to the literature, e.g. Refs. [75, 76] whose presentations we will partially follow.

### 3.1.1. Basic phenomena

The hallmark feature of superconductivity was first observed in 1911 by Kamerlingh Onnes [77]: the electrical resistance of certain materials – e.g. mercury and lead, but also aluminium or niobium – vanishes when the temperature drops below a critical value  $T_c$ . Experiments with persistent currents in superconducting rings provide the most sensitive probe of this ideal conductivity. Below  $T_c$  the resistance can drop by at least 14 orders of magnitude, suggesting that the resistance literally vanishes, i.e.  $R = 0$  [76]. A second key feature, namely perfect diamagnetism in the superconducting state, was discovered in 1933 by Meissner and Ochsenfeld [78]. Perfect diamagnetism implies that magnetic fields will be expelled from the metal when the superconducting state is entered. A consequence of the perfect diamagnetism is the existence of a critical magnetic field,  $B_c$ , for which superconductivity breaks down due to the energy cost to keep the magnetic field out of the bulk. More precisely, the external field leads to an increase of the Gibbs energy of the superconductor according to  $dG_S = -VMdB$ , where  $V$  is the Volume,  $M = -B/\mu_0$  is the magnetization of a perfect diamagnet and  $dB$  is magnetic field change. In the normal state the magnetic susceptibility is much smaller and the Gibbs energy has only a weak  $B$  field dependence. Therefore there must be a critical field for which the Gibbs energy of the superconducting state rises above that of the normal state,  $G_S(B_c, T) = G_N(B_c, T) \approx G_N(0, T)$ . At this point the superconductor is quenched into the normal state – a behaviour we will frequently use to perform control experiments in the normal conducting state.

### 3.1.2. Cooper pairs

The microscopic explanation of superconductivity was given by Bardeen, Cooper and Schrieffer and is now known as the BCS theory [79]. One pillar of this theory is a fundamental theorem that was worked out by Cooper [80]:

in the presence of a Fermi sea any net attraction between two electrons, no matter how small it is, can bind the electrons together into a so-called Cooper pair (given that the temperature is low enough). For the ordinary two-body problem in 3D it is well known that the attractive forces must exceed a finite threshold value to create a bound state. The background of the Fermi sea makes a crucial difference because Cooper pairs are composite particles of two fermions and thus obey Bose statistics. When two electrons in the vicinity of Fermi surface pair up, the Pauli exclusion principle no longer applies. Metaphorically speaking the Cooper pair cross the Fermi surface and dive into the Fermi sea. Thus the energy gain upon creation of a bound state is much larger than for two free particles in vacuum.

It was further shown by Cooper that the binding energy of the electron pair is a very sensitive function of the total momentum,  $\mathbf{K} = \mathbf{k}_1 + \mathbf{k}_2$ , where  $\mathbf{k}_1$  and  $\mathbf{k}_2$  are the wavevectors of the two electrons. The binding energy is maximal for  $\mathbf{K} = 0$  and decays very rapidly otherwise, i.e. the two electrons of a Cooper pair have opposite momenta,  $\mathbf{k}_1 = -\mathbf{k}_2$ . To understand this important result we have to consider the physical origin of the attractive interaction, which is mediated by the ion lattice. In a classical picture one might envision an electron that moves across the solid and thereby attracts the positively charged ion cores. The electron deforms the ion lattice, dragging a cloud of positive polarization behind which in turn attracts other electrons. In a quantum mechanical language one ascribes the attractive interaction to the exchange of virtual phonons. After two electrons exchange a virtual phonon with wavevector  $\mathbf{q}$  their initial wavevectors are changed to  $\mathbf{k}'_1 = \mathbf{k}_1 + \mathbf{q}$  and  $\mathbf{k}'_2 = \mathbf{k}_2 - \mathbf{q}$ , conserving the total momentum  $\mathbf{K} = \mathbf{k}_1 + \mathbf{k}_2 = \mathbf{k}'_1 + \mathbf{k}'_2$ . The energy transfer of this mechanism is limited by the available phonon energies, which are cut-off at the Debye frequency  $\omega_D$ . We assume very low temperatures so that all electron states with energies below the Fermi energy are occupied. Hence the phonon mediated interactions are restricted to a very narrow energy range between  $E_F$  and  $E_F + \hbar\omega_D$ . In the reciprocal space this corresponds to a narrow shell with a thickness  $\delta k = (m\omega_D/\hbar k_F)$  around the Fermi sphere. Figure 3.1 illustrates why the probability for phonon exchange is only significant for electrons that fulfil  $\mathbf{K} = 0$ . For  $\mathbf{K} = 0$  the complete  $\delta k$  shell is accessible, while for  $\mathbf{K} \neq 0$  momentum conservation restricts the allowed scattering states to the small area where both shells intersect.

Knowing that the two electrons of a Cooper pair have opposite momenta ( $\mathbf{k}, -\mathbf{k}$ ) suggests that Cooper pairs can be described by an orbital wavefunction of the form

$$\psi(\mathbf{r}_1, \mathbf{r}_2) = \sum_{k=k_F}^{k_F+\delta k} g_{\mathbf{k}} e^{i\mathbf{k}\cdot\mathbf{r}_1} e^{-i\mathbf{k}\cdot\mathbf{r}_2}, \quad (3.1)$$

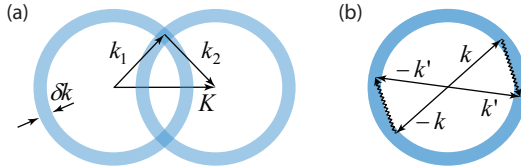


**Figure 3.1.:** Illustration of the momentum conservation for the exchange of a virtual phonon. The blue circles represent the allowed magnitude of the initial and final wavevector ranging from  $k_F$  to  $k_F + \delta k$ . (a) For  $\mathbf{K} \neq 0$  the only the small area where the two circles intersect fulfil momentum conservation. (b) For  $\mathbf{K} = 0$  the two circles lie on top of each other and the number of scattering events that fulfil momentum conservation is maximal. The argument is even more convincing when expanded to the 3D case, where the circles are replaced by spherical shells.

which can be expanded either in terms of  $\sin(\mathbf{k} \cdot (\mathbf{r}_1 - \mathbf{r}_2))$  or  $\cos(\mathbf{k} \cdot (\mathbf{r}_1 - \mathbf{r}_2))$  functions. The cosine ensures a larger probability amplitude for the electrons to be near each other, which seems favourable in the presence of attractive interactions. Indeed conventional superconductors obey a symmetric orbital wavefunction. To restore the antisymmetry of the total wavefunction we have to multiply the orbital part of the wavefunction with a spin singlet,

$$|S\rangle = \frac{1}{\sqrt{2}} (|\uparrow\downarrow\rangle - |\downarrow\uparrow\rangle), \quad (3.2)$$

where we have switched to the Dirac notation. The symbol  $(k \uparrow, -k \downarrow)$  is often used to describe a Cooper pair. However, it is important to remember that the spins of the two electrons are in a superposition state: if one could measure the spin of the electrons along a given axis the spin of one electron will point up and the spin of the other electron will point down, but the spin directions of the individual electrons remain undetermined until the first spin projection measurement performed, fixing the spin direction of both electrons. In other words: the two individual spins of a Cooper pair are maximally entangled, while the total spin is zero.

### 3.1.3. The energy gap

Cooper considered for his argument only one bound pair on the background of the Fermi sea. But at the same time his argument implies that the Fermi sea becomes unstable in the presence of attractive interactions: electrons keep condensing into pairs until an equilibrium state is reached which differs so strongly from the Fermi sea that Cooper's argument becomes inapplicable. A description of this state could in principle be given by extending the two-electron wavefunction from Eq. (3.1) to  $N$  electrons. However, for

all practical purposes such a description is useless, because one would have to determine hopelessly many probability amplitudes ( $\sim 10^{(10^{20})}$  for realistic situations [75]). The breakthrough of BCS was that they managed to find better representation of this wavefunction and thereby made the ground state accessible to a mathematical treatment. Still, the math of the BCS theory is rather complicated and we omit the derivation of the results presented in the following.

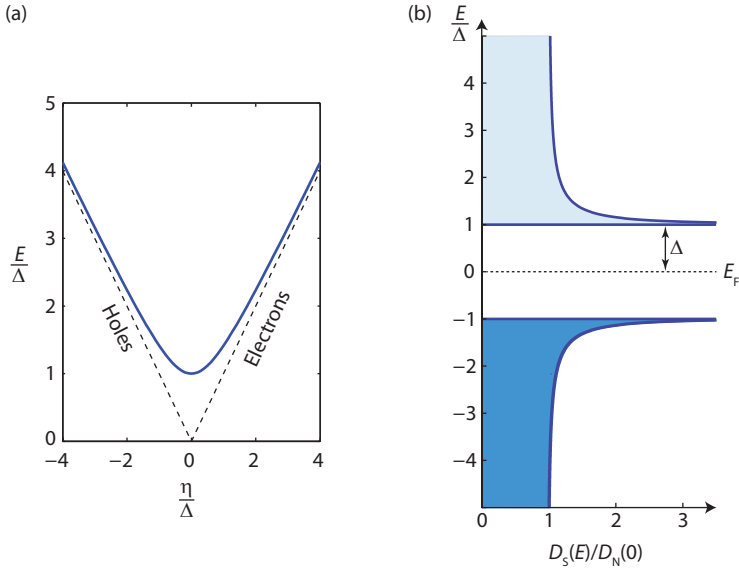


**Figure 3.2.:** (a) Quasiparticle excitation energy (solid line) in comparison with the electron energy in the normal state (dashed line) as a function of  $\eta$ , the kinetic energy of free electrons. The quasiparticle spectrum has an electron-like and a hole-like part. (b) Normalized density of states of the quasiparticles as a function of energy plotted in a band diagram fashion.

The most important finding of the BCS theory is that excitations from the ground state require a minimum energy of  $2\Delta$ . The quantity  $\Delta$  is referred to as the superconductor's energy gap. The factor of 2 stems from the fact, that elementary excitations correspond to the breaking of one pair into two unpaired charge carriers. We know from above that the background state must differ strongly from the Fermi sea. The unpaired charges that live in this new background state are called quasiparticles to distinguish them

from free electrons. The dispersion relations for these quasiparticles can be written as

$$E(\mathbf{k}) = \sqrt{\eta(\mathbf{k})^2 + \Delta^2}, \quad (3.3)$$

where  $\eta(\mathbf{k}) = \hbar^2 \mathbf{k}^2 / 2m - E_F$  is the kinetic energy of a free electron with respect to the Fermi energy. This dispersion relation has an electron-like branch ( $\eta > 0$ ) and a hole-like branch ( $\eta < 0$ ). In Fig. 3.2(a) we compare the energy of the quasiparticles to that of free electrons. For quasiparticles with large kinetic energies  $\eta \gg \Delta$  ( $\eta \ll \Delta$ ) the behaviour of free electrons (free holes) is restored. For small kinetic energies the behaviour of quasiparticles strongly deviates from that of free electrons, because the quasiparticles must obey a minimum energy of  $\Delta$ . The energy gap separates the Cooper pair condensate from the quasiparticle excitations, as becomes even clearer when we equate the quasiparticle DOS according to  $D_S(E)dE = D_N(\eta)d\eta$ :

$$D_S(E) = D_N(\eta) \frac{d\eta}{dE} = \begin{cases} D_N(\eta) \frac{E}{\sqrt{E^2 - \Delta^2}} & (E > \Delta) \\ 0 & (E < \Delta) \end{cases} \quad (3.4)$$

Usually one is interested in an environment of a few meV around the Fermi energy, where one can crudely approximate  $D_N(\eta) \approx D_N(0)$ . In Fig. 3.2(b) we plot the quasiparticle DOS normalized to  $D_N(0)$ . The existence of electron-like and hole-like quasiparticles suggests to plot the DOS in analogy to the band diagrams used in the theory of semiconductors. For large energies,  $E \gg \Delta$ , the behaviour in the normal state is resembled again. As the energy approaches  $\Delta$  the  $D_S(E)$  starts to grow and even diverges for  $E \rightarrow \Delta$ . For  $E < \Delta$  the DOS is zero, meaning that there are no quasiparticle states but only Cooper pairs.

The quasiparticle DOS can be probed by tunnelling spectroscopy, which is a conceptually simple and elegant method. Let us consider a NIS sandwich, i.e. a normal conductor and a superconductor that are separated by a thin insulating tunnel barrier. The current from N to S can be written as

$$I_{N \rightarrow S} = A \int |t|^2 D_N(E + eV) f(E + eV) \cdot D_S(E) [1 - f(E)] dE, \quad (3.5)$$

where  $D_N(E + eV)f(E + eV)$  gives the number of electrons in N and  $D_S(E)[1 - f(E)]$  gives the number of empty states in S. The tunnel barrier is characterized by the matrix element  $|t|^2$ ,  $V$  is the voltage drop across the barrier and  $A$  is a proportionality constant. After equating the current in the reversed direction,  $I_{S \rightarrow N}$ , and subtracting the two contributions one

obtains:

$$\begin{aligned} I &= I_{N \rightarrow S} - I_{S \rightarrow N} \\ &= A|t|^2 \int D_N(E + eV) D_S(E) [f(E + eV) - f(E)] dE. \end{aligned} \quad (3.6)$$

From this expression we calculate the differential conductance  $\partial I / \partial V$ . In the limit  $T \rightarrow 0$  the derivative of the Fermi function is given by the Dirac delta function  $\delta(E + eV)$ . The evaluation of the integral becomes trivial,

$$G = \frac{\partial I}{\partial V} = A|t|^2 D_N(0) D_S(E = eV), \quad (3.7)$$

and we see that the differential conductance across the NIS tunnel junction is directly proportional to the quasiparticle DOS at  $E = eV$ . A more interesting system is obtained when the insulating layer is replaced by a QD. Such N-QD-S junctions are the basic building blocks of the devices which are investigated in the main chapters of this thesis. Being characterized by two tunnel barriers and the QD spectrum, such N-QD-S junctions can already become rather hard to handle theoretically. Nonetheless, there are regions of the parameter space for which the devices can be understood quite intuitively. A particular simple example is a QD deep in Coulomb blockade. The differential conductance,  $G(V_{SD})$ , in the normal state is given by the elastic co-tunnelling background, which is approximately independent of  $V_{SD}$ . In the superconducting state the co-tunnelling conductance is multiplied with  $D_S(E = eV_{SD})$  and the QD acts as tunnel probe for the quasiparticle DOS (see e.g. Fig. 6.9).

Finite temperatures lead to a smearing of  $D_S(E)$  and to a reduction of  $\Delta$ . Thermally created quasiparticles occupy otherwise empty states. These states are no longer accessible for Cooper pairs. Less phonons can be exchanged and the gap decreases. The temperature evolution of the gap can be approximated as

$$\Delta(T) \approx \Delta(0) \left(1 - \frac{T}{T_c}\right)^{1/2}, \quad (3.8)$$

and the gap size at zero temperature can be related to the critical temperature via

$$\Delta(0) \approx 1.74 k_B T_c. \quad (3.9)$$

The latter equation involves some assumptions about the coupling constant that characterizes the phonon exchange and for some (strongly coupled) materials there are deviations from the given value.

Another important quantity which is related to the energy gap is the BCS coherence length

$$\xi_0 = \frac{\hbar v_F}{\pi \Delta}. \quad (3.10)$$

Except for the additional factor  $\pi$  the same result is obtained by considering the position uncertainty  $\delta x \approx 1/\delta k$  that results from the energy uncertainty  $\Delta$ , according to  $\delta k \approx \left. \frac{dk}{d\eta} \right|_{k_F} \delta E$ . Thus the coherence length can be interpreted as the spatial extent of a Cooper pair. Typical values for  $\xi_0$  range from a few tens to a few hundred nanometers. This means the Cooper pairs strongly overlap in the condensate. It also explains why the attractive phonon interaction can be larger than the Coulomb repulsion between the electrons: Coulomb interactions are typically screened on a length scale of  $\sim \text{\AA}$ .

We finish this section with a brief comment and the relation between the energy gap and the vanishing of the electrical resistance. In a normal conductor the resistance is caused by scattering from defects and phonons. In a superconductor the current is carried by the common motion Cooper pairs, characterized by an additional wavevector  $\delta \mathbf{K}$ , and a scattering event requires that a Cooper pair is broken (otherwise the momentum of all Cooper pairs would have to change, requiring an energy way larger than  $2\Delta$ ). Thus elastic scattering can be excluded right away, but also inelastic pair breaking events do not necessarily lead to a DC resistance. For  $R = 0$  there are no electric field gradients in the sample. The quasiparticles are not accelerated but remain at their position until they re-condense to Cooper pairs. However, in the presence of AC fields, flux traps, etc. also superconductors exhibit finite resistances.

### 3.1.4. Proximity effect and Andreev reflections

A good estimation of the size of a Cooper pair is given by considering the position uncertainty that corresponds to the energy uncertainty  $\Delta$ . It is intuitively clear that the Cooper pair density can not abruptly drop to zero, but rather decays smoothly over lengthscales on the order of the coherence length. A striking consequence of this behaviour is the superconducting proximity effect: Cooper pairs will leak into non-superconducting materials if these are placed in electrical contact with a superconductor. This leads to the occurrence of superconducting-like properties in the proximitized objects. This macroscopic view of the proximity effect can be described within the framework of the of the Ginzburg-Landau theory, where a macroscopic wavefunktion,  $\psi(\mathbf{r}) = \sqrt{\mathcal{N}(\mathbf{r})} e^{i\Phi(\mathbf{r})}$ , is assigned to the common ground state of the Cooper pairs and  $\mathcal{N}(\mathbf{r})$  is the Cooper pair density at the position  $\mathbf{r}$ .

However, the proximity effect can also be described in a microscopic language.

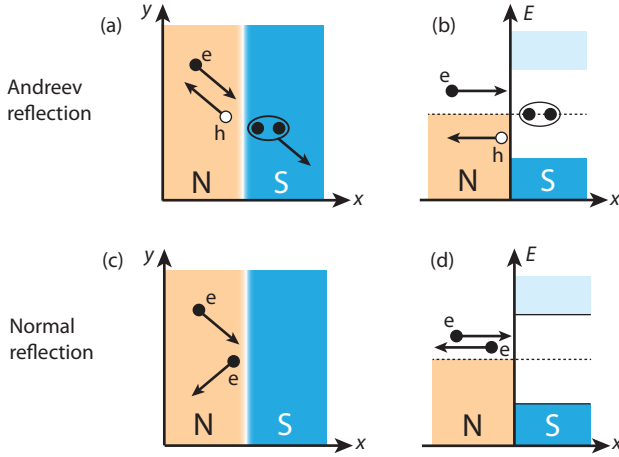


**Figure 3.3.:** Illustration of normal reflection and Andreev reflection of an electron at an NS interface. (a) and (c) give a real space representation while in (b) and (d) we draw energy-space diagrams.

On a microscopic level the proximity effect is carried by a process known as Andreev reflection. Andreev reflections occur at interfaces between normal metals (N) and superconductors (S). Let us consider an electron with sub-gap energy,  $|E| < \Delta$ , that impinges on a fully transparent NS interface. This situation is depicted in Fig. 3.3(a,b). The electron can not simply enter S since its energy is not sufficient to create a quasiparticle. At the same time the superconductor can not simply reflect the electron: a normal reflection of an electron, illustrated in Fig. 3.3(c), inverts the momentum component perpendicular to the interface,  $p_{\perp} \rightarrow -p_{\perp}$ . This requires a momentum transfer of  $2p_{\perp}$ . Without a sufficient potential barrier, e.g. due to a thin insulating layer between S and N, there is nothing which could take up the momentum of the electron, which is on the order of  $k_F$ . The superconductor constitutes a potential barrier with a maximal height  $\Delta$  and the maximal momentum that the superconductor can exert on the electron may be calculated as  $\delta k = \left(\frac{dk}{dE}\right)_{k_F} \delta E = \frac{1}{\hbar v_F} \Delta$  which is orders of magnitude smaller than  $k_F$ . An electron impinging on the superconductor is the unstoppable force hitting the unmovable object [81]. The way out of this dilemma is a simple second order process. The electron with  $E$  and  $|\mathbf{k}, \uparrow\rangle$  pairs up with

a partner electron at  $-E$  and  $|\mathbf{-k}, \downarrow\rangle$  to enter S by creation of a Cooper pair.<sup>1</sup> The second electron leaves a hole in N. This hole is associated with a positive energy  $E$  and  $|\mathbf{k}, \uparrow\rangle$ . Since the hole has a negative mass its velocity vector points in the opposite direction of its momentum vector: the hole travels backwards on the path of the incident electron, a phenomenon known as retro-reflection. The time reversed process of Fig. 3.3(a,b) is the retro-reflection of a hole as an electron. This latter process corresponds to the leaking of a Cooper pair into N.

Considering that there is no attractive interaction between electrons in a normal conductor it may seem adventurous to apply the term "Cooper pair" to any electron pair that is located in N. The crucial point is the coherence of the Andreev process which allows the two electrons to maintain their phase relation, at least for a certain time. As long as the two electrons maintain the "right" phase and energy relations in N they might just re-enter the pair condensate in S. On a microscopic level the proximity effect results from a combination of the mechanism of Andreev reflections and the phase coherence in N [82]. A nice illustration of this collaboration between Andreev reflection and phase coherence is provided by the Josephson effect: a dissipationless current can flow across an SNS junction, justifying the idea of Cooper pairs leaking into N, and the magnitude of this Josephson current critically depends on the phase difference of the macroscopic wavefunctions in the two S layers, indicating the phase coherence of the process.

### 3.1.5. Crossed Andreev reflection and elastic co-tunnelling

Above we discussed Andreev reflection as a phase coherent process that converts an electron pair ( $k \uparrow, -k \downarrow$ ) into a Cooper pair (or vice versa) and governs the sub-gap transport of NS interfaces. Since the Cooper pairs have a spatial extent on the order of the coherence length  $\xi_0$  it is possible that a hole entering S at a position  $x$  is retro-reflected as electron at a different position  $x + L$  with  $L < \xi_0$ . In multi-terminal geometries this can lead to cross conductance channels.g. between two normal leads, N1 and N2, which are connected at a small distance to the same S, as illustrated in Fig. 3.4. In a matrix notation these cross conductances correspond to the off-diagonal terms in

$$\begin{pmatrix} I_1 \\ I_2 \end{pmatrix} = \begin{pmatrix} G_{11} & G_{12} \\ G_{21} & G_{22} \end{pmatrix} \begin{pmatrix} U_1 \\ U_2 \end{pmatrix}, \quad (3.11)$$

---

<sup>1</sup>Note that the condition  $\mathbf{k}_2 = -\mathbf{k}_1$  only holds approximately. Due to the different energies of the two electrons the magnitude of the wave vectors differ by  $\frac{2E}{\hbar v_F}$ , which is usually negligible small.

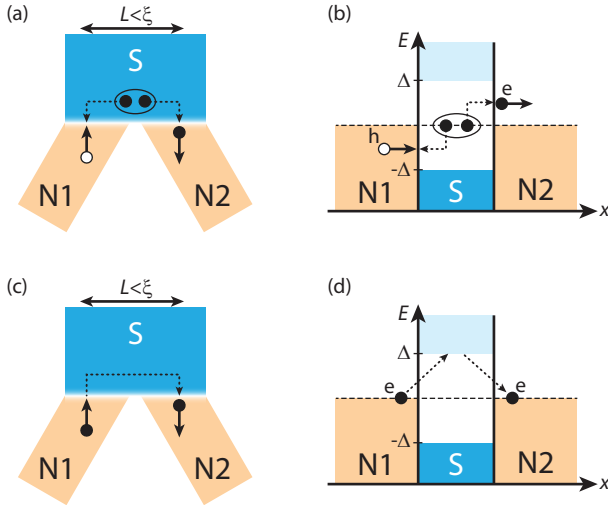


**Figure 3.4.:** Illustration of the non-local generalizations of Andreev reflection and normal reflection for a three-terminal device. (a) Crossed Andreev reflection in real-space and (b) as energy-space diagram. (c) Elastic co-tunnelling in real-space and (b) as energy-space diagram.

where the index labels the respective lead N1 or N2. The non-local generalization of the Andreev mechanism is known as crossed Andreev reflection (CAR). In the case depicted in Fig. 3.4, where the incoming hole from N1 is reflected as electron into N2, CAR corresponds to the splitting of a Cooper pair into two separate leads. This process triggered a lot of attention because it is a potential source for spatially separated spin-entangled electrons (see Sec. 3.2, Chapter 6 and references therein). The reverse process corresponds to the non-local creation of a Cooper pair.

In metallic NSN structures it is hard to observe CAR processes because there is another competing process, which can be viewed as the non-local generalization of a normal reflection: A single charge carrier, be it an electron or a hole, can tunnel between N1 and N2 by propagation through S as a virtual quasiparticle. In analogy to the tunnelling events discussed in Sec. 2.3.4 this process is called elastic co-tunnelling (EC). At a first sight one might guess that the probability amplitude for EC is lower than for CAR because EC involves a virtual intermediate state with an energy deficit  $\Delta$ . However, when we assume that the separation between the tunnelling points obeys  $L < \xi_0 = \hbar v_F / \pi \Delta$  this argument does not apply. If the quasiparticles

propagates from  $x$  to  $x + L$  with the Fermi velocity, then the duration time in S is given by  $\tau = v_F L$ . Thus the restriction of the length-scale can be translated into the inequality  $\tau < \hbar/\pi\Delta$ , which means that the uncertainty principle allows the creation of the virtual quasiparticle. It turns out that CAR and EC have approximately the same probability amplitudes, which decay exponentially on the scale of  $\xi_0$  [83].

## 3.2. Cooper pair splitters

We saw in the last section that crossed Andreev reflections provide a mechanism to create pairs of spatially separated spin-entangled electrons. However, metallic NSN junctions provide only little control over the respective transport processes. In particular it is very hard to enhance CAR processes with respect to local transport and EC. In an influential work Recher *et al.* suggested to insert tunable QDs between S and N to gain additional control knobs [84]. Figure 3.5 shows a sketch of such a device, to which we refer in the following as Cooper pair splitter. The figure also lists the relevant device parameters<sup>2</sup>.

The main idea is that the on-site Coulomb interactions prohibit a double occupancy of the QDs, which forces the Cooper pairs are to split into separate QDs in a crossed Andreev process. In principle it is possible to build an entangler with 100% efficiency: a device that converts an incoming stream of electrons into pairs of spin-entangled electrons that leave the device through two separate output terminals. Below we will discuss this claim, closely following the argumentation of Ref. [84].

### 3.2.1. Basic idea and working conditions

The Cooper pair splitter is based on the combination of two main effects, the Coulomb interactions  $U_1$  and  $U_2$  on QD1 and QD2 (for simplicity we assume  $U_1 = U_2 = U$ ) and the pairing interaction  $\Delta$  in the superconductor. Naturally, the device must be operated at a temperature where these two effects are well resolved,  $k_B T \ll U, \Delta$ . Also the bias voltage, applied between S and each of the drains N1 and N2, must not exceed these energy scales,  $|eV_{SD}| < U, \Delta$ . The basic idea of the device is to suppress the tunnelling of Cooper pairs into the same lead. Such local pair tunnelling (LPT) can happen via the two channels illustrated in Fig. 3.6(a,b). The two electrons of a Cooper pair can tunnel simultaneously on one QD, at the cost

---

<sup>2</sup>The chemical potentials of the leads  $\mu_{N1}, \mu_{N2}$  and  $\mu_S$ , the couplings between QD $_i$  and the leads,  $\Gamma_{N1}$  and  $\Gamma_{S1}$  with  $i = 1, 2$ , the inter-dot coupling  $\Gamma_{12}$ , the charging energies  $U_i$ , the energy gap  $\Delta$  and the spatial separation between the tunnelling points  $\delta r$ .

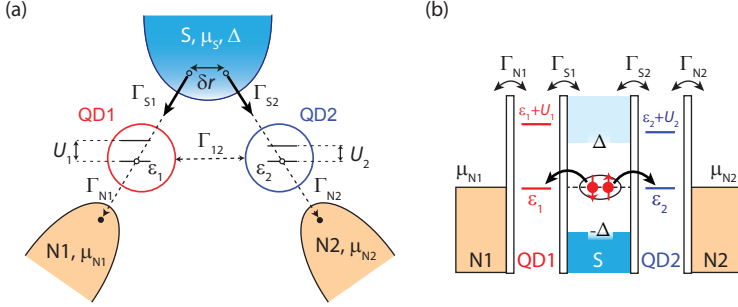


**Figure 3.5.:** Illustration of CPS device (a) in real space and (b) as energy-space diagram. Adapted from [84, 85].

of the charging energy  $U$ , and then leave to the respective lead (process I). Since neither  $T$  nor  $V_{SD}$  provide the charging energy, the doubly occupied QD constitutes a virtual state that is suppressed by  $1/U$ . Alternatively, the two electrons of a Cooper pair can escape to the same lead by a sequential tunnelling process (process II): A Cooper pair is broken up, one electron tunnels to one of the QDs, while the second electron waits in  $S$  as a virtual quasiparticle excitation. After the first electron tunnels from the QD to the lead, the second electron can follow the first one without causing a double occupancy of the QD. This process is suppressed with  $1/\Delta$  due to the virtual excitation of a quasiparticle. By increasing  $U$  and  $\Delta$  the rate of the parasitic local tunnelling processes can be made arbitrarily small. On the contrary, the desired Cooper pair splitting (CPS) suffers from no such suppression factors. CPS requires neither a double occupancy of a QD nor the waiting in a virtual quasiparticle state. Therefore the ratio between the desired CPS current and the parasitic LPT current can become arbitrarily large,  $I_{CPS}/I_{LPT} \rightarrow \infty$  for  $U, \Delta \rightarrow \infty$ .

In addition to  $T$  and  $V_{SD}$  the lifetime broadenings  $\Gamma_1 = \Gamma_{S1} + \Gamma_{N1}$  and  $\Gamma_2 = \Gamma_{S2} + \Gamma_{N2}$  of QD1 and QD2 are the critical quantities against which  $U$  and  $\Delta$  must be small. We simplify the discussion by setting  $\Gamma = \Gamma_1 = \Gamma_2$ . When the level broadening  $\Gamma$  becomes comparable to  $\Delta$  (or  $U$ ), the lifetime of the QD states,  $\tau \sim \hbar/\Gamma$ , corresponds to an energy uncertainty that is compatible with transport process II (or process I): the filter mechanism of the respective QD becomes ineffective.

Recher *et al.* proposed to operate the device in the regime  $\Gamma_N \gg \Gamma_S$ . This asymmetric coupling ensures that the electrons leave the QDs much

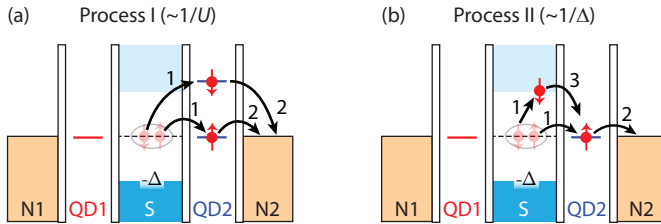


**Figure 3.6.:** Energy diagrams for the two parasitic local pair tunnelling processes. (a) The two electrons of a Cooper pair tunnel simultaneously on QD2 before they leave to N2. (b) The Cooper pair tunnels sequentially through QD2. The Cooper pair breaks up and one electron waits in a virtual quasiparticle state until the other electron tunnels via QD2 to N2.

faster to the N side, than they are replaced by new electrons from S. In this limit the QDs have vanishing occupation probabilities, which greatly simplifies the theoretical treatment of the device. We don't have to worry about electrons that remain on the QDs and thereby block subsequent CPS processes. In general a competition between different transport processes arises when the QDs are occupied with a finite probability. In chapter 6 we introduce a semi-classical master equation "toy model" that considers these competitions. This "toy model", however, neglects the coherence of the tunnelling processes which may lead to even further-reaching consequences: coherent oscillations between states with the Cooper pair in S and states with the Cooper pairs in the QDs may modify the energy spectrum of the QDs. In the limit  $\Gamma_N \ll \Gamma_S$  this can lead to the formation of Andreev bound states via the coherent repetition of the first step of LPT process I (see Sec. 3.3). For models that take such coherent oscillations into account we refer to Refs. [86–88]. A strong coupling to the Fermi leads, where the coherence is typically lost on a very short time-scale  $\tau \sim 1/E_F$ , inhibits such coherent oscillations [86].

Another coupling constant that we must take into account is the inter-dot tunnel coupling  $\Gamma_{12}$ . Such a coupling can arise due to elastic co-tunnelling via a virtual intermediate state in S or due to a direct tunnel coupling between QD1 and QD2. Obviously, an inter-dot tunnelling can lead to processes where both electrons of a Cooper pair end up in the same lead N1 or N2. The condition  $\Gamma_N \gg \Gamma_{12}$  ensures that the electrons usually leave to N before they have the chance to tunnel between QD1 and QD2. Again, one can think of this condition not only in the time domain, but also in the energy domain. The inter-dot tunnel coupling leads to a hybridization of the two QDs. This hybridization is characterized by avoided crossings in the

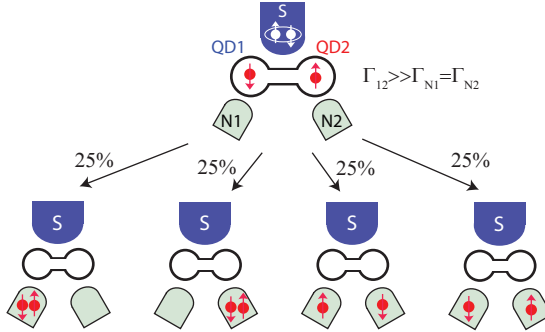


**Figure 3.7.:** Cooper pairs can also be split in electronic forks that act as Cooper pair "beam splitters" [64]. Such a device can be realized with a double QD with strong inter-dot coupling,  $\Gamma_{12} \gg \Gamma_{N1}, \Gamma_{N2}$ . The maximum efficiency is achieved with an unbiased beam splitter,  $\Gamma_{N1} = \Gamma_{N2}$ . In this case each electron of a Cooper pair will enter any of the two output terminals with 50% chance. This yields a splitting efficiency of 50% as illustrated in the figure.

level spectra of the QDs [64, 89]. Neglecting the mutual charging energy due to the capacitive cross-talk between QD1 and QD2 the anti-crossing has a magnitude of  $4\Gamma_{12}$  [64, 89]. When this anti-crossing can not be resolved the level broadening,  $\Gamma \approx \Gamma_N$ , is at least twice as large as the inter-dot coupling and the QDs may be approximated as decoupled.

If the tunnel rate between the QDs is larger than the tunnel rate to the drains,  $\Gamma_{12} \gg \Gamma_{N1}, \Gamma_{N2}$ , the device acts as Cooper pair "beam splitter" [64, 90]. The electrons leave to N1 or N2 at random, in analogy to a optical beam splitter that randomly guides photons into different paths. If the beam splitter is unbiased (i.e. a 50/50 beam splitter,  $\Gamma_{N1} = \Gamma_{N2}$ ) one can achieve a splitting efficiency of 50%, as illustrated in Fig. 3.7. This also marks the upper bound for the efficiency of such a beam splitter device. To achieve efficiencies beyond this threshold the splitting must be enforced by interactions. The inequalities

$$\Delta, U \gg \Gamma, |eV_{SD}|, k_B T \quad \Gamma_N \gg \Gamma_S, \Gamma_{12} \quad (3.12)$$

summarize the working conditions that allow to do so.

### Loss of entanglement

Up to now we have treated the conditions that enforce the splitting of Cooper pairs. The spin-entanglement of the initial Cooper pair is preserved due to the nature of the crossed Andreev process and eventually destroyed

by the inevitable dephasing of the electrons. However, there are also parasitic processes in which one electron of an entangled pair is swapped with another random-spin electron. Such processes would prevent the operation of the device as electron-entangler, even in the case of 100% splitting efficiency and infinite spin-dephasing times. To exclude such processes a sufficiently large level spacing

$$\delta\epsilon \gg \Gamma, |eV_{\text{SD}}|, k_{\text{B}}T \quad (3.13)$$

is required. Otherwise, the QD simply acts as capacitive island: after an entangled electron enters the island any electron from the QD may leave to the N lead, irrespective of spin properties. Furthermore the levels of the QDs should be empty in order to avoid unwanted correlations. Thus QDs which exhibit a clear shell-filling pattern are desirable. Finally, the QD levels might also be occupied by electrons which hopped on from the Fermi leads (electron-hole pair excitations). Such processes, which potentially exchange the entangled electron with an electron from the Fermi leads, may easily happen due to the strong couplings to N1 and N2. To suppress such contributions a sufficiently large bias voltage,

$$|eV_{\text{SD}}| > \Gamma, \quad (3.14)$$

can be applied to position the Fermi edge of the leads well below the QD resonance, while keeping the dots resonant with S, i.e.  $\mu_{\text{S}} = \mu_{\text{QDi}}$ .

### 3.2.2. Quantitative description of the Cooper pair splitter

In reference [84] Recher *et al.* give analytic expressions for the currents from CPS and LPT. These calculations were based on a  $T$ -matrix approach (i.e. the tunnel Hamiltonian was treated perturbatively in all orders). Parts of the calculation use some of the above specified working conditions as approximations. The resulting formula for the CPS current reads

$$I_{\text{CPS}} = \frac{e\Gamma_{\text{S}}^2\hat{\Gamma}}{(\epsilon_1 + \epsilon_2)^2 + \hat{\Gamma}^2/4} F(\delta r), \quad (3.15)$$

where  $\epsilon_1$  ( $\epsilon_2$ ) is the energy level of the QD1 (QD2),  $F(\delta r)$  is a geometrical factor that depends on the separation of the tunnelling points and  $\Gamma_{\text{S}} = \Gamma_{\text{S1}} = \Gamma_{\text{S2}}$ , while  $\hat{\Gamma} = \Gamma_{\text{N1}} + \Gamma_{\text{N2}}$ . The current depends on the level position of both QDs, as one should expect for such a correlated two-particle effect. For  $\epsilon_1 = -\epsilon_2$  the two-particle Breit-Wigner resonance takes its maximal value:

$$I_{\text{CPS}} = \frac{4e\Gamma_{\text{S}}^2}{\hat{\Gamma}} F(\delta r). \quad (3.16)$$

The local current is given by

$$I_{\text{LPT},i} = \frac{2e\Gamma_S^2\Gamma_{Ni}}{\mathcal{E}^2}, \quad \frac{1}{\mathcal{E}} = \frac{1}{\pi\Delta} + \frac{1}{U} \quad (3.17)$$

where the label  $i = 1, 2$  refers to the respective QD. When setting  $\Gamma_N = \Gamma_{N1} = \Gamma_{N2}$  we see that the local current is suppressed by a factor

$$\frac{I_{\text{LPT}}}{I_{\text{CPS}}} \propto \left(\frac{\Gamma_N}{\mathcal{E}}\right)^2. \quad (3.18)$$

The term  $\Gamma_S^2$  drops out, since LPT and CPS both require the tunnelling of two electrons through the barrier on the S side.

### The spatial decay of CPS

The chance for a CPS event scales with a geometry dependent factor  $F(\delta r)$ , where  $\delta r$  is the spatial separation of the two tunnelling points in S.<sup>3</sup> It is intuitively clear that  $F(\delta r)$  will decay rapidly when  $\delta r$  exceeds the coherence length  $\xi_0$ . However, the relevant form of factor  $F(\delta r)$  is ambiguously discussed among researchers.

In reference [84] Recher *et al.* consider a ballistic 3-dimensional superconductor and find

$$F(\delta r) = \left| \frac{\sin(k_F \delta r)}{k_F \delta r} \right|^2 \exp \left[ -\frac{2\delta r}{\pi \xi_0} \right], \quad (3.19)$$

with  $k_F$  being the Fermi wavevector in S and  $\xi_0$  being the coherence length. This result is well in agreement with an earlier calculation by Falci *et al.* [83]. The CPS rate decays exponentially with the distance  $\delta r$  on a scale given by the coherence length  $\xi_0$ . The latter is typically up to several hundred nanometers, which lies well within the reach of modern fabrication techniques. However, the algebraic pre-factor  $(k_F \delta r)^{-2}$  in Eq. (3.19) poses a severe problem for the efficiency of a Cooper pair splitter. The short Fermi wavelengths in S, which is typically on the order of Ångström, implies an additional suppression on the order of  $\sim 10^{-7}$  for a realistic spatial separation of  $\delta r = 150$  nm) between the QDs.<sup>4</sup>

As a more realistic scenario one may consider the diffusive limit where the mean free path in S is shorter than the coherence length,  $l_{\text{mfp}} < \xi_0$ . In the diffusive limit the coherence length is reduced to  $\xi = \sqrt{l_{\text{mfp}} \xi_0}$  and

<sup>3</sup>If the device is realized with a CNT (or a semiconducting nanowire) the order of  $\delta r$  is given by the width of the S contact covering the CNT.

<sup>4</sup>If the spatial separation between the QDs is not sufficiently large the device will usually exhibit a strong inter-dot coupling,  $\Gamma_{12}$ , which leads to the problems discussed above.

the denominator in Eq.(3.19) is replaced by  $(k_F \delta r)^{-1} (l_{\text{mfp}} k_F)^{-1}$  [91]. However, for realistic numbers (e.g.  $\lambda_F = 3.6 \text{ \AA}$ ,  $\delta r = 150 \text{ nm}$  and  $l_{\text{mfp}} = 5 \text{ nm}$  [63]) one still computes a suppression on the order of  $10^{-6}$ . Surprisingly, the observed CPS rates in InAs nanowires [63, 65], as well as in CNTs [64, 66], showed no indication of such an algebraic suppression term. It was therefore speculated that these 3-dimensional calculations are not valid for such confined geometries [63, 69]. We may assume that the CPS tunnelling does not occur at the periphery of the superconducting contact, but instead happens from the wire segment underneath the S contact, which effectively can be viewed as a superconductor by virtue of the proximity effect. Indeed, for a 1-dimensional ballistic superconductor one finds that  $F(\delta r) \propto |\sin(k_F \delta r)| \exp\left[-\frac{2\delta r}{\pi \xi_0}\right]$ , i.e. the problematic term  $(k_F \delta r)^{-2}$  is not present anymore [69, 92].

However, there are also alternative explanations for the absence of a strong geometrical suppression term. As it turns out, Recher *et al.* considered a system, where each QD is coupled to only one conductance channel of S. The algebraic pre-factor  $(k_F \delta r)^{-2}$  is not directly related to superconductivity, but can be viewed as a non-local analogue of a Sharvin resistance: it arises from a summation over all ballistic electron trajectories that connect the two tunnelling points. If CPS can arise not only from two tunnelling points, but from two interface areas  $\mathcal{A}_1$  and  $\mathcal{A}_2$ , then the factor must be multiplied by  $\mathcal{N}_1 \mathcal{N}_2$ , where  $\mathcal{N}_{1,2}$  is the number of conducting channels of the corresponding interface given by  $\mathcal{N}_{1,2} = k_F^2 \mathcal{A}_{1,2} / 4\pi$  [93]. Let us consider that CPS tunnelling does occur at the periphery of S, but from e.g. the last 10 nm of the S contact into a CNT. In this case each contact area provides about 360 conducting channels (on the S side), where we assumed a CNT with 1.5 nm diameter which is fully covered with aluminium ( $\lambda_F = 3.6 \text{ nm}$ ). In this example the we would get  $F(\delta r = 150 \text{ nm}) \sim 10^{-2}$ , i.e. the pre-factor is much less severe, but still present. However, it is not fully clear to the author if the theory from reference [93], which studies NSN structures, can simply be adapted in this manner to describe QD-S-QD devices (after all a CNT-QD only provides only a single conductance channel).

The authors from reference [93] also extended their theory to the experimentally more realistic case of a superconductor in the diffusive limit. Their result for the non-local resistance (again of a NSN structure) reads [94]

$$R_{12} = \frac{R_\xi}{2} \exp[-\delta r / \xi], \quad (3.20)$$

where  $R_\xi$  is the Drude resistance in the normal state over the length  $\xi$ . In contrast to the prior study of Feinberg [91] Eq.(3.20) does not contain any dependence on  $\delta r$ .

In conclusion we note that the geometry dependence of  $I_{\text{CPS}}$  is strongly influenced by the theoretical framework that one chooses to describe the experimental situation (diffusive vs. ballistic limit, number of conducting channels, dimension of the superconductor). From experiments [63–66] it is clear that CPS is not suppressed by an additional pre-factor  $(k_{\text{F}}\delta r)^{-2}$ . However, there are several plausible explanations for the absence of this factor and it is not yet clear which theoretical framework is most appropriate to describe the experimental circumstances that one encounters in such CPS devices.

### 3.3. Andreev bound states

When a QD is strongly coupled to a superconducting electrode the proximity effect can drastically alter the energy spectrum of the QD. In this section we discuss the formation of Andreev bound states (ABSs), a new type of sub-gap energy level that can appear in the spectrum of such QD-S devices. When a weakly coupled normal contact (N) is connected to the QD-S system one can directly observe these new energy levels by means of tunnelling spectroscopy. As we will see, a N-QD-S junction in the limit  $\Gamma_{\text{N}} \ll \Gamma_{\text{S}}$  behaves very different compared to a device which exhibits the coupling asymmetry of an ideal Cooper pairs splitter,  $\Gamma_{\text{N}} \gg \Gamma_{\text{S}}$ .

#### 3.3.1. The superconducting atomic limit

The physics of a QD-S system is usually described within the framework of the superconducting Anderson model. We consider a Hamiltonian of the form [55]:

$$H_{\text{tot}} = H_{\text{QD}} + H_{\text{S}} + H_{\text{TS}}, \quad (3.21)$$

with a single level QD described by

$$H_{\text{QD}} = \sum_{\sigma} \epsilon_{\text{d}} d_{\sigma}^{\dagger} d_{\sigma} + U n_{\uparrow} n_{\downarrow}, \quad (3.22)$$

where  $d_{\sigma}^{\dagger}$  ( $d_{\sigma}$ ) creates (annihilates) an electron with spin  $\sigma$  at  $\epsilon_{\text{d}}$ .  $U$  is the Coulomb interaction, which is only present if the energy level holds two electrons  $n_{\uparrow} = n_{\downarrow} = 1$ , where  $n_{\sigma} = d_{\sigma}^{\dagger} d_{\sigma}$  is the QD's number operator. The superconducting electrode is described by the standard BCS Hamiltonian

$$H_{\text{S}} = \sum_{\mathbf{k}, \sigma} \epsilon_{\mathbf{k}} c_{\mathbf{k}\sigma}^{\dagger} c_{\mathbf{k}\sigma} - \Delta_{\text{S}} \sum_{\mathbf{k}} \left( c_{\mathbf{k}\uparrow}^{\dagger} c_{-\mathbf{k}\downarrow}^{\dagger} + \text{h.c.} \right). \quad (3.23)$$

Here  $c_{\mathbf{k}\uparrow}^{\dagger}$  ( $c_{\mathbf{k}\uparrow}$ ) creates (annihilates) an electron with wavevector  $\mathbf{k}$  and spin  $\sigma$  in S and  $\Delta_{\text{S}}$  is the energy gap. The last term in  $H_{\text{tot}}$  is the tunnel

Hamiltonian that couples the lead and the QD:

$$H_{T_S} = t_S \sum_{\mathbf{k}, \sigma} \left( d_{\sigma}^{\dagger} c_{\mathbf{k}, \sigma} + \text{h.c.} \right). \quad (3.24)$$

The tunnelling probability  $t_S$  is related to the coupling constant via  $\Gamma_S = 2\pi t_S^2 \rho_0$ , where  $\rho_0 = 1/2D$  is a constant DOS in the an energy window  $[-D, D]$  around the Fermi energy. One can easily include a second lead into the model by adding additional terms  $H_{S2} + H_{T_{S2}}$  to Eq. (3.21). Normal conducting leads can be described analogously by setting  $\Delta_S = 0$  for the respective lead.

The above Hamiltonian  $H_{\text{tot}}$  has no exact solution. It must be treated either with sophisticated numerical methods or in restricted parameter regimes that allow an analytic solution. The easiest approximation one can make is called the atomic limit. One takes the tunnel coupling to zero,  $t_S \rightarrow 0$ , which decouples the lead and the QD. The Hamiltonian of the decoupled QD,  $H_{\text{QD}}$ , has four eigenstates,  $\{|0\rangle, |\uparrow\rangle, |\downarrow\rangle, |\uparrow\downarrow\rangle\}$ , which give rise to the well-known energy spectrum shown in Fig. 3.8(a). The spectral density of the QD exhibits sharp peaks at  $\epsilon_d$  and  $\epsilon_d + U$  which correspond to the (first order) transitions between these states. The atomic limit gives the typical behaviour of a QD in the Coulomb blockade regime, but evidently all superconductivity related phenomena are lost. Theoreticians therefore developed a so-called *superconducting atomic limit*, where the decoupling between the lead and the dot is achieved by increasing the bandwidth,  $D \rightarrow \infty$ , and taking the limit  $\Delta_S \rightarrow \infty$ . It was shown that in this case one can consider a local effective Hamiltonian [95–97]

$$H_{\text{eff}} = H_{\text{QD}} - \frac{\Gamma_S}{2} (d_{\uparrow}^{\dagger} d_{\downarrow}^{\dagger} + d_{\uparrow} d_{\downarrow}) \quad (3.25)$$

in analogy to the usual atomic limit. This Hamiltonian accounts for the proximity effect by an additional term that creates and destroys Cooper pairs on the QD. This new term occurs because Cooper pairs constantly tunnel back and forth between S and the QD via virtual Andreev reflections [Fig. 3.8(b)]. By comparing the local effective Hamiltonian to the BCS Hamiltonian from Eq. (3.23) we see that the coupling constant  $\Gamma_S$  plays the role of the pairing energy  $2\Delta$  for the proximitized QD. We therefore obtain physically meaningful results, even though the limit  $\Delta \rightarrow \infty$  may seem unphysical. The critical reader should try to look at the superconducting atomic limit as a convenient mathematical method to neglect quasiparticle interactions and not as case study of a hypothetical superconductor with infinite pairing energy.

The virtual Andreev reflections couple the even charge states of the QD and hence  $|0\rangle$  and  $|\uparrow\downarrow\rangle$  are no longer eigenstates of  $H_{\text{eff}}$ . In contrast,  $|\sigma\rangle$

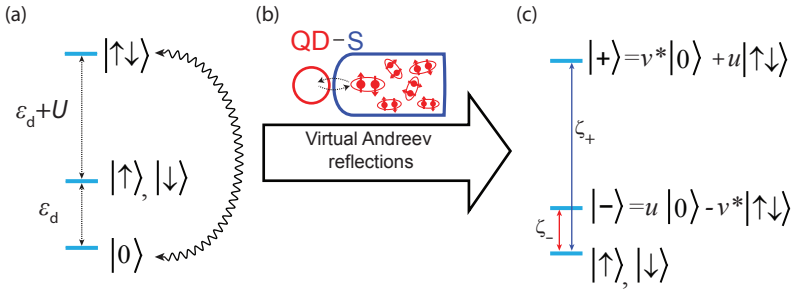


**Figure 3.8.:** (a) Energy spectrum of a single level QD in the atomic limit. (b) Virtual Andreev reflections couple the even charge states of the QD [curly arrow in (a)]. (c) Energy spectrum of the coupled QD-S system in the superconducting atomic limit.  $\zeta_-$  and  $\zeta_+$  are the elementary excitation energies of the system.

( $\sigma = \uparrow, \downarrow$ ) remains an eigenstate. However, the proximity term in  $H_{\text{eff}}$  shifts the respective eigenenergy to  $E_\sigma = \epsilon_d + U/2$ , which lies half way between the energy levels  $E_0$  and  $E_{\uparrow\downarrow}$  of the uncoupled QD. For the sake of convenience we introduce a new variable  $\delta = \epsilon_d + U/2$  which accounts for this electron-hole (e-h) symmetry.

$H_{\text{eff}}$  can be diagonalized by means of a Bogoliubov transformation, a consequence of the formal analogy with the BCS Hamiltonian. The new eigenstates are

$$\begin{aligned} |-\rangle &= u|0\rangle - v^*|\uparrow\downarrow\rangle \\ |+\rangle &= v^*|0\rangle + u|\uparrow\downarrow\rangle \end{aligned} \quad (3.26)$$

with the Bogoliubov-de Gennes (BdG) amplitudes  $u = \frac{1}{2}\sqrt{1 + \delta/\sqrt{\delta^2 + \Gamma_S^2}}$  and  $v = \frac{1}{2}\sqrt{1 - \delta/\sqrt{\delta^2 + \Gamma_S^2}}$  [95–97]. The two BCS-like states  $|\pm\rangle$  are called Andreev bound states and their energy is given by<sup>5</sup>

$$E_\pm = \frac{U}{2} \pm \sqrt{\delta^2 + \Gamma_S^2} + \delta. \quad (3.27)$$

The top panel of Fig. 3.9 shows the evolution of the energy levels of the coupled QD,  $E_\sigma$ ,  $E_-$  and  $E_+$ , with the gate-tunable dot energy  $\epsilon_d$  in units of  $U$ . The two dashed lines are the energy levels of the uncoupled QD

<sup>5</sup>To emphasize that the QD and S are no longer individual entities one could also write the ABSs in the form  $|-\rangle = u|0\rangle \otimes |\mathcal{N}\rangle - v^*|\uparrow\downarrow\rangle \otimes |\mathcal{N}-1\rangle$ , where  $\mathcal{N}$  is the number of Cooper pairs in S. However, we won't write this entanglement between QD and S explicitly.

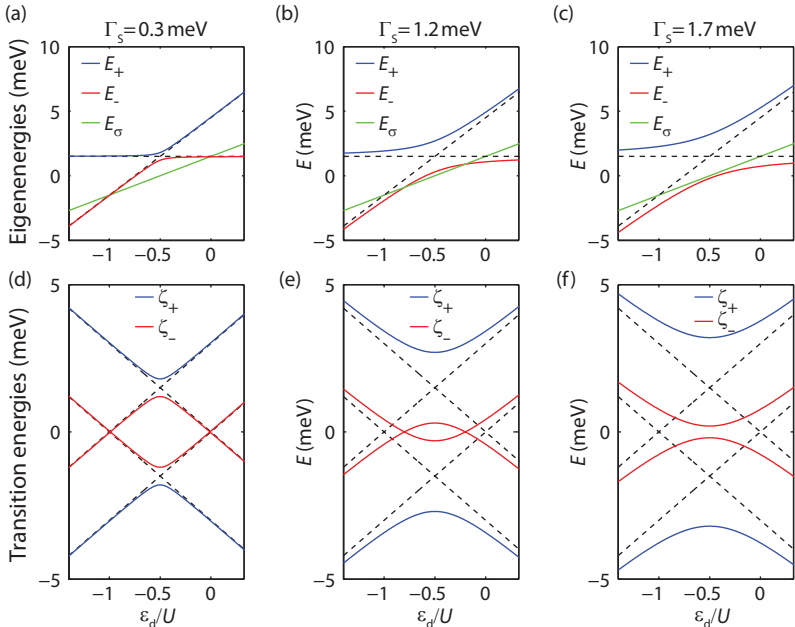


**Figure 3.9.:** Excitation energies (top panel) and energy levels (bottom panel) of  $H_{\text{eff}}$  for  $U = 3 \text{ meV}$  and (a,d)  $\Gamma_S = 0.3 \text{ meV}$ , (b,e)  $\Gamma_S = 1.2 \text{ meV}$  and (c,f)  $\Gamma_S = 1.7 \text{ meV}$ . The dashed lines in the top panel correspond to  $E = \pm \epsilon_d$  and  $E = \pm(\epsilon_d + U)$ . The two dashed lines in the bottom panel give the eigenenergies of the uncoupled QD shifted by  $U/2$ .

shifted by  $U/2$ , i.e.  $E_0 = U/2$  and  $E_{\uparrow\downarrow} = 2\epsilon_d + 3U/2$ . We see that the ABS energies follow the uncoupled states  $|0\rangle$  and  $|\uparrow\downarrow\rangle$ , but obey and avoided crossing as a result of the tunnel coupling between these two states. As the coupling strength  $\Gamma_S$  is increased the gap between  $|+\rangle$  and  $|-\rangle$  grows, while the energy of the  $|\sigma\rangle$  state remains unaffected [Fig. 3.9(a-c)]. At some point the energy gap is so large that  $E_-$  is pushed below  $E_\sigma$  for all values of  $\epsilon_d$ .

In transport experiments one measures transitions between two energy levels, rather than individual energy levels by themselves. Figure 3.8(c) shows the two elementary transitions  $|\sigma\rangle \leftrightarrow |-\rangle$  and  $|\sigma\rangle \leftrightarrow |+\rangle$  with excitation energies  $\zeta_-$  and  $\zeta_+$ . In the  $|\sigma\rangle$  state the QD holds an odd number of electrons, while  $|+\rangle$  and  $|-\rangle$  have an even parity of the charge state. Transitions between  $|+\rangle$  and  $|-\rangle$  are thus second order processes that have a much lower probability than the first order transitions  $|\sigma\rangle \leftrightarrow |\pm\rangle$ .

The excitation energies  $\zeta_{\pm}$  can be measured by tunnelling spectroscopy: when a normal conducting tunnel probe is connected to the QD-S hybrid the differential conductance shows peaks at  $|e|V_{\text{SD}} = \pm\zeta_{\pm}$ . We refer to these differential conductance peaks as *Andreev resonances*<sup>6</sup>. The respective transport mechanisms are discussed in detail in Chapter 7. For the moment our interest is focused on the energy dispersion of these Andreev resonances plotted in the bottom panel of Fig. 3.9. We see that  $\zeta_+$  (blue curve) always lies above  $\zeta_-$  (red curve). In the language of molecular physics  $|-\rangle$  corresponds to the bonding and  $|+\rangle$  to the anti-bonding orbital. We also find that the energy of the  $|-\rangle$  state can either lie below or above  $E_{\sigma}$ . At the points where  $E_-$  and  $E_{\sigma}$  cross the QD undergoes a ground state (GS) transition and also the Andreev resonances  $\zeta_-$  and  $-\zeta_-$  cross each other at zero energy. For large couplings  $\Gamma_{\text{S}}$  the pairing term in  $H_{\text{eff}}$  becomes so strong that the system always remains in the  $|-\rangle$  GS, i.e. the QD chooses to be in a singlet state regardless of the charging energy  $U$ , which favours the doublet  $|\uparrow\rangle, |\downarrow\rangle$  as the GS.

### 3.3.2. Finite superconducting gap

In case of a finite  $\Delta$  the presence of quasiparticles greatly complicates the theoretical treatment of the problem. Interactions with quasiparticles renormalize the energy spectrum and modify the dispersion of the Andreev resonances  $\zeta_{\pm}$  [95, 96, 98, 99]. In Fig. 3.10(a-c) we qualitatively sketch experimentally realistic stability diagrams for N-QD-S devices in the limit  $\Gamma_{\text{N}} \ll \Gamma_{\text{S}}$  for different values of  $\Gamma_{\text{S}}$ . At bias voltages that exceed the gap energy,  $|eV_{\text{SD}}| > \Delta$ , one observes the usual Coulomb diamond pattern (one line of the diamond follows the Fermi level of N, the other line follows the quasiparticle peak in the DOS of the superconductor). For  $|eV_{\text{SD}}| < \Delta$  one observes a mirror symmetric pair of Andreev resonances at  $\pm\zeta_-$ . The transition to the  $|+\rangle$  can usually not be observed because  $E_+ > \Delta$  (recently the first spectroscopic observation of the  $|+\rangle$  was reported, however, Bretheau *et al.* used superconducting atomic contacts, i.e.  $U = 0$ , instead of QDs [100]).

A key difference between the finite  $\Delta$  scenario [Fig. 3.10(a-c)] and the  $\Delta \rightarrow \infty$  limit [Fig. 3.9(d-f)] is that  $\zeta_-$  remains bound to  $\zeta_- < \Delta$  and can not grow arbitrarily. Let's consider the sub-gap spectrum in the regions where  $n = 0$  and  $n = 2$ . In these regions the  $|-\rangle$  state is nearly identical with the uncoupled  $|0\rangle$  and  $|\uparrow\downarrow\rangle$  states (i.e.  $|u| \approx 1$  for  $n = 0$  and  $|v| \approx 1$  for

<sup>6</sup>In the literature the transition energies  $\zeta_{\pm}$  (or the respective poles of the Green's functions) are often called Andreev bound states, too. The reading of literature can become quite confusing if one is not aware of this fact. Here we use the term "Andreev bound state" only for the actual energy levels  $|\pm\rangle$ .

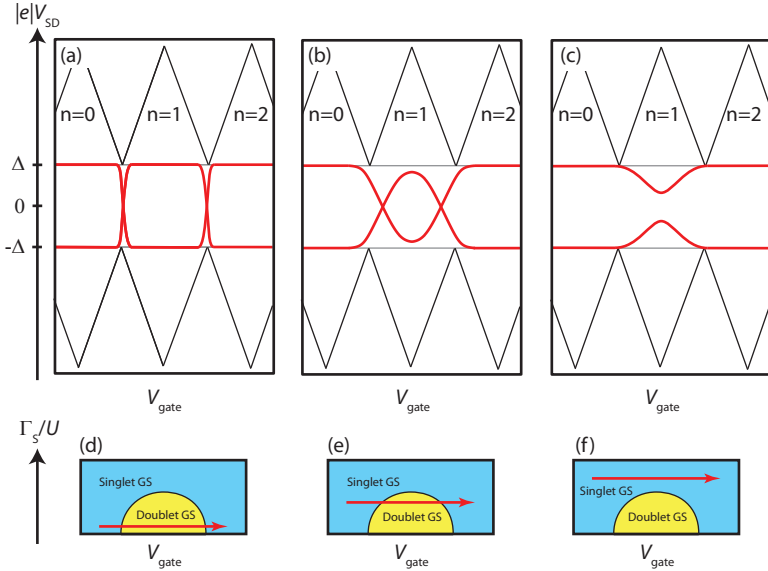


**Figure 3.10.:** (a-c) Qualitative sketches of the stability diagrams for N-QD-S devices in the  $\Gamma_N \ll \Gamma_S$  regime. The red lines depict the Andreev resonances, the black lines depict the conventional Coulomb diamonds. The coupling  $\Gamma_S$  increased from (a) to (c). (d-f) Qualitative sketches of phase diagram that predict the GS as a function of  $\Gamma_S/U$  and gate voltage. Each of the phase diagrams corresponds to the above stability diagram.

$n = 2$ ). In the  $\Delta \rightarrow \infty$  case the energy of the singly occupied state lies much higher than that of the  $|-\rangle$  state. For a finite gap the Andreev resonances have the maximal possible energy, i.e. they are pinned to the gap,  $\zeta_- \approx \Delta$ . The more interesting region lies within  $n = 1$  diamond, where Coulomb repulsion favours an odd GS but the superconducting pairing would prefer the  $|-\rangle$  GS. This competition can be illustrated by the phase diagrams shown in Fig. 3.10(d-f). The effect of the Coulomb repulsion is largest in the middle of the  $n = 1$  diamond where the distance to the even charge states maximal. The larger the ratio  $\Gamma_S/U$ , the deeper one can enter into the  $n = 1$  diamond before the  $|\sigma\rangle$  state becomes the ground state.

When  $\Gamma_S/U$  is increased there will be a critical ratio for which the  $|-\rangle$  state always remains the GS of the system. Above this threshold value the Andreev resonances don't cross anymore [Fig. 3.10(c,f)]. In the limit of very small ratios  $\Gamma_S/U$  the transition between the different GS occurs very

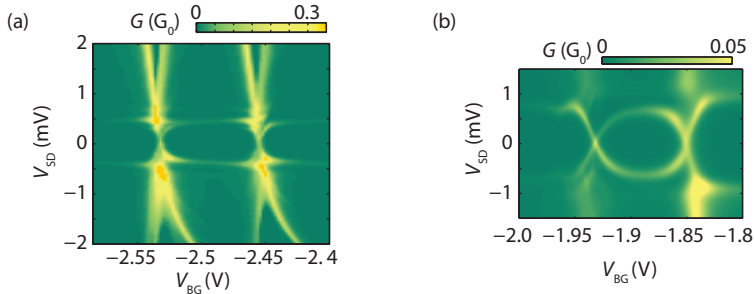


**Figure 3.11.:** Differential conductance maps of a N-QD-S device in the  $\Gamma_N \ll \Gamma_S$  regime. The device was made from a CNT with Ti/Nb (3 nm/50 nm) and Ti/Au (5 nm/50 nm) contacts and measured at a base temperature of 25 mK. The situation in (a) corresponds to Fig. 3.10(a,d). In (b) the coupling to S was stronger. The Andreev resonances are well resolved in correspondence with Fig. 3.10(b,e).

rapidly [Fig. 3.10(a,d)]. In this case  $\zeta_-$  quickly runs into  $\Delta$ . Now the Andreev resonances fall together with the quasiparticle edge, also inside the  $n = 1$  diamond. This explains why the experimental observation of ABSs happened only recently [56, 101], although the effective Hamiltonian from Eq. (3.25) always exhibits ABSs: for small  $\Gamma_S/U$  the splitting between the Andreev resonances becomes very small and can not be resolved anymore due to the lifetime broadening  $\Gamma_N$  induced by the tunnel probe. Figure 3.11(a) shows a stability diagram, measured on a CNT QD connected to a superconducting niobium lead and a normal conducting Ti/Au tunnel probe, in the regime of Fig. 3.10(a,d). At the charge degeneracy points ( $n = 0/1$  and  $n = 1/2$ ) the evanescent features of the ABS can just be resolved within the given linewidth. Off-resonance the Andreev resonance can not be distinguished from the onset of the quasiparticle co-tunnelling current. Figure 3.11(b) shows the same device, but at a different gate position where the coupling to S was stronger. The Andreev resonances are well resolved in correspondence with Fig. 3.10(b,e). For the regime of Fig. 3.10(c,f) we have no own experimental data. We thus must refer the reader to the beautiful data presented in Ref. [56, 72].



## Device fabrication and measurement set-up

The fate of a PhD student who is working in the field of nanoelectronics to a large fraction is decided in the clean room. A "good" sample – or at least a working sample – is certainly a prerequisite for any experiment. But the small size of the devices makes the fabrication process very sensitive to external perturbations and intrinsic sample-to-sample variations. In this chapter we introduce the basic fabrication process for CNT based QDs. Detailed recipes are given in Appendix A. The chapter closes with a brief description of the used measurement set-ups.

### 4.1. Standard fabrication process

**Wafer preparation.** All devices in this thesis are fabricated on a highly doped silicon wafer capped with a  $400\ \mu\text{m}$  thick layer of thermally grown oxide. The wafer is cut into pieces of about  $1 \times 1\ \text{cm}^2$  size and thoroughly cleaned.

**Carbon nanotube growth.** We use chemical vapour deposition (CVD) to grow single walled CNTs on the wafer [102, 103]. To do so we spin coat nanoparticles of an iron based catalyst solved in isopropyl alcohol (IPA) onto the wafer. The wafer is placed in a CVD reactor and heated to  $950^\circ\text{C}$  under 1500 sccm of argon flow. When the growth temperature is reached argon atmosphere is replaced by methane at a flow rate of 1000 sccm and

hydrogen at flow rate of 500 sccm. The methane dissociates at the catalyst particles, providing the carbon for the nanotube growth. The addition of hydrogen helps to reduce the amount of bundled CNTs [103]. The chosen parameters for the CVD growth are based on experience [103, 104]. Detailed models of the growth process are still ongoing research, see e.g. [105] and references therein. After 10 min growth time we replace the methane by argon and let the furnace cool down to room temperature.

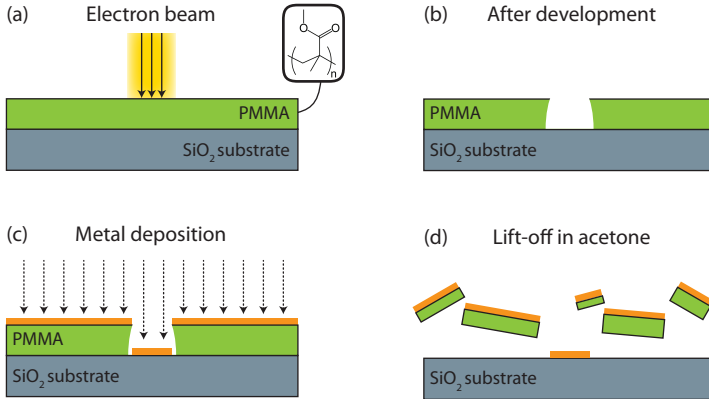


**Figure 4.1.:** Illustration of a standard e-beam lithography process. a) The substrate is covered with PMMA resist and exposed to an electron beam that writes the desired pattern into the resist. The inset shows the structural formula of PMMA chains. (b) After development a patterned resist mask remains. (c) Metal deposition. (d) Lift-off in acetone dissolves the PMMA mask and leaves a patterned metal film.

**EBL step 1: alignment markers.** After CNT growth we use standard electron-beam lithography (EBL) to pattern marker grids onto the wafer which serve later as coordinate system. The spacing between the markers is  $10\ \mu\text{m}$  and each grid consists of  $10 \times 10$  markers that fill an area of  $0.1 \times 0.1\ \text{mm}^2$ . The basic principle of EBL is illustrated in Fig. 4.1. We use polymethyl methacrylat (PMMA) solved in chlorobenzene as lithography resist. The resist is spin-coated onto the wafer and baked on a hot plate at  $180^\circ\text{C}$  for 2 min. Then the wafer is placed in a scanning electron microscope (SEM), where a highly focused electron-beam (e-beam) writes the desired structure into the resist [Fig. 4.1(a)]. PMMA is a long-chained polymer that is available in different molecular weights from 50000 (50K) to 950000 (950K).

The e-beam cuts the polymer chains of the resist into short segments (chain-scission) and a developer, typically a 1:3 mixture of methyl isobutyl ketone (MIBK) and IPA, is used to wash out the light-weighted polymer fragments [Fig. 4.1(b)]. The remaining resist acts as a mask for metallization [Fig. 4.1(c)]. For the marker grid we usually evaporate Ti/Au (5 nm/30 nm) in an e-beam evaporator. A bath in hot acetone removes the PMMA mask and only the desired structure, the area where the resist was opened beforehand, remains on the wafer [Fig. 4.1(d)]. In tenacious cases we help the lift-off process with a syringe which is used to create turbulent flow in the acetone bath and "blow off" the sticky parts.

**CNT localization.** We use SEM imaging to locate individual CNTs with respect to the marker grid. Under the irradiation of the scanning e-beam the insulating substrate charges. The conducting CNTs act as additional capacitances, leading to a much slower charging of the substrate below them [106]. Thus, a positively charged shadow of the CNT becomes visible. An optimal contrast is achieved by using the in-lens detector and low acceleration voltages (0.5-2 keV). We select individual CNTs of appropriate length which we plan to contact. The CNTs are chosen randomly. It is usually not possible to distinguish between single- or multi-wall, metallic or semiconducting and defect rich or pristine CNTs from the charge shadow the CNT leaves on the SiO<sub>2</sub> substrate.

**EBL steps 2 + 3: building a Cooper pair splitter from a CNT.** The positions of the CNTs are transferred into a GDSII-file where contacts and gates can be designed as illustrated in Fig. 4.2(a). In case of a Cooper pair splitter device at least two more EBL steps are required.

In the first EBL step we fabricate the central contact, using a metal which becomes superconducting at low temperatures. For the devices presented in this thesis we used either Al or Nb. Since both of these materials make only very poor contact to CNTs a thin contact layer below the superconductor is required. Pd and Ti with thicknesses between 3 and 5 nm have proven successful for this purpose. Pd/Al bilayers were evaporated thermally in a UHV system at  $\sim 10^{-10}$  mbar. Ti/Nb bilayers were sputtered. To avoid damage of the CNT we sputtered the contact layer at a rather high background gas pressure of 15 mTorr ( $\approx 2 \cdot 10^{-2}$  mbar), at which the Ti atoms lose a large fraction of their kinetic energy in collisions with the working gas (Ar with a flow rate of 35 sccm). The central contact is connected from both sides to bond pads, which allows to determine the critical temperature of the superconductor by two-terminal conductance measurements. We fabricate bond pads, shown in Fig. 4.2(b), and CNT contacts in the same EBL

step, using to different apertures (typically  $10\ \mu\text{m}$  and  $120\ \mu\text{m}$ ) of the SEM.

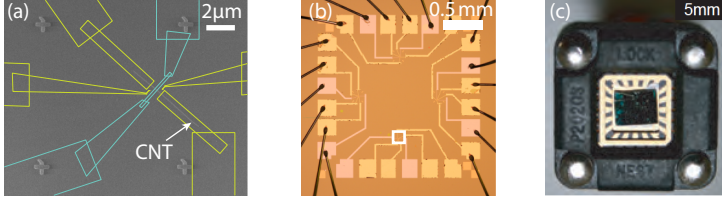


**Figure 4.2.:** (a) SEM image of an individual CNT with the design for a CPS device with side gates. The four alignment markers uniquely determine the position within a grid of  $10 \times 10$  markers that fill the area marked by a white square in (b). (b) Optical microscope image of a chip with 4 CPS devices. Each device is connected to 6 bond pads. The chip is glued into a chip-carrier and contacted with a wafer bonder. (c) Image of a chip-carrier in the socket of a cryostat (source for image (c): reference [85]).

In a second EBL step we fabricate the two normal conducting drain contacts and two side gates, using either Pd or Ti/Au ( $5\ \text{nm}/50\ \text{nm}$ ). To exclude the formation of different Schottky barriers at source and drain (e.g. n-type contact to source and p-type contact to drain) we use the same wetting material as for the superconducting contact. The materials are evaporated either by e-beam or by thermal evaporation.

In a last step the  $1 \times 1\ \text{cm}^2$  wafers are cut into  $4 \times 4\ \text{mm}^2$  pieces and glued into chip-carriers. The chip-carriers fit into sockets at the cryostats which are electrically connected to 20 measurement lines [Fig. 4.2(c)]. The electrical connection between bond pads and chip-carrier is achieved with a wire bonder. The contact to the backgate is made by scratching the oxide and sealing the scratch with silver-paint. We chose to fabricate 4 CPS devices per chip, with 6 terminals per device. Since the chip-carrier provides 20 terminals (from which one is needed to contact the back gate) we can maximally bond three devices per chip. To decide which devices will be bonded we measure the room temperature conductance of each device with a needle prober station.

## 4.2. Residues from lithography resist

It is a well known fact that organic lithography resists often leave polymer residues on the substrate surface. Figure 4.3(a) shows AFM images of PMMA(80K) residues that remained after exposure and development of the resist [107]. The authors of reference [107] found that granular residues of up to  $10\ \text{nm}$  height remained on the Si substrate after EBL processing with a standard recipe similar to the one given in appendix A.5. As the dose

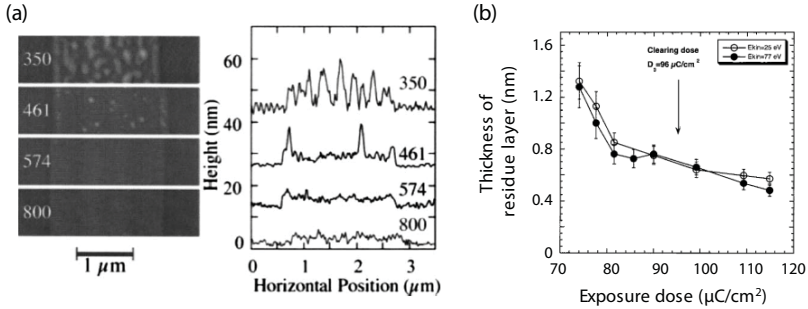


**Figure 4.3.:** (a) AFM images and height profiles of residues that remained after exposure and development of PMMA(80K). For exposure doses of 350 and 461  $\mu\text{C}/\text{cm}^2$  the granular residues with up to 10 nm height are observed. A continuous residue layer (2.5 – 3.2 nm) remains for all exposure doses up to 800  $\mu\text{C}/\text{cm}^2$ . Source: reference [107]. (b) Measurement of the thickness of the residue layer of 150 nm PMMA(50K) on a  $\text{SiO}_2$  substrate. The thickness is extracted from the intensity decrease of  $\text{SiO}_2$  peaks in photoemission spectra. Source: reference [108].

is increased granules get smaller and fewer and finally vanish.<sup>1</sup> However, the AFM profiles in Fig. 4.3(a) show that these granules lie on a plateau of about 3 nm height. This plateau remains visible even when the resist is overexposed with a dose of 800  $\mu\text{C}/\text{cm}^2$  before development. Similar findings are reported in reference [108], where the thickness of the residual layer from 150 nm of PMMA(50K) on  $\text{SiO}_2$  is measured as a function of the exposure dose, see Fig. 4.3(b). By using photoemission spectroscopy and interpreting the intensity decrease in the  $\text{SiO}_2$  spectra the authors conclude that the substrate surface remains covered with a 0.5 nm thick residue layer even at overexposed conditions.

It is obvious that polymer residues between the CNTs and the contact metal might degrade the contact properties or even prevent electron conduction. Usually resist residues (and other organic contaminants) are cleaned by an oxygen plasma ash or by UV ozone cleaning [107]. However, these conventional cleaning schemes are not suitable for carbon-based electronics. The ion bombardment from the plasma, as well as the oxidation by O radicals also attack CNTs and eventually remove them.

<sup>1</sup>Such granular PMMA residues have a tendency to remain sticking to CNTs. The chargeable PMMA granules are visible in the SEM where they appear as dark spots on the CNTs, see reference [109], p. 34.

### 4.2.1. Minimizing resist residues

To minimize resist residues from EBL one may increase the exposure dose to the highest tolerable values. The rationale behind this idea is that the resist polymers are fragmented into smaller and more uniform pieces. Shorter polymer chains dissolve more easily and leave less residues [110]. This strategy is also applied by groups that are interested in high resolution EBL: in the sub-10 nm regime the same polymer clusters that leave granular residues also limit the resolution and cold development [110] or less sensitive developers [111] are used to increase the clearing dose. Instead of increasing the dose one may also decrease the molecular weight of the resist.<sup>2</sup> For our purposes resolution is not the major concern and the usage of a resist bilayer, as schematically shown in Fig. 4.4, seems the best option. A thin top layer of PMMA with a molecular weight of 950K gives the resolution of the resist mask. A thick bottom layer of PMMA with a molecular weight of 50K is heavily overexposed, which helps to minimize residues and creates a nice undercut to ease lift-off.

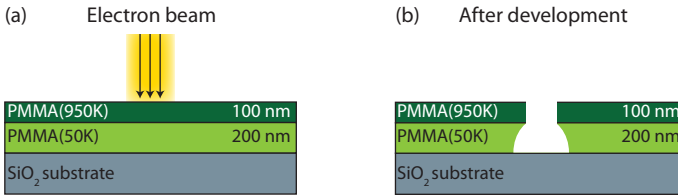


**Figure 4.4.:** A resist double with thin layer of high molecular weight on top of a thick layer with low molecular weight allows to overexpose the bottom layer without losing resolution. This procedure increases the surface cleanliness and creates an undercut to help lift-off. Schematic drawing (a) during exposure and (b) after development.

The amount of residues may also be minimized by choosing an appropriate resist. Several products based on different polymers are on the market. In the beginning of this thesis we used bilayers of PMMA(950K) and the copolymer PMMA-MA 33% from Allresist (serial number AR-P 617.03). This combination gave good lift-off and nicely defined structures, but the yield of good electrical contacts to the CNTs was very poor. In the meanwhile people in our group made very good experience with ZEP-520A from Zeon as single layer resist [112]. However, even ZEP leaves residues, as

<sup>2</sup>The molecular weight  $M^*$  of the fragmented polymers can be calculated as  $M^* = \left(\frac{1}{M} + \frac{gD}{\rho N_A}\right)^{-1}$ , where  $M$  is the initial molecular weight of PMMA resist and  $D$  is the dose,  $g$  indicates the chain scission efficiency,  $\rho$  is the density of PMMA and  $N_A$  is Avogadro's number [110].

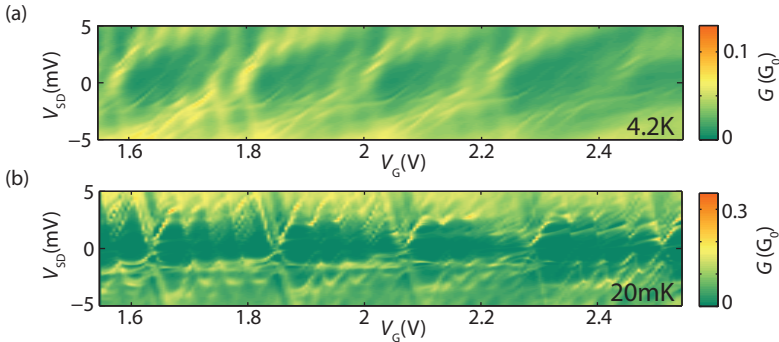


**Figure 4.5.:** Stability diagram of a CNT QD measured in the same set-up at two different temperatures: (a) 4.2 K and (b) 20 mK. The image illustrates the importance of sufficiently low temperatures for transport experiments.

can be concluded AFM measurements of the surface roughness which increased up to 15 nm (rms) after exposure and development of ZEP [113]. It is therefore highly desirable to test novel fabrication schemes which avoid or remove organic contaminations. Chapter 5 discusses some attempts in this direction.

### 4.3. Measurement set-up

The electronic properties of a device can only be resolved if the electron Temperature is well below the relevant energy scale, such as the charging energy  $U$ , the level spacing  $\delta E$ , the lifetime broadening  $\Gamma$  and, if superconductivity is involved, the energy gap  $\Delta$ . Several cryogenic set-ups, with base temperatures ranging from 4.2 K to 20 mK, were available for this PhD project. Figure 4.5 illustrates the importance of a sufficiently low temperature: the stability diagram of a CNT QD is measured at 4.2 K and a second time at  $T_{\text{base}} \approx 20$  mK in the same cryostat (i.e. with the same filtering). The charging energy is about  $5 \text{ meV}/k_B \approx 60$  K, but still the resolution drastically increases as the temperature is lowered below 4.2 K until the lifetime broadening is reached, which is typically  $\Gamma/k_B \sim 1$  K. Furthermore, coherent effects, such as Cooper pair splitting, are often very fragile and require even lower temperatures (see Ref. [63] and Fig. 7.4).

A temperature of 4.2 K can be reached with relatively little effort by dipping the sample into liquid  $^4\text{He}$ . To lower the temperature one can pump on the helium bath. The "hottest" particles boil away and the liquid is

cooled. The lowest temperature that is reachable by this evaporative cooling is determined by the respective vapour pressure curve. By pumping on  $^4\text{He}$  one can lower the temperature down to 1.2 K. The rare (and expensive) isotope  $^3\text{He}$  has a lower boiling point that allows to conveniently reach temperatures around 230 mK in a so-called  $^3\text{He}$  cryostat. Even lower temperatures can be reached with dilution refrigerators that use a mixture of  $^3\text{He}$  and  $^4\text{He}$ . Below  $\sim 870$  mK the mixture undergoes a phase separation into a  $^3\text{He}$ -rich and a  $^3\text{He}$ -poor phase. With a cleverly designed pumping and cooling scheme, described e.g. in [114], one can create an osmotic pressure difference that drives  $^3\text{He}$  from concentrated to the dilute phase. The  $^3\text{He}$  "evaporates" into the  $^4\text{He}$  (which can effectively be viewed as  $^3\text{He}$  gas). The achievable temperatures are given by the phase diagram of  $^3\text{He}/^4\text{He}$  mixtures and the dilution refrigerators that are available in our group reach base temperatures around  $\sim 20$  mK.

To perform transport measurements one inevitably has to connect the sample, which is held in the cryogenic environment, with the necessary read out electronics at room temperature. The measurement lines thus form a heat leak. At very low temperatures the phonon lattice of the sample, which is cooled by the cryostat, can not fully take up the heat transferred through the measurement lines: the electron and phonon temperatures decouple,  $T_{\text{el}} > T_{\text{ph}}$ . For the used dilution refrigerators we assume very roughly  $T_{\text{el}} \sim 100$  mK for  $T_{\text{el}} \approx 20$  mK. To keep the heat leak as small as possible the measurement lines are thermally well anchored and strongly filtered (a temperature of 100 mK corresponds to a frequency  $f = Tk_{\text{B}}/h \approx 2$  GHz). We use a two-stage filter set-up consisting of a specifically designed tape-worm filter at cryogenic temperature [115] and commercial  $\pi$ -filters from Syfer at room temperature. The cut-off from the tape-worm filter starts at  $f > 10$  MHz, that of the  $\pi$ -filter at  $f > 1$  MHz. A schematic of the complete measurement set-up is shown in Fig. 4.6.

The gates are addressed by low noise DC voltage sources (either Yokogawa YK 7651 or homebuilt 8-channel low-noise DAC). The gate voltages run through a 1 M $\Omega$  resistor to protect the sample from high currents in case of a spontaneous formation of a gate leak during the measurement. To bias the sample we use a DC voltage superposed with a small AC excitation, typically around  $V_{\text{AC}} \sim 10\mu\text{eV}$ , which is provided from a lock-in amplifier (Stanford SR 830) and added to the DC signal by a transformer with a 1:4 winding ratio. In addition a voltage divider with a 1:1000 ratio is mounted directly before the  $\pi$ -filter on the break-out box. The frequency of  $V_{\text{AC}}$  is limited by the line capacitances and we typically chose  $f = 135$  Hz or lower. For a CPS device we read out two currents simultaneously, by two homebuilt current-to-voltage (I/V) converters with a transimpedance of  $10^7$  V/A or  $10^8$  V/A. The output voltage of the I/V converters is fed to two separate

SR 830 lock-in amplifiers, both phase-locked to the same frequency. The set-up is controlled with a computer via Labview programs and a General Purpose Interface Bus (GPIB).

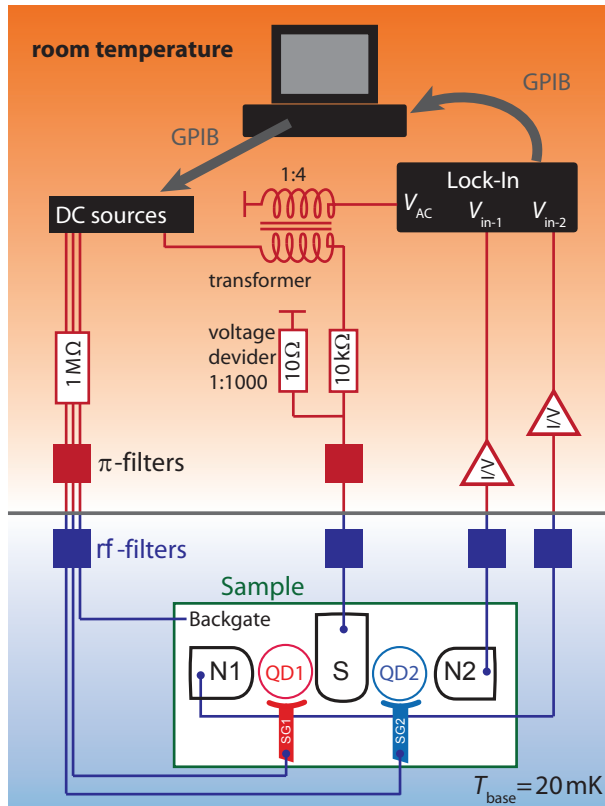


**Figure 4.6.:** Typical measurement set-up for voltage biased differential conductance measurements on parallel QD devices. Adapted from [109].

## Novel fabrication approaches

The most spectacular results in CNT research – the discovery of spin-orbit interactions [116], the formation of a 1D Wigner crystal [117] and a 1D Wigner molecule [118], the observation of Klein tunnelling [119] and the observation of valley-spin blockade [120] and the realization of a valley-spin qubit [121], to name only the most prominent ones – were driven by the continuously improving quality of devices. These tremendous improvements of the device quality were obtained by applying so-called ultraclean processing schemes. In these schemes the CNT is grown either in the last production step [122] or transferred as-grown by means of stamping techniques [120, 123]. Both approaches avoid contamination and damage of the CNT that results from chemical processing and the location of individual CNTs by AFM or SEM. Unfortunately, it turns out to be extremely challenging to incorporate superconductors into these processing schemes [124]. Indeed the yield of "good" superconducting contacts is typically significantly lower than the yield of "good" normal conducting contacts, also for conventional processing schemes. In the beginning of this PhD project we faced a very low yield of devices that showed signatures of superconductivity. Urged by this low yield – and inspired by the stunning characteristics of ultraclean devices – we experimented with novel fabrication approaches. These approaches aim to improve the contact quality or the device quality or even both at the same time.

### 5.1. Aluminium oxide protection layer against resist contamination

As outlined in section 4.2 lithography resist usually leaves residues which can not be removed from CNTs with conventional methods: cleaning by oxygen plasma or UV ozone both attack the CNT and eventually remove it. In the following we introduce an approach which avoids a direct contact between the lithography resist and the nanotube and thereby prevents a contamination with polymer residues. To achieve this we cover the CNTs with an aluminium oxide ( $\text{Al}_2\text{O}_3$ ) protection layer directly after CVD growth. The  $\text{Al}_2\text{O}_3$  is grown by atomic layer deposition (ALD) as described in reference [125]. The CNT surface is chemically inert to the precursor molecules of the ALD process [126] and we use a substrate-assisted growth to encapsulates the CNTs.<sup>1</sup> The oxide was grown in 40 ALD cycles, yielding a 4.4 nm thick layer under which the CNTs could still be located with the SEM. The devices went through the standard lithography processes, but the  $\text{Al}_2\text{O}_3$  was locally etched away after the resist was developed. The etching was done in a 25% tetramethylammonium hydroxide (TMAH) water solution during 20 sec at 50°C and stopped in a water bath. A good adhesion between the resist and the  $\text{Al}_2\text{O}_3$  layer is required to avoid an under-etching of the resist mask, which is driven by capillary forces between the hydrophobic resist and the water diluted TMAH. We found that PMMA(950K) masks work well, while PMMA-MA masks get under-etched.

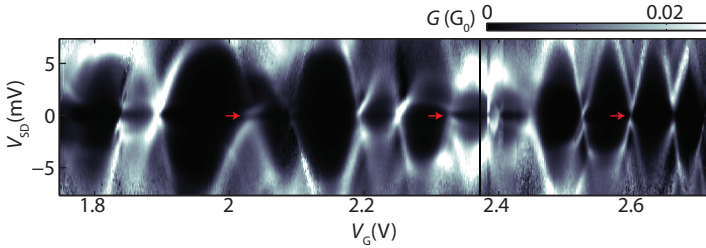


**Figure 5.1.:** Stability diagram of a N-QD-S device ( $N = 50$  nm Pd;  $S = 4$  nm/50 nm Pd/Al) measured at 230 mK. The red arrows guide the eye to the superconducting transport gap of  $2\Delta \approx 0.24$  meV. The device was fabricated with an  $\text{Al}_2\text{O}_3$  protection layer against resist contamination and corresponds to QD2 of the CPS device in Chapter 6.

After dissolving the protection layer we presumably recover a clean CNT surface, free of polymer residues. We fabricated several batches to test if

<sup>1</sup>Some groups functionalize the CNT surface by an iterative exposure to  $\text{NO}_2$  and trimethylaluminum (TMA) to grow  $\text{Al}_2\text{O}_3$  directly on the CNT [126, 127].

the protection layer fully covers the CNTs in the first place and dissolves sufficiently within the given etch time. If the  $\text{Al}_2\text{O}_3$  layer was etched for only 1 sec no electrical contact to the CNTs could be established, indicating a full CNT coverage. In batches with etch times  $t \geq 10$  sec about one-third of the devices had good contact properties with a room temperature two-terminal resistance below 200 k $\Omega$ . For typical processing we chose an etching time of 20 sec, well above the clearing time of  $\sim 10$  sec. The uncontacted segments of the CNT remained covered with  $\text{Al}_2\text{O}_3$  after the sample fabrication was completed. Due to the poor wetting properties of  $\text{Al}_2\text{O}_3$  on the CNT surface we presume that the  $\pi$ -electron system is not disturbed severely. Figure 5.1 shows the stability diagram of a CNT QD fabricated in this manner. The stability diagram demonstrates the formation of a stable QD, but the height of the diamonds and the width of the resonances exhibit irregular variations on a scale that is typical for conventionally fabricated CNT QDs. Figure 5.1 may also serve as a reference for the clean and ultraclean QD characteristics discussed in Section 5.2 and 5.3.

### 5.1.1. Conclusions

In the conduct of this PhD project the application of the described protection layer technique marked a breakthrough. We unsuccessfully fabricated 16 batches of CNT based Cooper pair splitter devices, without ever observing an induced superconducting gap. The first batch fabricated with a  $\text{Al}_2\text{O}_3$  interlayer yielded the sample presented in chapter 6 (Near-unity Cooper pair splitting efficiency). However, one should be cautious when drawing conclusions from this fact. It does not necessarily mean that the protection layer technique is notably good, it could also be a hint that we did a particular bad job in the fabrication of the first 16 batches.<sup>2</sup> Indeed other groups successfully fabricated devices with narrow superconducting strips on CNTs with standard EBL techniques [56, 64]. Thus, one may achieve comparable good devices by optimizing the EBL process as described in section 4.2.

In conclusion we successfully applied a fabrication scheme that protects CNTs from contamination by lithography resist. The technique relies on an  $\text{Al}_2\text{O}_3$  interlayer and is probably most effective when the EBL processing is

---

<sup>2</sup>In retrospect I believe that the main problem during the fabrication of the first 16 batches was a too low exposure dose for the EBL of the narrow superconducting strip. As outlined in section 4.2 this presumably increases the amount of residues. However, instead of increasing the dose I first increased the development time. Dose tests were interpreted to find the dose that gives the best match with the designed structure (later I tried to determine the highest dose that is tolerable). The increased development time caused therefore even smaller exposure doses, which increased the amount of residues further.

not thoroughly optimized, leaving problematic amounts of residues on the contact area after development. However, we fabricated too few batches to make definite statements about the yield and the device quality. We can therefore not judge if the benefits of the method prevail the drawbacks, such as the unknown variables that one introduces – will there be harmful trap states in the  $\text{Al}_2\text{O}_3$  layer? does the etching procedure degrade the properties of the CNT properties? – and the additional processing time.

## 5.2. Cleaning and selective CNT etching with hydrogen radicals

Instead of trying to avoid a resist contamination of the CNT one may also develop new cleaning methods. The finesse is to find a method that is aggressive enough to remove organic residues without attacking the nanotube's carbon atoms. Hydrogen radicals are a potential candidate to manage this balancing act: they don't break the C–C bonds of an intact graphene lattice but attack carbon atoms which are not fully embedded into such a robust lattice [128–131]. However, already a single defect site in the graphene lattice can be sufficient to trigger a chain reactive etching process [128–131]. Below we will show that hydrogen radicals not only remove PMMA, they can also be used to selectively etch CNTs. It is not clear which factors eventually determine if a CNT is inert against H radical etching. Despite this uncertainty we suggest a etching mechanism that discriminates between CNTs that are free of dangling bonds and others which are not. The potential application of H radicals is therefore twofold: 1) They can remove undesired residues from structured PMMA masks without attacking the CNT. 2) They may be used to preselect low-defect CNTs. We present several devices that are fabricated from H radical inert CNTs and characterized at low temperatures by transport measurements to support the hypothesis of a low-defect CNT selection.

### 5.2.1. Generation of hydrogen radicals from a hydrogen plasma

Hydrogen radicals can be generated as a by-product of a hydrogen plasma which we create in the vacuum CVD reactor shown in Fig. 5.2. The quartz tube of the CVD reactor is equipped with a cylindrical capacitor connected to a radiofrequency (RF) generator. We apply an RF power of 25 W at 13.56 MHz to the electrode, while letting  $\text{H}_2$  flow through the quartz tube at rate of 20 sccm and a pressure of 1.2 mbar. These conditions allow to ignite and maintain a  $\text{H}_2$ -plasma. The characteristic plasma glow, caused by the recombination of ions and electrons, gives a good estimate of the

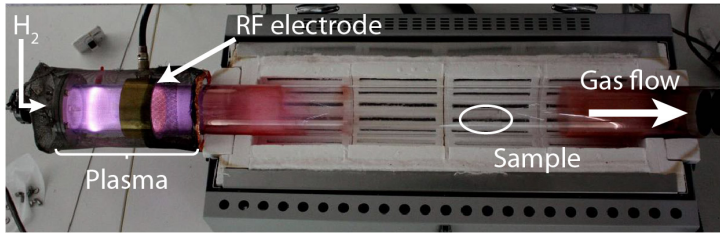


**Figure 5.2.:** Set-up for hydrogen radical etching. A vacuum CVD reactor is equipped with a cylindrical capacitor connected to an RF generator to ignite a hydrogen plasma. The sample is placed downstream in the quartz tube at a position where the aggressive hydrogen ions already recombined but the  $H_2$  gas is still enriched with less aggressive hydrogen radicals. The set-up allows to control  $H_2$  flow, pressure, temperature and RF power. The distance between sample and RF electrode is 52 cm.

longitudinal extension of the plasma. The sample is placed downstream of the RF electrode at a position where the high energetic hydrogen ions already recombined, but the  $H_2$  gas is still enriched with the less aggressive hydrogen radicals. By varying the distance between the plasma and the sample allows to tune the ratio of hydrogen ions, radicals and molecules, as a result of the different recombination rates of ions and radicals [130]. To hinder that the CNTs are damaged by ion bombardment the samples were placed at a distance 52 cm downstream from the RF electrode. Further details on the set-up and the etching mechanisms, as well as further specifications of etch rates, can be found in the PhD thesis of Dorothée Hug [130] who equipped the CVD set-up with the RF electrode and performed many etching experiments with graphene and graphite.

### 5.2.2. Selective etching of carbon nanotubes

Figure 5.3 shows a SEM image of CNTs, grown by CVD on a  $SiO_2$  substrate with a Ti/Au marker grid that was patterned after growth. The wafer was exposed to hydrogen radicals for 60 min at  $T = 350^\circ C$  under the above stated conditions. After this treatment the wafer was again imaged. The comparison of SEM images in Fig. 5.3 shows that a large fraction of CNTs got etched away. However, some CNTs were inert to the treatment. A third class of CNTs was partially etched or fragmented into shorter segments (see upper right image in Fig. 5.3).

In the following we propose an etching mechanism that discriminates between CNTs that are free of dangling bonds and others which are not. However, the proposed etching mechanism should be treated as hypothesis for which we have no direct experimental evidence. This hypothesis is

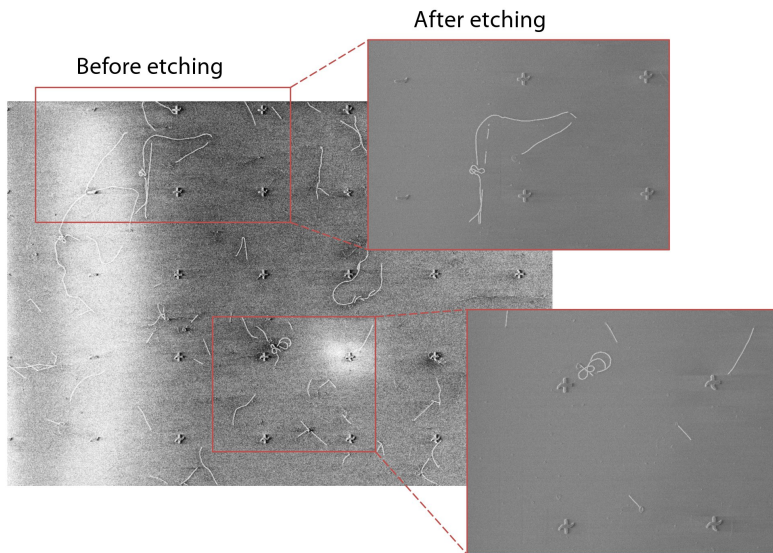


**Figure 5.3.:** SEM images of CVD grown CNTs on  $\text{SiO}_2$  before and after a 60 min hydrogen radical treatment at  $350^\circ\text{C}$ . A large fraction of CNTs is etched away, whereas some CNTs are inert to the treatment. The spacing between the markers is  $10\ \mu\text{m}$ . For a better visibility the contrast of the CNTs was enhanced with a image editing software.

derived from state of the art experiments in which graphene is exposed to H radicals under similar conditions [128–130]. These experiments consistently show that for certain parameter regimes graphene is merely etched at defect sites and at the edges, but not in the basal plane. More strikingly, the etching is anisotropic and produces regular hexagonal pits around an initial defect site. The current understanding of this process can be summarized as follows. H radicals can not break the C–C bonds in a graphene lattice, unless an additional activation energy of about  $1.2\ \text{eV}$  is provided [131]. At the graphene edge and at strong defect sites the carbon atoms have an unsaturated bond. Two H radicals can bind to these atoms without breaking a strong C–C bond: one H radical binds to the dangling bond, the other H radical breaks the weak  $\pi$ -bond. The electronic configuration of the bi-hydrated carbon is no longer  $sp^2$ . The two remaining C–C bonds are weakened and can now be broken up by the H radicals. The C atom with the initial dangling bond is removed from the lattice under the creation of a  $\text{CH}_4$  molecule. Each carbon atom that is removed from the lattice leaves

two new C atoms with a dangling bond: a chain-reaction sets in. For a CNT this chain-reaction can be viewed as a process that is inverse to CVD growth. Atom by atom is removed from the CNT lattice and methane is created as end product. Within this analogy the dangling bonds play the role of the CVD catalyst, they initiate the reaction. The fact that some CNTs become fragmented into several long segments is not compatible with an etching mechanism that attacks the CNT uniformly. It may thus be seen as an indication for the non-uniform "inverse growth" mechanism.

### 5.2.3. Etching of PMMA

To determine the etch rates of PMMA we spin-coated wafers with 200 nm thick films that were baked for 2 min on a hot plate at 180°C. The wafers were exposed to H radicals at the same conditions as above ( $p = 0.4$  mbar,  $P_{\text{RF}} = 25$  W,  $\text{H}_2$  flow rate: 20 sccm, sample-electrode distance: 52 cm) and etched for 10 min at different temperatures. As a control test we also exposed the samples to the same conditions without plasma ( $P_{\text{RF}} = 0$ ). It turns out that the PMMA etch rate is strongly temperature dependent. At room temperature no significant etching was obtained. At  $T = 110^\circ\text{C}$  a convenient PMMA etch rate of 7 nm/min was observed. The etch rate was the independent of the molecular weight (we tested 50K and 950K) and without igniting the plasma no etching took place. At 350°C the PMMA was fully removed during 10 min, even without application of an RF power. We found that a temperature of 110°C is still compatible with structured and developed PMMA masks (at too high temperatures the masks start to melt). However, the etching degrades the lift-off properties and a good undercut of the PMMA mask is required.

### 5.2.4. Transport measurements on hydrogen radical inert CNTs

In Fig. 5.4 and 5.5 we present low temperature transport measurements on CNT devices that were fabricated by modifying the standard scheme, described in Section 4.1, in the following ways:

1. After CVD growth we performed H radical etching for 30-60 min at 350°C to preselect inert CNTs.
2. Before depositing the metal contacts we cleaned the contact areas by a 1 min exposure to H radicals at 110°C, which removes about 7 nm PMMA.
3. After lift-off the samples were annealed for 60 min in vacuum at 350°C to exclude possible hydrogenation effects (dehydrogenation of CNTs sets in at 200°C [132]).

	Contacts	Etch time	Resist
Sample A	Ti/Nb & Ti/Au	30 min	bilayer
Sample B	Ti/Nb & Ti/Au	30 min	bilayer
Sample C	Ti/Nb	60 min	single layer
Sample D	Pd/Nb	60 min	single layer

**Table 5.1.:** Summary of fabrication details. The thickness of the adhesion layers below the Nb contacts was 3-4 nm. The etch time refers to step 1 of the protocol (CNT preselection). As single layer resist we used 300 nm of PMMA(950K), bilayers were made from PMMA(50K)/PMMA(950K) (200 nm/100 nm).

We fabricated four test batches, labelled  $\mathcal{A}$ ,  $\mathcal{B}$ ,  $\mathcal{C}$  and  $\mathcal{D}$ , and contacted between four and eight CNTs per batch. Below we present measurements from one selected CNT, named A, B, C and D, out of each test batch. The study was not fully systematic. The differences between the devices are summarized in Table 5.1.

Starting with the stability diagram of sample A [Fig. 5.4(a)] we note that a clear fourfold symmetric shell-filling pattern can be observed over a wide range of gate voltages. The gate voltage allows to tune the QD from a closed into an open regime. At the right side of Fig. 5.4(a) the individual Coulomb peaks can no longer be resolved and a Fabry-Perot like beating pattern is observed. However, the rather low conductance of only  $5 \cdot 10^{-2} G_0$  seems unexpected in combination with Fabry-Perot oscillations, which are usually observed for very transparent contacts with tunnel resistances  $R < h/e^2$ . In a capacitor model of the QD this condition allows electrons to enter and leave the QD on a time-scale  $\tau \sim RC$ , that is short enough to overcome the charging energy,  $U = e^2/C$ , according to Heisenberg's uncertainty principle,  $h/\tau > U$ . For sample A we conclude that only one of the two contacts fulfils the condition  $R < h/e^2$ , while the second contact is weakly coupled and acts as tunnel probe. In this interpretation the Farby-Perot interferometer consists of a semi-transparent mirror (strongly coupled contact) and a second mirror that is almost fully reflecting (tunnel probe).

Test sample B exhibits similar transport characteristics as sample A, including fourfold symmetry and gate dependence of the contact resistance [Fig. 5.4(b)]. However, the Fabry-Perot regime is not entered, even though the conductance is about one order of magnitude higher than for sample A.

Within the range  $-30\text{V} < V_{\text{BG}} < 30\text{V}$  neither sample A nor sample B could be gated into a band gap. Test sample C was selected to show that the hydrogen radical etching does not discriminate between metallic and semiconducting CNTs. The back gate sweep in Fig. 5.5(a) displays a semiconducting CNT with a band gap of 0.87 eV. Conduction though the electron band and the hole band are on the same order of magnitude,

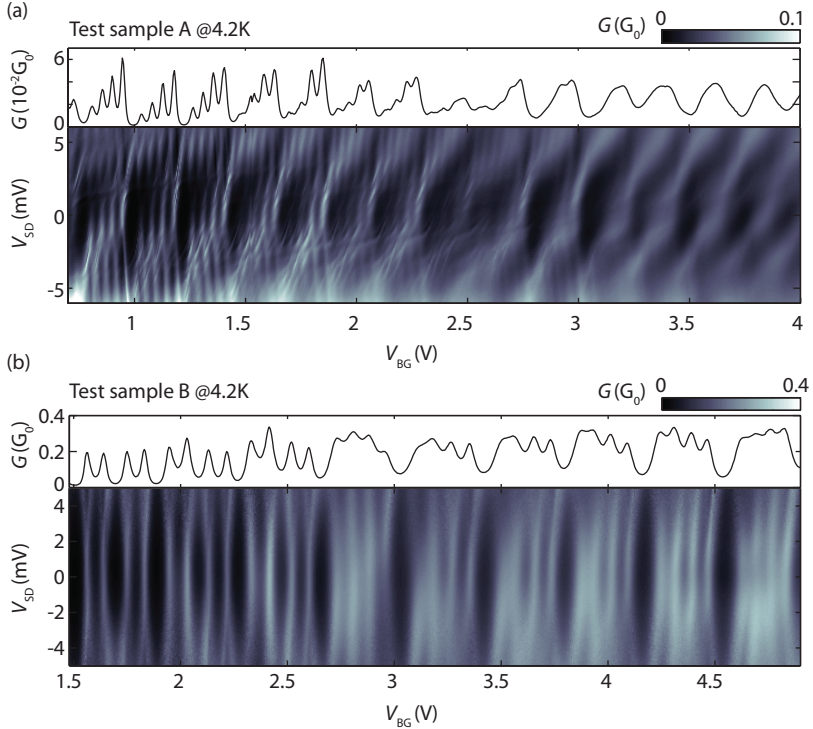


**Figure 5.4.:** (a,b) Stability diagrams of hydrogen radical inert CNTs from two different fabrication batches. The measurements were performed in a He dewar at 4.2 K. The top panels show a cut of the differential conductance,  $G$ , across zero bias,  $V_{SD} = 0$ . Both samples show clear fourfold symmetry and are backgate tunable from a closed to an open QD regime. For (a) the low conductance values suggest a strongly asymmetric coupling,  $\Gamma_1 \ll \Gamma_2$ .

suggesting that the work function of the contact lies in deep inside the band gap. The center of the band gap is shifted to  $V_{\text{BG}} = -18\text{ V}$  due to doping. It remains unclear if this doping is caused by the hydrogen treatment. Figure 5.5(c) shows a zoom into the backgate region where the first electrons are filled into the CNT. By eye it is hard to see a shell-filling pattern, but the addition energy spectrum of the QD demonstrates a twofold degeneracy. Such a reduced symmetry indicates disorder which strongly scatters the electrons between the K and K' valley (alternatively it is also conceivable that the spin-degeneracy is broken and the valley degeneracy is conserved).

Test sample D is a three-terminal device with two well-decoupled QDs. An SEM image of sample D is shown as inset of Fig. 5.5(b). The curly structures are metal residues due to an insufficient undercut. Such lift-off problems were not present for samples A and B, which have been fabricated with a resist bilayer (see Table 5.1). In Fig. 5.5(b) both QDs show a weak fourfold symmetry. This underpins the view that the shell-filling symmetries are determined by the CNT and not by the contacts.

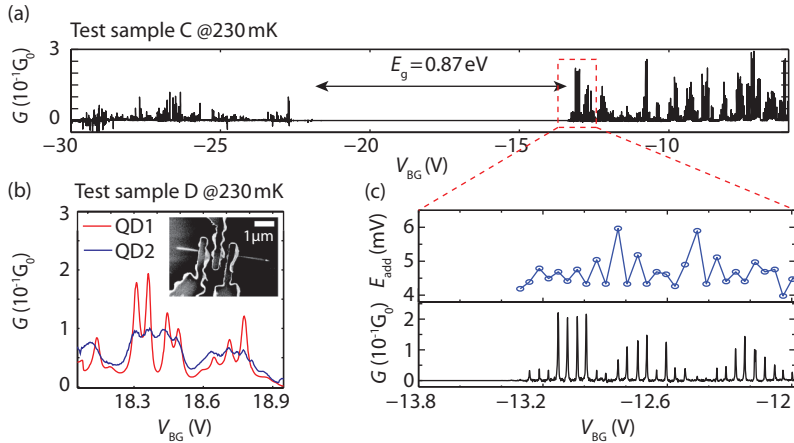


**Figure 5.5.:** Differential conductance around zero bias as a function of backgate voltage for two hydrogen radical inert CNTs. Measurements were performed in a  $\text{He}^3$  cryostat at 230 mK. (a) A semiconducting CNT with a band gap of 0.87 eV. The center of the band gap is strongly shifted away from  $V_{\text{BG}} = 0$ , indicating the presence of chemical doping. (b) Measurements on the two QDs from the three-terminal shown in the inset. (c) Zoom into the backgate region where the first electrons are filled into test sample C. The extracted addition energies (top panel) show a only twofold symmetric shell-filling.

### 5.2.5. Conclusions

In this section we demonstrated that clean and stable CNTs behaviour can be observed on devices where the CNTs were cleaned and pre-selected by a hydrogen radical treatment. The low-defect rate of the CNTs is concluded rather indirectly from shell-filling patterns which frequently showed fourfold symmetry. Devices of similar quality were frequently obtained with standard fabrication techniques, see e.g. Refs. [50, 133, 134]. However, this actually fits to the viewpoint that the shell-filling properties of CNT QDs are mostly governed by the tube quality: when many CNTs are contacted it is only a matter of time until a high quality CNT is found. The transport properties of the presented test samples suggest that the chances to find clean CNTs can be improved by pre-selecting the CNTs via an exposure to hydrogen radicals. However, a more systematic study with better statistics would be desirable to support this claim.

Unlike shell-filling symmetries, the superconductivity related properties of a CNT QD seem to be determined by the contact and not by the CNT. Without stating it explicitly we showed devices that were connected to at least one superconducting contact. Test samples A and B had a S-QD-N geometry and test samples C and D had a S-QD-S geometry, where S refers to a sputtered Nb contact with a Ti or Pd adhesion layer (3-4 nm). Anyway, none of the presented stability diagrams showed signatures of superconductivity. In general the yield of working QD devices was much higher than the yield of QDs that showed signatures of superconductivity. About 50% of the fabricated QDs had room temperature resistances  $R_{RT} < 100 \text{ k}\Omega$ , but from 18 fabricated QDs only 3 showed superconductivity related behaviour. In Section 6.7 and Chapter 7 we present results that were obtained from these QDs. The reason for the lower yield of superconducting QDs remains unclear. Following the theoretical study of Takei *et al.* [135] one may speculate that not only the coupling between S and the QD plays an important role, but also the homogeneity of the coupling, i.e. the variation of a locally defined  $\Gamma_S(x)$ , where  $x$  describes the position along the metal-CNT interface.

Lastly we assess that the cleaning of PMMA residues from the contact area by hydrogen radical etching did not lead to the desired reproducibility of the contact properties. Many devices exhibit asymmetric couplings,  $\mathcal{O}(\Gamma_1) \neq \mathcal{O}(\Gamma_2)$ , and the yield of QDs with superconducting contacts was considerably lower than the yield of QDs with transparent contacts. However, the clean CNT behaviour, the good yield of transparent contacts and the small but acceptable yield of QDs with niobium induced superconductivity are good arguments for the additional processing time. In addition, the method can be applied for a controlled reduction of the CNT density

after CVD growth (a too high CNT density often hinders further processing of a batch, which is especially annoying if the wafer already contained nanostructures, e.g. bottom gates).

### 5.3. Bottom-gate defined quantum dots

We discussed in the introduction to this chapter how improvements of the device quality have pushed CNT experiments into realms that many researchers would have conceived as unreachable before. The dramatic improvements of the device quality have been a result of so-called ultraclean processing schemes. In these schemes the CNT is placed in the last step of the fabrication [120, 122, 123]. The pristine and stable behaviour of these devices was naturally attributed to the absence of any kind of chemical processing and the fact that the CNTs were suspended from the SiO<sub>2</sub> substrate [122]. However, Minkyung Jung *et al.* surprisingly found that the characteristics of ultraclean CNTs can also be obtained, even when a conventional resist-based lithography step is used after placing the CNT [34]. In the following the findings of Jung *et al.* are briefly summarized. The author of this thesis made minor contributions to the sample fabrication. The main work was carried out by Minkyung Jung.

#### 5.3.1. Sample fabrication

The samples were fabricated as described in Section 4.1, but pairs of bottom gates were embedded into the SiO<sub>2</sub> substrate before CVD growth. These gates could be used to define the QDs electrostatically, as opposed to contact-defined QDs. Figure 5.6 illustrates the device fabrication. The trenches for the bottom gates were fabricated by EBL and a reactive ion etching with CF<sub>4</sub>, followed by a wet etch step with buffered HF to create an undercut. The trenches are metallized with sputtered Re, but any metal that is compatible with the conditions during CVD growth may be chosen. SEM imaging is used to find CNTs that grew over the pre-defined bottom gates and a standard EBL step is used to place source-drain contacts of Ti/Au (5 nm/65 nm).

#### 5.3.2. Transport characteristics

The devices were measured in a <sup>4</sup>He transport dewar at 4.2 K. The investigated CNTs exhibited band gaps of  $\sim 100 - 300$  meV. The back gate voltage was set to  $V_{BG} = -7.5$  V. In this regime the complete CNT was p-doped and the device acted as a Fabry-Perot cavity (Fig. 5.7). The cavity length

can be extracted from the energy dependence of the Fabry-Perot oscillations according to  $L = \pi v_F \hbar / e V_C$  [136], where  $v_F = 8.1 \cdot 10^{-5}$  m/s [25] is the Fermi velocity and  $V_C = 3$  V is the characteristic bias voltage marked in Fig. 5.7(b). This yields an effective length of 700 nm, which is well in agreement with the separation between the source and drain contact measured by SEM. To define a QD a positive voltage is applied to one of the bottom gates. This pulls the conduction band below the Fermi energy, as illustrated in the top row of Fig. 5.8, until a p\*-n-p\* junction is formed. Here p\* denotes the doping of CNT segment adjacent to the source-drain contacts. The tunnel barrier between p\* and n region is given by the CNT band gap and the electric field configuration. In this way it is possible to define extremely small QDs with smooth confinement potentials. The stability diagram shown in Fig. 5.8 exhibits a charging energy of  $U \gtrsim 50$  meV. The estimated size of the QD is 80 nm (see [34]), which is comparable to the bottom gate width of 70 nm. A QD of similar quality could be formed over each of the two bottom gates. In addition it was possible to form double QDs (p\*-n-i-n-p\*) and even bipolar triple QDs (p\*-n-p-n-p\*).

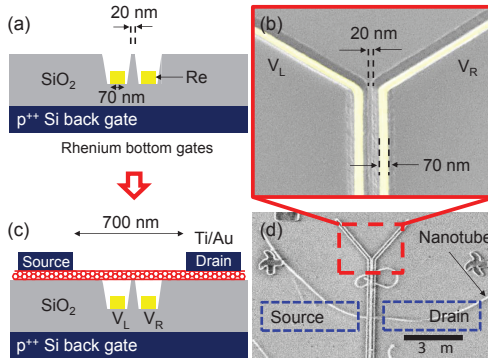


**Figure 5.6.:** (a) Schematics of the recessed Re bottom gates that were sputtered in trenches in the  $\text{SiO}_2$  substrate. (b) SEM image of the bottom gate contact area in (d) taken at  $80^\circ$  tilting angle. (c) Schematics of the CNT device with source and drain contacts. The CNT growth is not the last step but is followed by a conventional resist-based electron beam lithography step to define the source and drain contacts made of Ti/Au bilayer. (d) SEM image after the carbon CNT growth. Reproduced with permission from [34]. Copyright 2013 American Chemical Society.

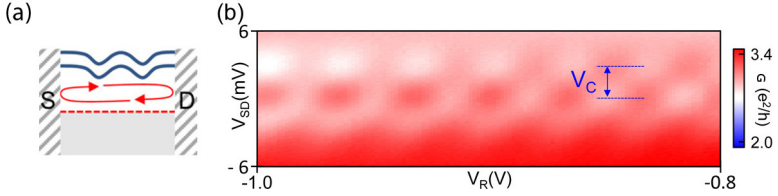


**Figure 5.7.:** (a) Energy band diagram of the CNT in the Fabry-Perot regime. (b) Differential conductance,  $G$ , as a function of the voltage applied to the right bottom gate,  $V_R$ , and source-drain bias,  $V_{SD}$ . Reproduced with permission from [34]. Copyright 2013 American Chemical Society.

### 5.3.3. Conclusions

The work of Jung *et al.* shows that ultraclean CNT-QD characteristics can be obtained after a resist-based microfabrication process is used. To appreciate the device quality one may compare Fig. 5.8 with the conductance map of a conventional QD exemplified in Fig. 5.1 and the conductance maps of the clean devices shown in Fig. 5.4. The characteristic energy scales of the bottom gate defined QD,  $U$  and  $\delta E$ , are a factor of  $\sim 10$  larger than that of typical contact defined QDs. This is mainly a consequence of the small dot length (for the charging energy also the suspension from the dielectric substrate contributes). Jung *et al.* suggest that this large energy scales leave the devices immune to the remaining disorder potentials caused by resist residues and adsorbates. It is interesting to note that the change to ultraclean processing schemes led almost naturally to the inclusion of bottom gates to control the devices and the devices e.g. in Refs. [27, 119] also exhibit very large charging energies  $U \sim 40$  meV.

The bottom gate definition of CNT QDs greatly increases the versatility of the device fabrication and offers the prospect to realize ultraclean QD-S hybrid devices. This calls for the fabrication of an ultraclean CNT based Cooper pair splitter. Eventually more advanced gating schemes may even allow individually tune the tunnel coupling of the QDs.

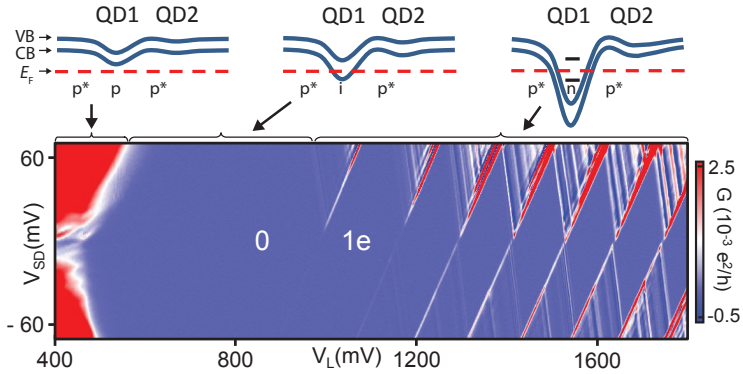


**Figure 5.8.:** Stability diagram,  $G(V_{SD}, V_L)$  of a single QD defined over the left bottom gate. A clean QD behavior is observed in the few electron regime displaying sequential electron filling starting from the empty QD (0) with the first electron (1e). The top row schematically shows the evolution of the energy band diagrams of the CNT as a function of  $V_L$ . It was also possible to define QDs of similar quality over the right bottom gate and double or even triple (n-p-n) QDs. Reproduced with permission from [34]. Copyright 2013 American Chemical Society.



## Near-unity Cooper pair splitting efficiency

### 6.1. Introduction

In this chapter we present experimental results from CNT based Cooper pair splitter device. By charge transport measurements we demonstrate that up to 90% of the incoming current is converted into subsequently split Cooper pairs. Efficiencies close to unity mark an important step on the way to applications and more sophisticated experiments, for example the explicit demonstration of entanglement. The obtained efficiencies, which by far exceed 50%, can also be regarded as a proof that the splitting is enforced by electron-electron interactions. Splitting efficiencies up to 50% can in principle be reached without enforcing the splitting, e.g. in a chaotic cavity [90], or in a double-dot system with strong inter-dot coupling [64], where the electrons of a Cooper pair can exit the device through two ports at random.

In the regime of high efficiencies also new questions arise: we find an apparent mismatch between the CPS currents extracted in the left and in the right arm of the device. We develop a master equation "toy model" to explain how these discrepancies arise from a competition between local processes and CPS. We also present first attempts to further improve such devices by using superconducting materials with energy gaps on the meV scale. Parts of this chapter were published elsewhere in similar form [66].

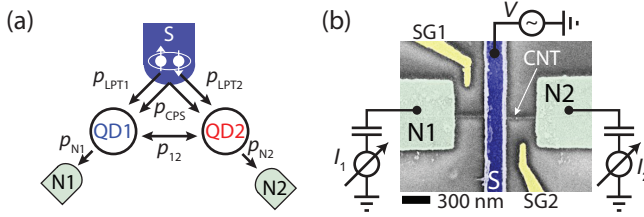


**Figure 6.1.:** (a) Schematic of the device geometry. The probabilities for the individual transport processes,  $p_i$ , are discussed in the text. (b) Scanning electron micrograph of the CPS device and measurement set-up.

## 6.2. Device and measurement set-up

An artificially coloured scanning electron micrograph of a CPS device is shown in Fig. 6.1(b), together with a schematic of the measurement set-up. The device was fabricated as described in Sec. 5.1. A CVD grown CNT (arrow) is contacted in the center by a 200 nm wide Pd/Al (4 nm / 60 nm) contact (S), which becomes superconducting below  $\sim 1.1$  K. Two pure Pd contacts to the right and left of S serve as normal metal contacts N1 and N2, both of which define a quantum dot (QD1 and QD2) on the two CNT segments adjacent to S. The QDs can be tuned electrically by a global backgate and the local side-gates SG1 and SG2.

The experiments are performed in a dilution refrigerator at a base temperature of  $\sim 20$  mK. From standard charge stability diagrams we extract charging energies of  $\sim 7$  meV for QD1 and  $\sim 4$  meV for QD2 and an orbital energy spacing of  $\sim 1$  meV. At zero magnetic field we find that a BCS-like density of states is impinging on the co-tunnelling background of each QD. Figure 6.2(a) shows the non-linear differential conductance of QD1 and QD2, measured off resonance in the co-tunnelling regime for different strengths of an external magnetic field. The magnetic field was aligned parallel to the chip plane. From Fig. 6.2(a) we extract the magnitude of the induced energy gap as  $\sim 120$   $\mu$ eV and a critical magnetic field of  $\sim 150$  mT. With S in the normal state we find typical level broadenings of  $\sim 150$ -500  $\mu$ eV. Many Coulomb peaks exhibit relatively low peak conductances which suggests rather asymmetric couplings of the QDs to the leads. The lever arms from a side-gate across the superconductor to the other QD is roughly ten times smaller than that of a local side-gate. Figure 6.2(b) shows a conductance measurement in the normal state, with both QDs in series and the S contact floating. We find that the conductance is maximal when both QDs are resonant and we do *not* observe any avoided crossings of the QD

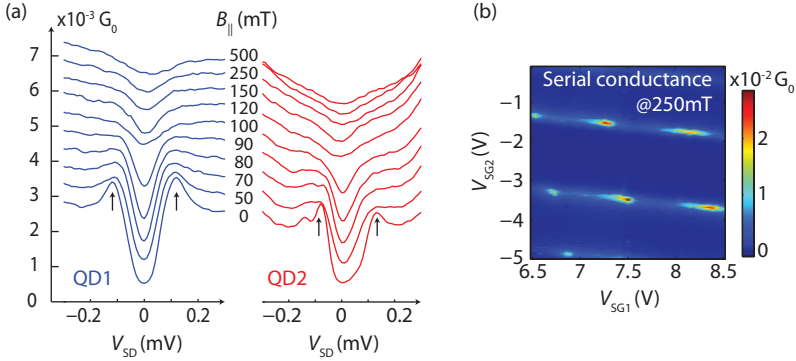


**Figure 6.2.:** (a) Differential conductance  $G_1$  (left) and  $G_2$  (right) of QD1 and QD2 as a function of the source-drain voltage  $V_{SD}$  for different magnetic fields  $B_{||}$ . The arrows indicate the position of the quasiparticle peaks in the BCS density of states. For clarity the curves are offset by  $5 \cdot 10^{-4} G_0$ . (b) Serial conductance of QD1 and QD2 measured from N1 to N2 with floating S contact while varying  $V_{SG1}$  and  $V_{SG2}$ .

resonances. This demonstrates that the two QDs are well decoupled and can be tuned individually without a hybridization of the QD levels. This difference to Ref. [64] might be due to the larger width of S.

### 6.3. Experimental signature of Cooper pair splitting

Figures 6.3(a) and 6.3(b) show the simultaneously recorded differential conductances  $G_1$  through QD1 and  $G_2$  through QD2, both as a function of the side-gate voltages  $V_{SG1}$  and  $V_{SG2}$ . The measurements were done at zero bias and zero magnetic field. When  $V_{SG1}$  is varied, QD1 is tuned through several resonances, which result in conductance maxima in  $G_1$ , labelled L1, L2 and L3 in Fig. 6.3(a). The amplitudes of the resonances vary only little when tuning  $V_{SG2}$ , while the resonance position changes slightly due to capacitive cross talk from SG2 to QD1. Very weak, but similar conductance ridges labelled R1, R2 and R3 can be observed in the conductance through QD2 in Fig. 6.3(b). These are mainly tuned by SG2, which results in conductance ridges almost perpendicular to the ones in Fig. 6.3(a) due to QD1.<sup>1</sup>

Our main experimental findings are pronounced peaks when both QDs are in resonance. At these gate configurations the conductance is increased

<sup>1</sup>The two weak lines between R1/R2 and R2/R3 at two constant  $V_{SG1}$  values are probably due to random charge rearrangements.

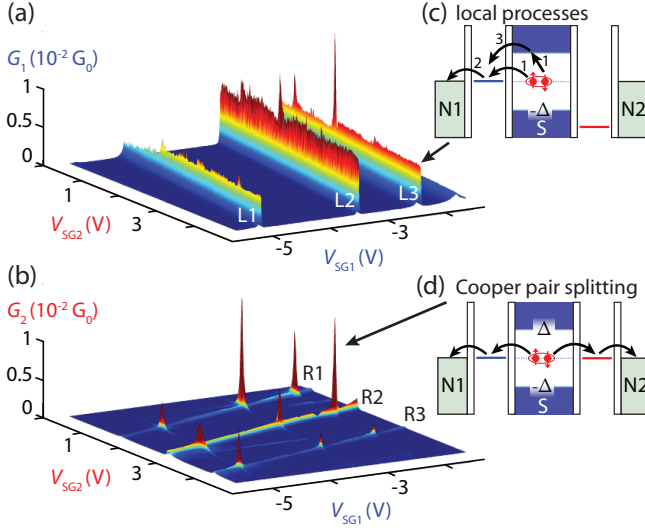


**Figure 6.3.:** (a) Differential conductance  $G_1$  of QD1 and (b)  $G_2$  of QD2 as a function of the side-gate voltages  $V_{SG1}$  and  $V_{SG2}$ . (c) and (d) Energy diagrams of local (Cooper) pair tunneling (LPT) and CPS.

by up to a factor of  $\sim 100$  compared to the respective conductance ridge. This is most prominent in  $G_2$ , but most of the peaks are also visible in  $G_1$  on a larger background. No peaks at resonance crossings can be observed when the superconductivity is suppressed by a small external magnetic field (see inset of Fig. 6.4(a) and discussion below). If only one QD is resonant, only local transport through this QD is allowed. A possible local process is local (Cooper) pair tunneling (LPT), illustrated in Fig. 6.3(c): the first electron of a Cooper pair is emitted into the QD, which leaves S in a virtual excited state. When the first electron has left the dot, the second tunnels into the same QD. Other local processes like double charging of a dot are strongly suppressed by the large charging energies. However, if both QDs are in resonance, the second electron can tunnel into QD2, as shown in Fig. 6.3(d), which splits the initial Cooper pair.

We now focus on the resonance crossing (L2,R2). Figure 6.4(a) shows the Coulomb blockade resonance L2 in  $G_1$  as a function of  $V_{SG1}$  (blue curve). In the same gate sweep  $G_2$  is tuned through the resonance R2 due to capacitive cross-talk which results in a wide conductance maximum (red curve). However, an additional much sharper peak occurs at the voltage of the L2

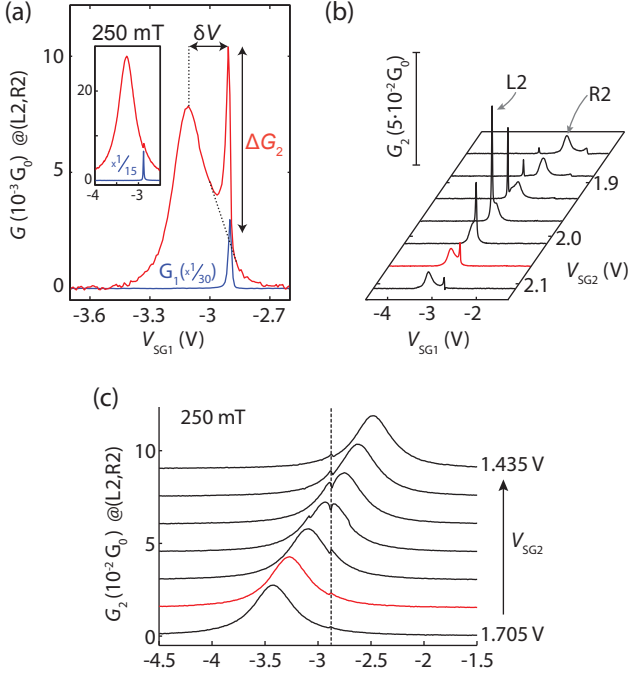


**Figure 6.4.:** (a)  $G_1$  and  $G_2$  as a function of  $V_{SG1}$  for  $V_{SG2} \approx 2.07$  V. Inset: the same measurement at a magnetic field of 250 mT to suppress the superconductivity. (b)  $G_2(V_{SG1})$  for a series of side-gate voltages  $V_{SG2}$ . The curve from (a) is highlighted red. (c)  $G_2(V_{SG1})$  for a series of side-gate voltages  $V_{SG2}$  in the normal state ( $B_{\parallel} = 250$  mT).

resonance, with similar width and shape as the resonance in  $G_1$ . This narrow peak corresponds to the additional conductance due to CPS. Figure 6.4(b) shows the evolution of this CPS conductance in  $G_2$  for a series of different side-gate voltages  $V_{SG2}$  with the curve from Fig. 6.4(a) highlighted in red. Note that the position of the CPS peak in  $G_2$  has almost no dependence on  $V_{SG2}$ . It remains pinned to the position of the  $G_1$  resonance, as expected for a correlated two-particle effect like CPS.

As a control experiment we suppress the superconductivity in the S-contact by a magnetic field of 250 mT and perform the same side-gate voltage scans as in Fig. 6.3(a,b). The results are plotted in Fig. 6.5(a,b). In the superconducting state the local current was strongly suppressed by the combination of Coulomb interactions and superconducting pairing. In

the normal state there are no paired electrons in the S-contact and this suppression is not present. The overall conductance is strongly increased. More importantly, on the scale of Fig. 6.5(a,b) no conductance correlations between  $G_1$  and  $G_2$  are observed. In Fig. 6.4(c) we plot slices across the conductance map of Fig. 6.5(b) for a series of  $V_{SG2}$  values, in analogy to Fig. 6.4(b). Fig. 6.4(c) reveals that conductance correlations are still present in the normal state. However, these correlations are considerably smaller than in the superconducting state. At the SG1 voltage of the QD1 resonance (dashed vertical line) we observe either tiny dips (close to resonance) or S-shaped structures (off resonance) in  $G_2$ . This S-shape is inverted on the other side of the resonance. The amplitudes and line shapes of these features are consistent with a finite lead resistance of the S-contact in the cryostat [63] and a capacitive coupling between the quantum dots, which leads to features characteristic for "charge detection" of the QD1 state by QD2 [137].

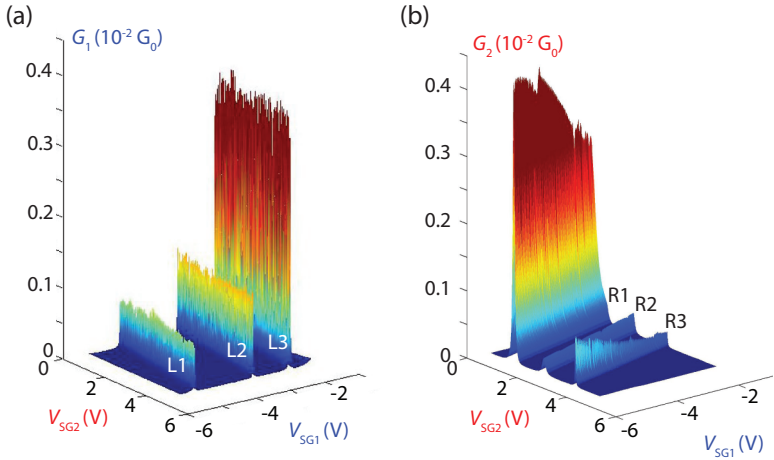


**Figure 6.5.:** (a) Normal state ( $B_{\parallel} = 250$  mT) differential conductance  $G_1$  of QD1, and (b)  $G_2$  of QD2, as a function of the side-gate voltages  $V_{SG1}$  and  $V_{SG2}$ . Compared to the superconducting state ( $B_{\parallel} = 0$ ) the overall conductance is strongly increased and the huge CPS peaks vanished.

## 6.4. Evaluation of the splitting efficiency

After having established that the non-local signals arise from CPS we want to quantify the CPS rates. To do so we use the amplitude  $\Delta G_2$  of the additional peak in  $G_2$  at the position of the QD1 resonance, as illustrated in Fig. 6.4(a). The subtracted background is determined by manually interpolating the bare QD2 resonance. In Fig. 6.4(a) we also define  $\delta V$ , the detuning between the two resonances. One finds that  $\Delta G_2$  depends strongly on the detuning  $\delta V$ . In Fig. 6.6(a) we therefore plot  $\Delta G_2$  vs.  $\delta V$ . The value that was extracted from the slice in Fig. 6.4(a) is marked by a red triangle. As another example, the conductance variation near the crossing (L3,R2) is also plotted in Fig. 6.6(a). For all crossings we find that  $\Delta G_2$  has a maximum at  $\delta V \approx 0$ , i.e. where both QDs are in resonance, in agreement with theoretical predictions [compare Eq.(3.15)]. For  $\delta V \neq 0$ ,  $\Delta G_2$  falls off rapidly and tends to zero on an energy scale consistent with the width of the respective resonances. We note that Hofstetter *et al.* observed a qualitatively different behaviour [63]. In their CPS experiment the non-local current was maximal when the second QD was positioned on the Coulomb peak tail ( $\delta V \neq 0$ ). As the double resonance condition was approached ( $\delta V \rightarrow 0$ ) the CPS currents decreased and eventually even turned negative for  $\delta V = 0$ . This unexpected behaviour may be attributed to the discrepancy between the experimental coupling regime ( $\Gamma_S + \Gamma_N \approx 500 \mu\text{eV} \gg \Delta \approx 150 \mu\text{eV}$  [63]) and the aspired working conditions ( $\Gamma_S < \Gamma_N < \Delta$  [84]).

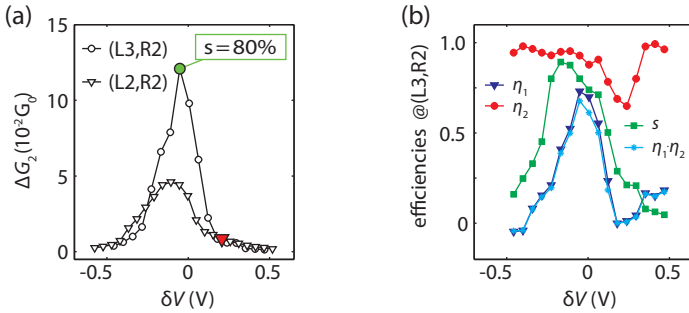


**Figure 6.6.:** (a)  $\Delta G_2$  as a function of the detuning  $\delta V$  between the resonances in QD1 and QD2 for the indicated resonance-crossings. (b) Plots of the visibilities  $\eta_i$ , the CPS efficiency  $s$  and  $\eta = \eta_1 \eta_2$ .

On the resonance crossings investigated here the maximum change in  $G_2$  is  $0.012 e^2/h$ . This number has to be compared to the total conductance,

including the local processes, so that we define the *visibility* of CPS in the second branch of the Cooper pair splitter as  $\eta_2 = \Delta G_2/G_2$  (similar for  $G_1$ ). The CPS visibilities for both branches on resonance crossing (L3,R2) are plotted in Fig. 3d.  $\eta_2$  is essentially constant over a large range of  $\delta V$  and reaches values up to 98%, i.e. the current in one branch can be dominated by CPS.  $\eta_1$ , however, has a maximum of only 73% at  $\delta V \approx 0$  and drops to zero for a large detuning.

As a measure for the CPS *efficiency* we compare the CPS currents to the total currents in both branches of the device. Assuming that CPS leads to a conductance  $G_{\text{CPS}}$  in each branch, independent of other processes, we define the CPS efficiency as

$$s = \frac{2G_{\text{CPS}}}{G_1 + G_2}. \quad (6.1)$$

By assuming that  $G_{\text{CPS}} = \Delta G_2$  we find efficiencies up to  $s \approx 90\%$ . Efficiencies up to 50% can also be reached when the splitting is procured by chance, as outlined in Sec. 3.2. Therefore our experiment provides a solid proof that the splitting is enforced by interactions.

The efficiency as a function of  $\delta V$  is plotted in Fig. 6.6(b) for the crossing (L3,R2). However, depending on the intended purpose of the entangler,  $s$  is not necessarily the relevant parameter. For example, in tests of Bell's inequality proposed for electrons [138, 139], the measured quantities are current cross correlations between the normal metal terminals, which suggests to use the following figure of merit:

$$\eta = \eta_1 \cdot \eta_2 = \frac{\Delta G_1}{G_1} \cdot \frac{\Delta G_2}{G_2} \quad (6.2)$$

A violation of Bell's inequality requires  $\eta > 1/\sqrt{2} \approx 71\%$ . In Fig. 6.6(b),  $\eta$  is plotted as a function of  $\delta V$  for the crossing (L3,R2). We find values up to  $\eta = 68\%$ , mostly limited by the large rates of local processes through QD1. Nonetheless, the large visibility in  $G_2$  demonstrates the feasibility of testing Bell's inequality with electrons, if an ideal detection scheme was available.

We note that there is no consensus in the literature about the definition of splitting efficiencies. Das *et al.* define efficiency as the ratio of CPS current and local background current:  $I_{\text{CPS}}/I_{\text{LPT}} \propto \Delta G_i/G_{\text{BG},i}$  with the local background conductance  $G_{\text{BG},i}$ , given by  $G_i = G_{\text{BG},i} + \Delta G_i$  [65]. This definition only considers one arm of the device and the efficiency can become infinitely large. In our terminology the splitting efficiencies of 100% (and above) that were reported in Ref. [65] correspond to CPS visibilities of 50% (and above).

Intuitively one might expect  $\Delta G_1 = \Delta G_2$ . This is found within experimental errors for 4 of the 9 resonance crossings. As an example,  $\Delta G_1$  and

$\Delta G_2$  of the crossing (L3,R2) investigated above are plotted as a function of  $\delta V$  in Fig. 6.8(a). For the other crossings, the two conductance variations deviate significantly from each other. 4 of the 9 crossings exhibit curves comparable to (L3,R1) plotted in Fig. 6.8(b). Here,  $\Delta G_2$  is larger than  $\Delta G_1$  by about a factor of 2, but with a similar curve shape. One of the 9 crossings, (L2,R1) shown in Fig. 6.8(c), is very peculiar: the variation in  $\Delta G_1$  is almost negligible, while  $\Delta G_2$  exhibits a pronounced peak. In addition, one finds that  $\Delta G_2 > G_1$ , i.e. the conductance variation in one branch is larger than the total conductance in the other.

## 6.5. Semi-classical master equation model

To qualitatively understand our experiments we discuss the electron dynamics in our devices using a strongly simplified semi-classical master equation model, graphically illustrated in Fig. 6.7. For each QD we consider a single level with constant broadening and a large charging energy. The system can be in one of the following four states  $k$ : both QDs empty, (0,0), either QD filled with one electron, (1,0) or (0,1), or both dots occupied, (1,1). The average occupation probability  $Q_k$  of each state is given by a rate equation of the form [140]

$$\frac{d}{dt}Q_k = \sum_{l=1}^N [p_{k,l}Q_l(t) - p_{l,k}Q_k(t)] \quad (6.3)$$

with the respective transition probabilities per time  $p_{k,l}$  being defined in Fig. 6.7. The first term describes transitions to the state  $k$ , while the second describes transition from  $k$  to any other state. We consider only transitions that correspond to the transport processes depicted in Fig. 6.1(a): CPS changes the system from (0,0) to (1,1) with a rate  $p_{\text{CPS}}$ , the transition from (1,x) to (0,x) is given by  $p_{\text{N1}}$  (similar for N2), the tunnelling between the QDs, i.e. from (0,1) to (1,0), by  $p_{12}$  (similar for the reversed tunnelling) and the transition from (0,x) to (1,x) is described by  $p_{\text{LPT1}}$  (similar for LPT2)<sup>2</sup>. We assume that electrons are transferred only in one direction, from S to the QDs and from the QDs to the respective normal metal contact. In this regard the  $p_{k,l}$  are *effective* rates. The model also neglects virtual intermediate states and coherent transition between them. We refer to Refs. [86–88] for models which take these into account. We explicitly assume that the QD spectra remain unaffected by S – a condition that will break

<sup>2</sup>The interpretation of  $p_{\text{LPT1}}$  is not trivial since it contains the tunnelling of the first and then the second electrons from S to QDi, and from QDi to Ni. However, we simply assume that both, the first and the second electron, lead to a change in the time-averaged dot occupation, treating LPT as one single transition.

down for a weak coupling  $N$  [96] – and simply choose effective values for the  $p_{k,l}$  that qualitatively reproduce the experiments. The main purpose of this ”toy model” is a pedagogic one: to illuminate the mutual influence that the transport processes have on each other.

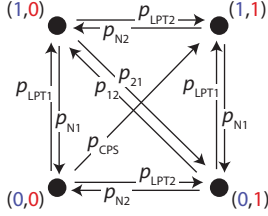


**Figure 6.7.:** Graphical representation of the semi-classical master equation model of a Cooper pair splitter. The four allowed states of the model – both QDs empty, (0,0), either QD filled with one electron, (1,0) or (0,1), or both dots occupied, (1,1) – are connected by transition rates that correspond to the processes illustrated in Fig. 6.1(a).

We solve Eq.(6.3) for the  $Q_k$  by using the maximal tree method, as described in detail in Ref. [140]. The solutions are found in Appendix B. To incorporate the QD resonances we multiply each probability with effective density of states in the the target state, assuming gate-dependent Lorentzian profiles  $\mathfrak{g}_1(V_{SG1})$  and  $\mathfrak{g}_2(V_{SG2})$  for QD1 and QD2:

$$\tilde{p}_{LPT1}(V_{SG1}) = p_{LPT1} \mathfrak{g}_1(V_{SG1}) \quad (6.4)$$

$$\tilde{p}_{LPT2}(V_{SG2}) = p_{LPT2} \mathfrak{g}_2(V_{SG2}) \quad (6.5)$$

$$\tilde{p}_{12}(V_{SG1}) = p_{12} \mathfrak{g}_1(V_{SG1}) \quad (6.6)$$

$$\tilde{p}_{21}(V_{SG2}) = p_{21} \mathfrak{g}_2(V_{SG2}) \quad (6.7)$$

$$\tilde{p}_{CPS}(V_{SG1}, V_{SG2}) = p_{CPS} \mathfrak{g}_1(V_{SG1}) \mathfrak{g}_2(V_{SG2}) \quad (6.8)$$

$$\tilde{p}_{Ni}(V_{SGi}) = p_{Ni} \quad (6.9)$$

Based on the occupation probabilities we calculate the conductances in units of  $G_0 = 2e^2/h$  as follows:

$$G_{CPS} = \tilde{p}_{CPS} Q_{(0,0)} \quad (6.10)$$

$$G_{LPT1} = \tilde{p}_{LPT1} (Q_{(0,1)} + Q_{(0,0)}) \quad (6.11)$$

$$G_{LPT2} = \tilde{p}_{LPT2} (Q_{(1,0)} + Q_{(0,0)}) \quad (6.12)$$

$$G_1 = \tilde{p}_{N1} (Q_{(1,0)} + Q_{(1,1)}) \quad (6.13)$$

$$G_2 = \tilde{p}_{N2} (Q_{(0,1)} + Q_{(1,1)}) \quad (6.14)$$

We then extract the conductance variations  $\Delta G_1$  in the same way as in the experiments, i.e. by taking the difference between the maximum and the minimum of the conductance  $G_1$  along a trace that follows the resonance maximum in  $G_2$ , and analogous for  $G_2$ . Appendix B contains a the code for a Matlab program to calculate  $\Delta G_1$ ,  $\Delta G_2$  and other quantities of interest.

## 6.6. Discussion of the model

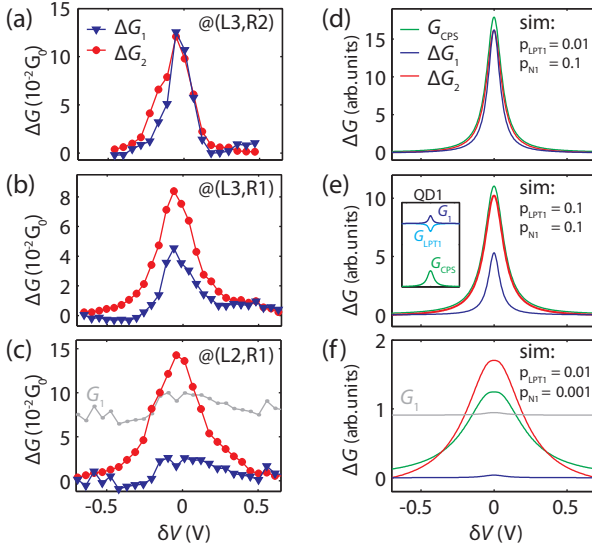


**Figure 6.8.:** (a)-(c)  $\Delta G_1$  and  $\Delta G_2$  as a function of the detuning  $\delta V$  for the indicated resonance crossings. (d)-(f) Similar plots obtained from the master equation model of CPS, including  $G_{\text{CPS}}$ . The parameters varied between the simulations are given in the figures. The inset in (e) shows the conductances in the branch of QD1 due to local processes ( $G_{\text{LPT1}}$ , CPS and at  $N1$ ).

Our model shows that a finite QD population can lead to a competition between the various transport mechanisms. In Figs. 6.8(d-f) simulated conductance variations are plotted for different QD1 parameters, while those of QD2 are kept at  $p_{\text{LPT2}} = 0.01$  and  $p_{\text{N2}} = 0.1$  for all plots, i.e. in the regime of Ref. [84], where the coupling to S is much weaker than to the normal contacts. We set  $p_{\text{CPS}} = 0.03$  to obtain conductances comparable to the experiments, and  $p_{12} = 0.001$  so that the inter-dot coupling is the smallest parameter in the problem. If the occupation of both QDs are negligible, i.e.  $p_{\text{LPT1}} \ll p_{\text{N1}}$ , one finds  $\Delta G_1 = \Delta G_2$ , as shown in Fig. 6.8(d), similar to the experiments presented in Fig. 6.8(a). For clarity we chose slightly different widths for the QD resonances.

If one QD occupation becomes significant, the conductance variations are not identical anymore. Figure 6.8(e) shows plots for  $p_{\text{LPT1}} = p_{\text{N1}} = 0.1$ , for which  $\Delta G_2 \approx 2\Delta G_1$ , as in the experiment shown in Fig. 6.8(b). The model

also allows us to calculate the rate at which Cooper pairs are extracted from S by CPS. The corresponding conductance is also plotted in Figs. 6.8(d-f). We find that  $\Delta G_i < G_{\text{CPS}}$  as long as the inter-dot coupling  $p_{12}$  is negligible, i.e. the experimentally extracted CPS conductance underestimates the actual value,  $\max(\Delta G_1, \Delta G_2) < G_{\text{CPS}}$ , which is explained as follows. The rate  $p_{N1}$  starts to limit the current. QD1 is not emptied fast enough, which inhibits the following processes on the dot resulting in a competition between the processes that fill QD1. An increase of CPS current is accompanied by a decrease of the LPT current (and vice versa). This is illustrated in the inset of Fig. 6.8(e), where the calculated local conductance from S to QD1,  $G_{\text{LPT1}}$ , has a minimum where  $G_{\text{CPS}}$  is maximal. The same suppression mechanism might also account for the discrepancy between noise correlations and conductance measurements in Ref. [65].

The situation is more complex if the tunnel coupling between the dots becomes relevant. For example, if  $p_{N1} = p_{12} = 0.001$  and  $p_{\text{LPT1}} = 0.01 > p_{N1}$ , as used for Fig. 6.8(f), the electrons can leave QD1 to N1 and to QD2 with the same probability. Since  $p_{N1}$  is small, this quenches  $G_1$ , but  $G_2$  is increased due to the additional current from QD1. Here, the  $\Delta G_i$  do not give an upper or lower bound for the CPS rate and  $\Delta G_2$  can become larger than  $G_1$ , as in the experimental curves in Fig. 6.8(c). We note that the discussed situations are not in the regime of completely filled QDs. Our model suggests that in this unitary limit the conductances can be reduced considerably in the center of a resonance crossing, which might account for the yet unexplained anomalous behaviour of the on-resonance signals in [63].

## 6.7. Outlook: niobium based Cooper pair splitters

Above we showed that a regime can be reached in which Cooper pairs are split with efficiencies up to 90%. However, a near-ideal Cooper pair splitter is not necessarily a near-ideal electron entangler. One serious source of entanglement loss are electron-hole (e-h) pair excitations in which electrons hop from the Fermi leads onto the QDs [84]. As discussed in Section 3.2, such excitations can be suppressed by positioning the QD resonances above the chemical potentials of the N-leads, while keeping the dots resonant, i.e.  $\mu_S = \mu_{\text{QDi}} > \mu_{\text{Ni}}$ . But this is barely possible if the level broadening of the resonance is of similar magnitude as the induced superconducting gap,  $\Gamma \approx \Delta$ . The bias voltage one would need to apply to exclude e-h pair excitations would be large enough to break up Cooper pairs and let them escape as quasiparticles. A CPS entangler requires therefore that  $\Gamma$  and  $\Delta$  are well separated. This can be reached by decreasing  $\Gamma$  or by increasing

$\Delta$ . Since the current fabrication techniques barely provide control over the tunnel couplings we chose to work with superconducting materials that exhibit larger energy gaps.

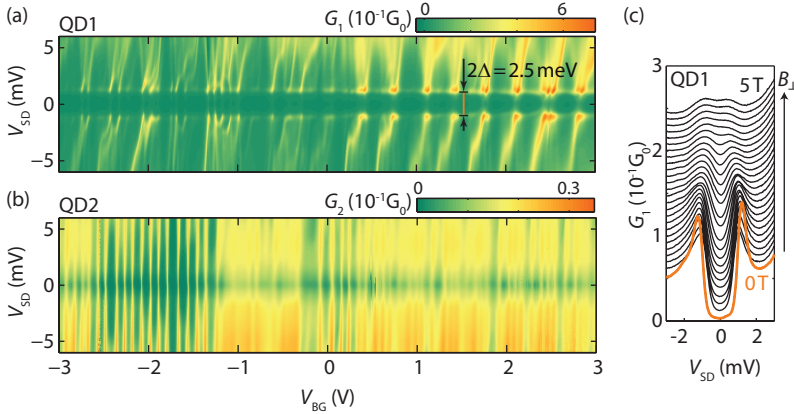


**Figure 6.9.:** (a,b) Simultaneous recorded differential conductance maps  $G_i(V_{SD}, V_{BG})$  ( $i = 1, 2$ ) of the two QDs from a Nb based CPS device. QD1 (a) shows a hard transport gap of  $2\Delta = 2.5$  meV, but QD2 (b) shows only a very weak and inconclusive features of a soft transport gap. (c) Magnetic field evolution differential the conductance  $G_1(V_{SD})$  of QD1 measured at  $V_{BG} = 1.6$  V. The spacing between the splices is 0.2 T. Note that the induced energy gap is about ten times larger than for Fig. 6.2(a).

Figure 6.9 shows the two stability diagrams of a CPS device for which we used a Ti/Nb (3 nm/50 nm) bilayer as superconducting contact. The device was fabricated according to the recipe given in Section 5.2 that involves the cleaning and pre-selection of CNTs by hydrogen radical etching. The stability diagram of QD1, shown in Fig. 6.9(a), exhibits a transport gap of  $2\Delta$  with  $\Delta = 1.25$  meV. The magnetic field evolution of the gap is shown in Fig. 6.9(c) where we plot  $G_1(V_{SD})$  measured at  $V_{BG} = 1.6$  V. As in Fig. 6.2(a) a BCS-like density of states is impinged on the background conductance of QD1 and a critical magnetic field  $B_c \sim 4$  T can be deduced. The induced superconducting gap is close to the bulk value for niobium,  $\Delta_{Nb} = 1.45$  meV [141], and about 10 times larger than the aluminium induced gap in Fig. 6.2(a). To our knowledge such large superconducting energy gaps were not reported yet for CNT QDs.<sup>3</sup> Nevertheless, the reli-

<sup>3</sup>In Ref.[142] induced gaps of  $\Delta \sim 0.25$  meV were reported for Nb contacted CNTs. In Ref. [143] multi-walled CNTs with Nb contacts were investigated. Supercurrent was measured, but no superconducting gaps were observed. Ref. [144] reports quasi-

able implementation of CNT devices with large superconductivity induced energy gaps ( $\Delta \gtrsim 0.5$  meV) remains a challenge. As an example the reader may consider the stability diagram of the second QD, shown in Fig. 6.9(b). A weak conductance suppression for  $|eV_{SD}| < 1.25$  meV points towards the existence of a soft superconducting gap, but the respective features are too smeared to be conclusive. Also, we were not able to observe any non-local conductance correlations between QD1 and QD2 for this device.

The key problem in the fabrication of CNT based CPS devices are the random variations of the contact properties. To obtain a device with two QDs that show a hard energy gap and obey the same coupling asymmetry,  $\Gamma_{Si} \ll \Gamma_{Ni}$ , one needs an appreciable share of luck.

## 6.8. Conclusions

We presented Cooper pair splitting experiments with efficiencies up to 90%, demonstrating the importance of electron-electron interactions in such systems. For the figure of merit relevant in tests of Bell's inequality for elections we find values close to the required limits. In addition, we assessed CPS on both QDs and found rather large apparent discrepancies between the CPS signals in the two output terminals. We explained these discrepancies in a semi-classical master equation model. Our model suggests that for negligible inter-dot couplings the experimentally extracted CPS rates are a lower bound to the real CPS rates. Our experiments and calculations show that there is a large variety of different transport phenomena in CPS devices that need further investigation. In addition we showed that niobium contacted CNTs can exhibit superconductivity induced energy gaps on the meV scale. Both findings are important steps on the way to a Bell experiment in which the spins of single electrons are used as flying qubits.

---

particle peaks at  $\Delta \approx 1 - 1.5$  meV, but the investigated Nb-junction used several CNTs in parallel to form a weak link. Alternatively, rhenium [145] and molybdenum/rhenium alloys [146] were successfully used as CNT contacts. In Ref. [145] a superconducting gap of  $\Delta \sim 0.1$  meV is visible while in the supplementary material of Ref. [146] shows no signs of an induced gap, although the main text clearly demonstrates supercurrent.

## Non-local spectroscopy of Andreev bound states

In this chapter we will discuss a device which looks very similar to the Cooper pair splitter presented in the preceding chapter. However, despite the similar geometry of the devices, we will encounter completely different physics. It will turn out, that the device we investigate in this chapter has one QD which is strongly coupled to the superconductor (S), while the second QD is weakly coupled to S. As a result, the strongly coupled QD forms Andreev bound states (ABSs). The second QD forms no ABSs, but it can be used to probe the ABSs on QD1 non-locally via CPS and elastic co-tunnelling. We find an appreciable non-local conductance with a rich structure, including a sign reversal at the ground state transition from the ABS singlet to a degenerate magnetic doublet. We describe our device by a simple rate equation model that captures the key features of our observations and demonstrates that the sign of the non-local conductance is a measure for the charge distribution of the ABS, given by the respective Bogoliubov-de Gennes amplitudes  $u$  and  $v$ .

### 7.1. Introduction

#### 7.1.1. Local spectroscopy of ABS

The proximity allows superconducting order to leak into a QD. As we discussed in Chapter 3 this may lead to the formation of ABSs. In a pictorial

way, one might think of the ABSs as emerging from the superposition of virtual Andreev reflections at the interface between the QD and a superconducting electrode (S). In each such Andreev reflection, a Cooper pair (virtually) enters or leaves the QD, thereby mixing the even charge states of the QD. In the so-called superconducting atomic limit, the ABS can be expressed as a BCS-like superposition of an empty and a doubly occupied QD level, denoted as  $|-\rangle = u|0\rangle - v^*|\uparrow\downarrow\rangle$  (see Sec. 3.3). The  $|-\rangle$  state is characterized by its energy  $E_-$  and by the Bogoliubov-de Gennes (BdG) amplitudes  $u$  and  $v$ . The odd charge states are not affected by the BCS condensate and remain eigenstates of the QD, forming a spin-degenerate doublet  $\{|\uparrow\rangle, |\downarrow\rangle\}$  [95–97].

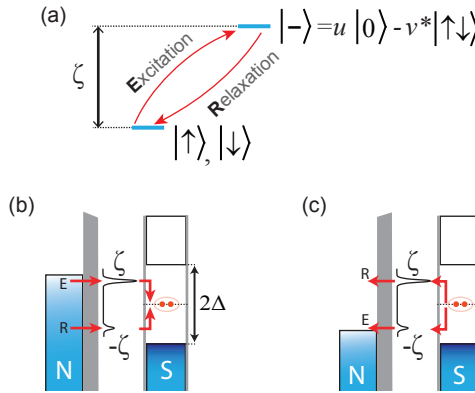


**Figure 7.1.:** (a) Example of the low-energy excitation spectrum of a QD-S device, with the magnetic doublet as GS, separated from the ABS by the Andreev addition energy  $\zeta$ . (b) Energy diagram of the local Andreev transport through a normal conducting tunnel probe. The alternation of an excitation and a relaxation process (labelled E and R) converts a normal current into a supercurrent. (c) Transport process at negative bias.

The low-energy excitation spectrum of a QD-S system is shown schematically in Fig. 7.1(a), where we chose the magnetic doublet to be the ground state (GS) and the ABS to be the excited state (ES). A natural experiment to measure the Andreev addition energy  $\zeta = |E_- - E_{\uparrow,\downarrow}|$ , defined as the energy difference between ABS and magnetic doublet, uses a normal conducting tunnel probe (N) in a N-QD-S geometry. If the tunnel coupling between N and the QD,  $\Gamma_N$ , is sufficiently weak, the influence of the tunnel probe on the QD-S excitation spectrum is negligible and the differential conductance across the device,  $G = \partial I / \partial V_{SD}$ , shows a peak for  $|eV_{SD}| = \zeta$

[56, 70–73, 101].

This peak in differential conductance represents the onset of a current through the Andreev channel when the electrochemical potential of the tunnel probe,  $\mu_N$ , exceeds the addition energy,  $\zeta$ , as depicted in Fig. 7.1(b). This allows an electron to tunnel across the barrier  $\Gamma_N$  and excite the QD, even in the presence of a large charging energy  $U \gg \zeta$ . The electron does not enter the  $|\uparrow\downarrow\rangle$  state, but the  $|-\rangle$  state, where the charge is shared between QD and S. The probability of this transition,  $|\uparrow\rangle \xrightarrow{+1e} |-\rangle$ , scales with  $v^2$ , the weight of the  $|\uparrow\downarrow\rangle$  term in the  $|-\rangle$  state [147]. To relax back to the GS, the QD takes up a second electron at negative energy  $-\zeta$  from N, which is equivalent to the emission of a hole with energy  $\zeta$  into N. The rate of this relaxation process is proportional to  $u^2$ , the probability to find the QD empty so that an electron can be added to reach the  $|\uparrow\rangle$  state. A complete transport cycle,  $\text{GS} \rightarrow \text{ES} \rightarrow \text{GS}$ , reflects an incoming electron as a hole and transfers a Cooper pair to S with a probability proportional to  $u^2 v^2$ .

Since the  $|-\rangle$  state is a superposition of an empty and a doubly occupied QD level, the same ES can be reached either by addition of an electron with positive energy  $\zeta$  to the GS, or by removal of an electron with negative energy  $-\zeta$  from the GS. Consequently, the Andreev resonances are always observed symmetrically about Fermi level of the superconductor, which we define as reference potential  $\mu_S = 0$ . In case of a negative bias,  $\mu_N \leq -\zeta$ , the QD is excited by removing an electron with negative energy  $-\zeta$  from the QD and transferring it to N, as shown in Fig. 7.1(c). The probability of this excitation,  $|\uparrow\rangle \xrightarrow{-1e} |-\rangle$ , scales with  $u^2$ . Compared to the situation in Fig. 7.1(b) the rates for excitation and relaxation are inverted and the direction of electron flow is reversed, but the Andreev current is again proportional to  $u^2 v^2$ . Therefore local spectroscopy of ABS is not able to investigate the excitation and relaxation process individually in a controlled manner.

### 7.1.2. Non-local spectroscopy of ABS

When a current is passed through the Andreev channel the QD fluctuates between  $\{|\uparrow\rangle, |\downarrow\rangle\}$  and  $|-\rangle$ . In each such fluctuation the QD state changes between even and odd occupation, which requires the addition or removal of a single electron to the QD. If only local processes are considered the S contact can not drive such transitions because the electrons at energies below  $\Delta$  are paired and form a so-called BCS condensate. However, if a second QD is added to the QD-S system, higher-order processes involving electrons from the second QD can deliver single electrons at sub-gap energies to one side of the superconductor.

Figure 7.2(a) shows a sketch of the device geometry we consider. Two

QDs (QD1 and QD2) are connected to two normal conducting drains (N1 and N2) and one common superconducting source. One possible process, in which the S-contact can excite QD1, is elastic co-tunnelling: an electron at energy  $\zeta$  tunnels from QD2 to QD1 via a virtual quasiparticle state in S. Another mechanism is crossed Andreev reflection, also known as Copper pair splitting (CPS): a Cooper pair is coherently split into two electrons at opposite energies, here  $\zeta$  and  $-\zeta$ , that leave S at different sites [84]. In Chapter 6 we demonstrated that the splitting of Cooper pairs can be controlled by tuning the levels of the individual QDs with local gates (see also Refs. [63–66, 148]). Compared to the preceding chapter we explore a new coupling regime, summarized in Fig. 7.2(a), which leads to the formation of ABSs on QD1. We then employ the non-local transport mechanisms to excite these ABS. Thus, in our device the Cooper pairs play a twofold role. On the one hand, the Cooper pair condensate mixes the even charge states of QD1 as a result of the proximity effect. On the other hand, Cooper pairs can be split into individual charges that drive QD1 from even to odd occupation (or vice versa) with the assistance of QD2.

Since CPS and elastic co-tunnelling are coherent processes with electrons from two spatially separated QDs, we refer to them as non-local. In this chapter we use local tunnelling spectroscopy to identify ABSs and then investigate the response of the ABS channel to non-local excitations. In section 7.2 we describe how the double QD device is realized with a carbon nanotube and present local and non-local transport measurements. In section 7.3 we introduce a simple rate equation model that explains our main experimental findings. We show that the non-local current reflects the relative amplitudes of the BdG amplitudes. In section 7.4 we summarize the results and conclude that non-local transport measurements provide a novel spectroscopic tool to investigate the charge distribution of the ABS – an information that complements the knowledge of the Andreev addition energy  $\zeta$  accessed by local tunnelling spectroscopy.

## 7.2. Experiment

### 7.2.1. Device and measurement set-up

Figure 7.2(b) shows a colored scanning electron micrograph of our device and schematically the measurement set-up. The device was fabricated from a hydrogen radical inert CNT, according to the recipe given in Sec. 5.2. A Nb lead (50 nm thick, 170 nm wide), with a Ti contact layer (3 nm thick) below, serves as superconducting reservoir. Together with two Ti/Au contacts (5/50 nm thick) the S contact defines two QDs. The QDs can be tuned by applying a voltage  $V_{BG}$  to the Si substrate, or by applying a voltage  $V_{SG2}$

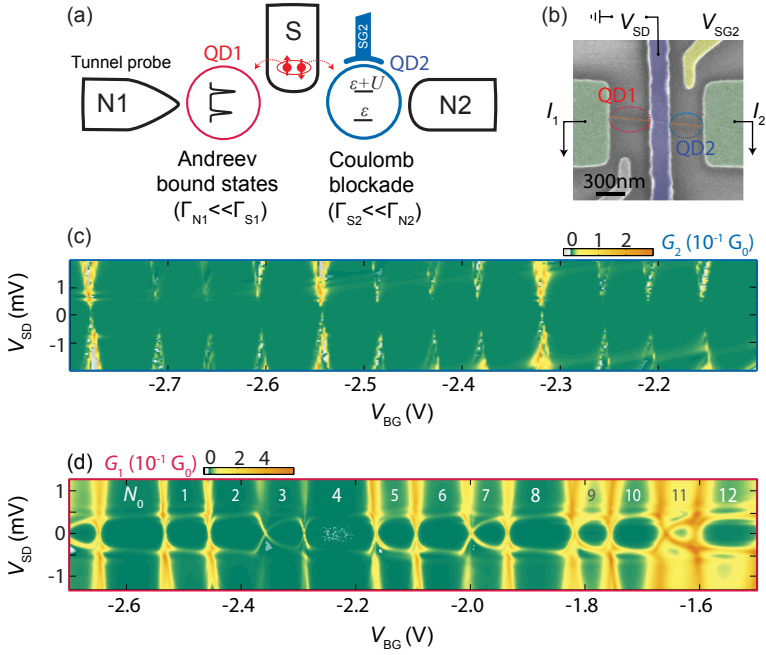


**Figure 7.2.:** (a) Device schematic: two QDs are coupled to a common superconducting reservoir and two independent normal leads. The tunnel couplings follow  $\Gamma_{N1} \ll \Gamma_{S1}$  and  $\Gamma_{S2} \ll \Gamma_{N2}$ . The subscript S/N labels the contact and the numbers refer to the respective QD. When both QDs are resonant Cooper pairs can split and leave S at different sites, thereby exiting the ABS on QD1. (b) Coloured SEM micrograph of the device and measurement set-up. (c,d) Differential conductances  $G_2$  and  $G_1$  as a function of the common source drain voltage,  $V_{SD}$ , and back gate voltage,  $V_{BG}$ .

to a local side gate in the vicinity of QD2. The side gate of QD1 was not connected, due to a defect. In comparison to Chapter 6 we will measure non-local signals also at finite bias voltages,  $V_{SD}$ , which are applied to the S contact. We use two independent current voltage converters at N1 and N2 to obtain the currents through QD1 and QD2. The differential conductances through QD1,  $G_1 = \partial I_1 / \partial V_{SD}$ , and through QD2,  $G_2 = \partial I_2 / \partial V_{SD}$ , are measured simultaneously by standard lock-in technique, while varying the gate voltages and  $V_{SD}$ . All measurements are carried out in a dilution refrigerator at a base temperature  $T \approx 25$  mK.

### 7.2.2. Local transport measurements

The structure of the stability diagrams differs strongly for QD1 and QD2. The stability diagram of QD2 [Fig. 7.2(c)] shows the well known pattern of Coulomb diamonds, disconnected by an induced transport gap of  $2\Delta$  due to the superconductor, from which we extract  $\Delta \approx 0.5$  meV. For voltages  $|eV_{SD}| < \Delta$  the conductance through QD2 is suppressed by a factor of  $\sim 10$ .

The conductance map for QD1 is shown in Fig. 7.2(d) and 7.3(c), which zooms into the gate range around a diamond with odd occupation. Again the conductance is suppressed for  $|V_{SD}| < 0.5$  mV, but inside the superconducting gap we observe two lines, positioned symmetrically about  $V_{SD} = 0$ , that cross each other near the diamonds edges. We interpret these sub-gap features as Andreev resonances at  $\pm\zeta$ . The crossing of two Andreev resonances at zero energy is associated with a quantum phase transition in which the GS of the QD changes from the  $|-\rangle$  singlet to the magnetic doublet, or vice versa [71, 72, 96]. For odd occupation numbers the Coulomb repulsion, which favours the doublet GS, can prevail over the superconducting pairing, which favours the ABS as GS. At the phase boundary the energy of the  $|-\rangle$  state equals the energy of the magnetic doublet and hence the Andreev resonances cross, i.e.  $\pm\zeta = 0$ . For even occupation, where the QD is in the  $|-\rangle$  GS, we find that the Andreev addition energy is pinned close to the gap edge,  $\zeta \approx \Delta$ , as discussed in Sec. 3.3.

Both QDs have similar charging energies of  $\sim 5$  meV and their stability diagrams exhibit a fourfold symmetry that is characteristic for clean CNT devices [134]. However, remaining disorder and spin orbit interactions lift the fourfold degeneracy, breaking up the CNT shells into two pairs of Kramer doublets [149]. For QD1 we evaluate the separation between both Kramer doublets to be  $\delta = 1 \pm 0.3$  meV. Thus we treat the ABS as emerging from two-fold spin-degenerate energy levels, neglecting the influence of the additional orbital degree of freedom on the ABS spectrum.

### 7.2.3. Non-local conductance correlations

CPS and elastic co-tunnelling involve electron exchange with both QDs and can therefore be identified by studying correlations between the conductances  $G_1$  and  $G_2$ . By tuning QD2 from Coulomb blockade to resonance, or vice versa, the non-local transport processes can be switched on and off, provided  $|eV_{SD}| \geq |\zeta|$ . In Figs. 7.3(a) and 7.3(b) we plot  $G_1$  and  $G_2$  as a function of the voltage applied to the local side gate at QD2. When a resonance of QD2 enters the bias window, which was set to  $V_{SD} = 0.375$  mV, a sudden increase in the differential conductance  $G_2$  is observed. These peaks in  $G_2$  are accompanied by a conductance change  $\Delta G_1$  in  $G_1$ . We ascribe

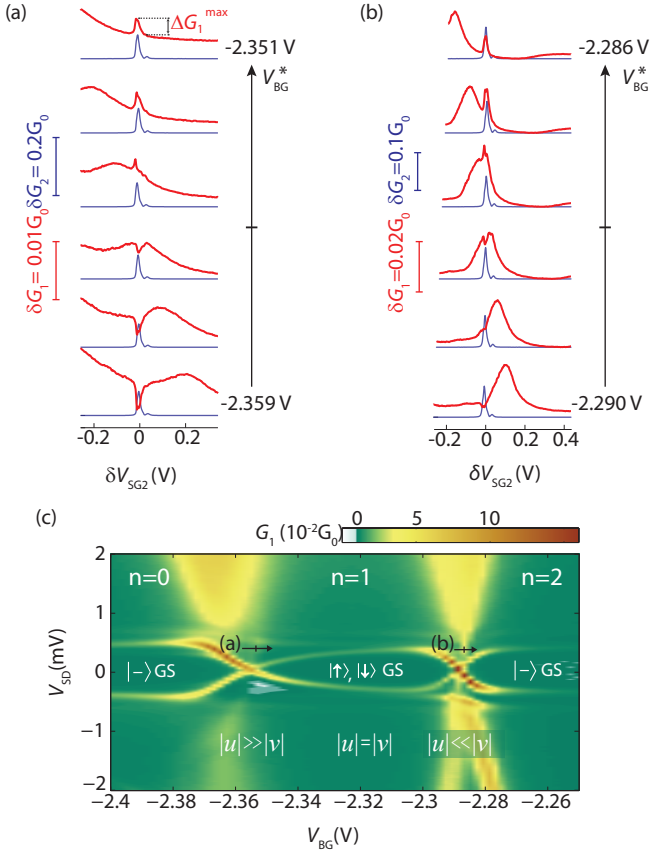


**Figure 7.3.:** (a,b) Simultaneously recorded differential conductances  $G_1$  and  $G_2$  as a function of  $\delta V_{SG2} = V_{SG2} - \hat{V}_{SG2}$  for increasing values of  $V_{BG}^* = V_{BG} + \alpha \hat{V}_{SG2}$ . The source drain voltage was kept fixed at  $V_{SD} = 0.375$  mV. The resonances in  $G_2$  are accompanied by a non-local conductance change  $\Delta G_1$  in  $G_1$ . (c) Stability diagram  $G_1(V_{SD}, V_{BG})$  for QD1 measured at  $V_{SG2} = 0$ . The black arrows indicate the direction along which the non-local signal is probed in (a,b). The sign change of  $\Delta G_1$  coincides with the GS transitions of QD1.

these correlations  $\Delta G_1(G_2)$  to the non-local conductance caused by CPS and elastic co-tunnelling. To substantiate this interpretation we note that the conductance correlations tend to zero when superconductivity is suppressed, either by raising the temperature above 500 mK or by applying an

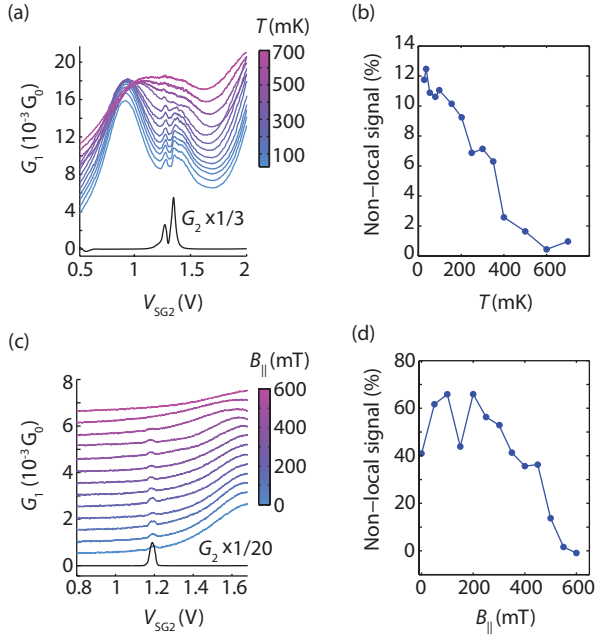


**Figure 7.4.:** (a) Simultaneously recorded  $G_1$  and  $G_2$  as a function of  $V_{SG2}$  at  $V_{BG} = -1.958$  V and  $V_{SD} = -0.45$  mV. The non-local conductance variations  $\Delta G_1$  tend to zero as the base temperature is increased. (b) Visibility of the non-local signal  $\Delta G_1/G_1$  vs.  $T$  obtained from the data shown in (a). (c) Simultaneous recorded  $G_1$  and  $G_2$  as a function of  $V_{SG2}$  at  $V_{BG} = 15.583$  V and  $V_{SD} = 0$  mV. The non-local conductance variations  $\Delta G_1$  tend to zero when an external magnetic field is applied. The field direction is parallel to the plane of the S-contact. (d) Visibility of the non-local signal  $\Delta G_1/G_1$  vs.  $B_{||}$  obtained from the data shown in (c).

external magnetic field  $B_{||} > 500$  mT as shown in Fig. 7.4.

By repeating these correlation measurements for many consecutive values of  $V_{BG}$  we can map out how the non-local signal depends on the energy level configuration of QD1. To correct for the capacitive cross-talk from the side gate to QD1 we introduce the new variable  $V_{BG}^* = V_{BG} + \alpha \hat{V}_{SG2}$ . Here  $\hat{V}_{SG2}$  is the side gate voltage for which the non-local conductance takes its maximal value,  $\Delta G_1^{\max}$ , and  $\alpha = 1.56 \times 10^{-2}$  is a geometry dependent factor that accounts for the respective gate efficiency. The variable  $V_{BG}^*$  allows to assign a position in the stability diagrams of QD1, measured at  $V_{SG2} = 0$ , to the non local signals, measured at  $\hat{V}_{SG2} \neq 0$ . In Fig. 7.3(c), we indicate the direction along which  $\Delta G_1^{\max}$  is probed in Fig. 7.3(a,b) by black arrows.

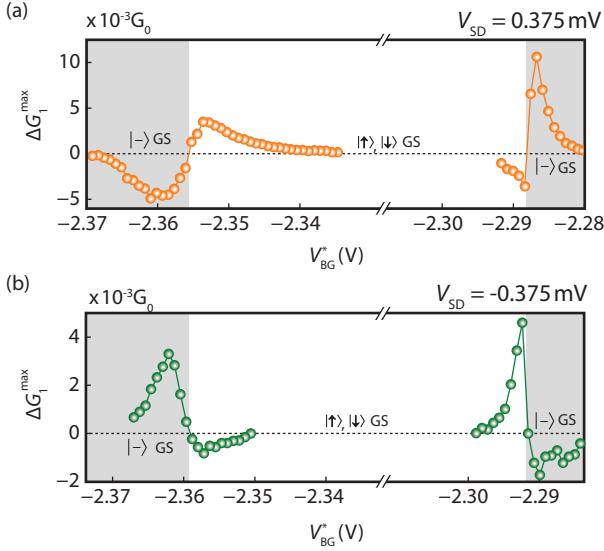


**Figure 7.5.:** Magnitude of the non-local differential conductance,  $\Delta G_1^{\max}$ , as a function of  $V_{BG}^*$ , the back gate voltage corrected for the capacitive cross-talk from the side gate (see text). A bias of  $V_{SD} = 0.375$  mV (a) and  $V_{SD} = -0.375$  mV (b) was applied to the S contact.

The conductance correlations can be either positive or negative, i.e.  $G_1$  can show a peak or a dip at the QD2 resonance, depending on  $V_{BG}^*$ . Strikingly, the turnover from a negative to a positive non-local conductance coincides with the quantum phase transition in which the GS changes from the ABS singlet to the magnetic doublet.

In Fig. 7.5 we plot the evolution of  $\Delta G_1^{\max}$  over the complete back gate range of an odd QD1 state for opposite bias voltages  $V_{SD} = \pm 0.375$  mV. Starting from the left side of Fig. 7.5(a) a negative non-local signal starts to build up when the Andreev resonance enters the bias window,  $\zeta < |e|V_{SD} = 0.375$  mV, at  $V_{BG}^* \approx -2.37$  V. The magnitude of  $\Delta G_1^{\max}$  increases towards the singlet–doublet phase boundary where it rapidly changes sign. In the doublet GS region, the positive correlations decay and become immeasurably small around the centre of the plot. As the right GS transition is approached the non-local signal builds up again, but with a negative sign. Around  $V_{BG}^* \approx -2.288$  V, where we expect the  $| \rightarrow \rangle$  state to become the GS, the sign of  $\Delta G_1^{\max}$  is again inverted. The evolution of the non-local signal at

a negative bias voltage of  $V_{SD} = -0.375$  mV, shown in Fig 7.5(b), exhibits a similar behaviour, except for a sign change that results from the reversal of the bias voltage.

Comparing the left and the right side of Figs. 7.5(a) and 7.5(b) we notice a sharper reversal of  $\Delta G_1^{\max}$  at the right GS transition. However, the slope of the dispersion  $\zeta(V_{BG})$  in Fig. 7.3(c) is also steeper at the right GS transition, implying a more rapid crossover between different GSs than for the left GS transition. We speculate that this asymmetry results from a gate dependence of  $\Gamma_{S1}$ , which decreases for increasing  $V_{BG}$ .

The sign change of the non-local signal is reminiscent of the  $0-\pi$  transition in S-QD-S Josephson junctions. There, a reversal of the supercurrent across the device is observed when the GS of the QD changes from singlet to doublet [56, 62, 150, 151]. However, the back gate evolution of  $\Delta G_1^{\max}$  demonstrates that the sign of the non-local signal is not merely determined by the GS of QD1, but also changes in the doublet GS region and under reversal of bias voltage. Hence, the sign of  $\Delta G_1$  can not be explained by analogy to the supercurrent reversal at the  $0-\pi$  transition.

### 7.3. Model

To understand the nature of the observed non-local signals we discuss the relevant transport processes and their impact on the conductance  $G_1$ . Assuming  $|e|V_{SD} > \zeta$ , the local Andreev channel gives rise to a background current that flows from N1 to S, as shown in Fig. 7.6(a), where  $t_e$  and  $t_r$  denote the rate of the local excitation and the local relaxation by electrons from N1. If QD2 is tuned into resonance it can provide single electrons with energy  $\zeta$ . This configuration allows the non-local creation of Cooper pairs in a process inverse to CPS: an electron from QD2 with energy  $\zeta$  and an electron from QD1 with energy  $-\zeta$  pair up and enter S in a distance on the order of the superconducting coherence length [Fig. 7.6(b)]. We refer to the rate of this process as  $t_{CPS}$ . In addition, an electron from QD2 can also co-tunnel via a quasiparticle state in S and excite QD1, as shown in Fig. 7.6(c), where we define the rate of elastic co-tunnelling as  $t_{EC}$ .

We note that non-local relaxation processes, which require that QD2 absorbs electrons at energy  $\zeta$ , are suppressed by the coupling asymmetry of QD2: The condition  $\Gamma_{S2} \ll \Gamma_{N2}$  implies that QD2 is refilled much faster from N2 than from S. Therefore, the relaxation of QD1 is dominated by the same local process, independent of the nature of the preceding excitation.

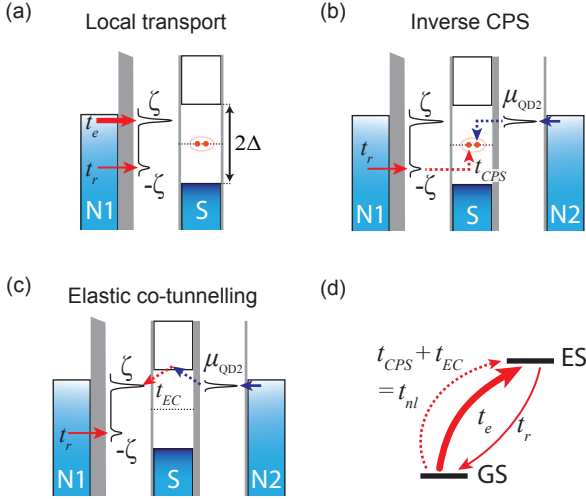


**Figure 7.6.:** (a-c) Energy diagrams of the local and non-local transport processes considered in our model. (d) Two-level rate equation model for QD1. The non-local processes with rate  $t_{nl}$  (red dashed arrow) only change the occupation probabilities but do not contribute to the current through N1.

### 7.3.1. Rate equation

To model the conductance through QD1 we formulate a two-level rate equation, graphically illustrated in Fig. 7.6(d). The steady state occupation probabilities of GS and ES, denoted  $P_{GS}$  and  $P_{ES} = 1 - P_{GS}$ , are given by

$$\frac{d}{dt} P_{ES} = (t_e + t_{nl}) P_{GS} - t_r P_{ES} = 0, \quad (7.1)$$

where  $t_{nl} = t_{CPS} + t_{EC}$  is the sum of both non-local excitation rates.

From the occupation probabilities one can calculate the current through the tunnel probe N1

$$I_1 = \frac{e}{h} (t_e P_{GS} + t_r P_{ES}). \quad (7.2)$$

The influence of  $t_{nl}$  on  $I_1$  is hidden in the occupation probabilities  $P_{GS}$  and  $P_{ES}$ , which are modified according to Eq. (7.1) when  $t_{nl}$  changes. The non-local excitations, depicted by the dashed arrows in Fig. 7.6(b,c), do not exchange electrons with N1. Hence the current through the barrier  $\Gamma_{N1}$  is only carried by local excitation and relaxation processes. In the absence

of non-local transport, Eq. (7.2) simplifies to  $I_1(t_{n\ell} = 0) = \frac{e}{\hbar} \frac{2t_e t_r}{t_e + t_r}$ . To calculate the non-local current, we subtract this local background from the total current, which yields

$$\begin{aligned} \Delta I_1 &= I_1(t_{n\ell} \neq 0) - I_1(t_{n\ell} = 0) \\ &= \frac{e}{\hbar} t_{n\ell} P_{\text{GS}} \frac{t_r - t_e}{t_r + t_e}. \end{aligned} \quad (7.3)$$

As one may expect, the non-local current is proportional to the excitation rate  $t_{n\ell}$  and the occupation probability of the GS,  $P_{\text{GS}} = t_r / (t_e + t_r + t_{n\ell})$ . However, the sign of  $\Delta I_1$  is determined by  $t_r - t_e$ , the relative strength of the local rates  $t_e$  and  $t_r$ . This can be understood by considering a very asymmetric situation,  $t_r \ll t_e$ , as assumed in Fig. 7.6.  $t_r$  limits the current and the QD is "stuck" in the ES most of the time. The non-local processes increase this imbalance, but without contributing to the current through N1. The QD gets even more "stuck" in the ES and the current flow is hindered,  $\Delta I_1 < 0$ . In the reversed situation,  $t_r \gg t_e$ , the excitation rate is the bottleneck. Here, the non-local excitations bypass this bottleneck, leading to an increased current,  $\Delta I_1 > 0$ . When the asymmetry between  $t_e$  and  $t_r$  decreases the sign of  $\Delta I_1$  remains the same, but the non-local current also decreases and finally vanishes for  $t_e = t_r$ .

The gate evolution of the rates  $t_e$  and  $t_r$  is determined by the physics of ABSs. We first discuss these rates in the limit  $\Delta \rightarrow \infty$ , where analytic expressions for the eigenstates of the QD-S system can be found. Later we compare these results to numerical calculations from the literature that consider a finite gap and therefore represent a more realistic scenario.

Figure 7.7(a) shows the dispersion relation of the Andreev resonance in the limit  $\Delta \rightarrow \infty$  calculated with the analytic expressions given in [95] for  $\Gamma_{\text{S1}} = 0.37$  in dimensionless energy units. The energy level of the QD,  $\epsilon_d$ , is parametrized by  $\delta = \epsilon_d + U/2$ . The local transport rates can be calculated with Fermi's golden rule [97, 147], which yields

$$\begin{aligned} |\sigma\rangle \xrightarrow{+1e} |-\rangle : t_e^+ &= \Gamma_{\text{N1}} \underbrace{|\langle - | d_{\bar{\sigma}}^\dagger | \sigma \rangle|^2}_{v^2} f_1(\zeta) \\ |-\rangle \xrightarrow{+1e} |\sigma\rangle : t_r^+ &= \Gamma_{\text{N1}} \underbrace{|\langle \sigma | d_{\bar{\sigma}}^\dagger | - \rangle|^2}_{u^2} f_1(-\zeta) \end{aligned} \quad (7.4)$$

and

$$\begin{aligned} |\sigma\rangle \xrightarrow{-1e} |-\rangle : t_e^- &= \Gamma_{\text{N1}} \underbrace{|\langle - | d_{\sigma} | \sigma \rangle|^2}_{u^2} (1 - f_1(\zeta)) \\ |-\rangle \xrightarrow{-1e} |\sigma\rangle : t_r^- &= \Gamma_{\text{N1}} \underbrace{|\langle \sigma | d_{\bar{\sigma}} | - \rangle|^2}_{v^2} (1 - f_1(-\zeta)). \end{aligned} \quad (7.5)$$

Here  $f_1(E)$  is the Fermi function of the lead N1,  $d_\sigma^\dagger$  ( $d_\sigma$ ) is the creation (annihilation) operator of QD1 for an electron with spin  $\sigma = \uparrow, \downarrow$  and  $\bar{\sigma}$  denotes the spin opposite to  $\sigma$ . For a sufficiently positive bias  $|e|V_{SD} > \zeta$  we can approximate  $f_1(\pm\zeta) \approx 1$ , hence the rates  $t_e^-$  and  $t_r^-$  can be neglected. In Fig. 7.7(c) we plot the rates  $t_e^+$  and  $t_r^+$  which reflect the evolution of the BdG amplitudes  $v^2$  and  $u^2$  with the QD energy. When the GS changes the initial and final states of the respective matrix elements are interchanged and the rates  $t_e^+$  and  $t_r^+$  are inverted.

The non-local excitation rate relevant for positive bias can be written as

$$|\sigma\rangle \rightarrow |-\rangle : t_{n\ell}^+ = \left( k_{\text{CPS}} |\langle -|d_\sigma|\sigma\rangle|^2 + k_{\text{EC}} |\langle -|d_{\bar{\sigma}}^\dagger|\sigma\rangle|^2 \right) \times \Gamma_{\text{S1}}\Gamma_{\text{S2}} \varrho_{\text{QD2}}(\zeta) f_2(\zeta), \quad (7.6)$$

where  $\varrho_{\text{QD2}}(E)$  is the spectral density of QD2 and  $f_2(E)$  is the Fermi function of the lead N2. The rate  $t_{n\ell}^-$  can be obtained by the following replacements:  $d_\sigma \leftrightarrow d_{\bar{\sigma}}^\dagger$ ,  $\zeta \rightarrow -\zeta$  and  $f_2 \rightarrow 1 - f_2$ . The probabilities for CPS and elastic co-tunnelling scale with a geometry depended pre-factor  $k_{\text{CPS}}$  and  $k_{\text{EC}}$ .

It is generally assumed that the non-local tunnelling processes originate from the wire segment below S, which is turned superconducting by the proximity effect, and not from the bulk S [63, 69, 88]. This is concluded from the fact that non-local tunnelling through the bulk of S is suppressed by factor  $(k_{\text{F}}\delta r)^{-2}$  [83, 84], where  $k_{\text{F}}^{-1} \sim \text{\AA}$  is the Fermi wavevector in S and  $\delta r$  is the separation between the QDs. The non-local transport rates reported in Refs. [63–66, 148] are way larger than compatible with the suppression term  $(k_{\text{F}}\delta r)^{-2}$ . This term arises from a summation over different paths in S. It is therefore not present in 1-dimensional superconductors, for which one expects probability amplitudes on the order of

$$k_{\text{CPS}} \sim k_{\text{EC}} \sim e^{-\delta r/\pi\xi^*} \quad (7.7)$$

in the ballistic limit [69, 91].  $\xi^* = \hbar v_{\text{F}}/\pi\Delta^* \approx 340 \text{ nm}$  is the coherence length that corresponds to the induced gap  $\Delta^*$  in the CNT, where the Fermi velocity is  $v_{\text{F}} = 8.1 \cdot 10^5 \text{ m/s}$  [152]. The exponential function ensures that non-local tunnelling can only take place over distances on the order of the superconducting coherence length. However, the estimated coherence length  $\xi^*$  is larger than the dot separation. Thus we expect that the non-local current is mostly limited by the rate of the competing first order process  $t_r^+$  and not by the geometry of the device. We emphasize that for the devices investigated in Refs. [63, 65, 84] elastic co-tunnelling could be neglected not because the probability amplitude  $k_{\text{EC}}$  was small, but because of the vanishing occupation probability of the QDs ( $P_{\text{QDi}} \approx 0$ ) that is implied by the coupling asymmetry  $\Gamma_{\text{Si}} \ll \Gamma_{\text{Ni}}$ .

## 7.3.2. Model results and comparison with experiment

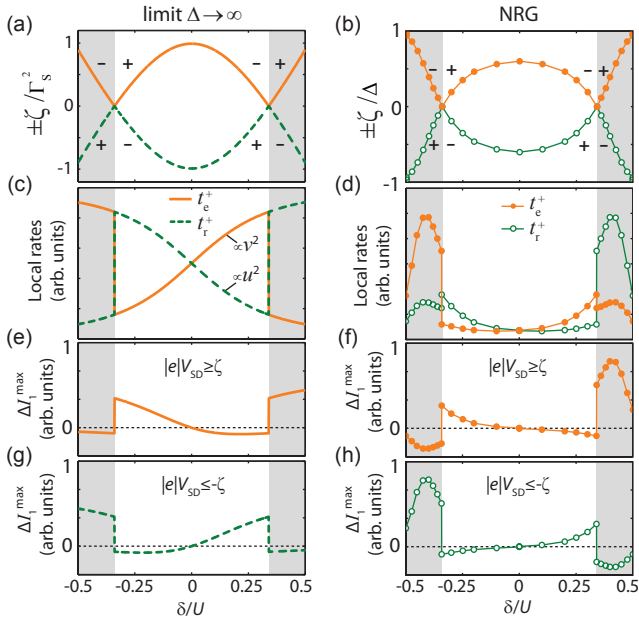


**Figure 7.7.:** Model for non-local signals calculated in the limit  $\Delta \rightarrow \infty$  for  $\Gamma_{S1} = 0.37$  (left column) and based on NRG results for the parameters  $U = 1$ ,  $\Delta = 0.01$  and  $U/\pi\Gamma_S = 5$  extracted from reference [96] (right column). The QD energy is parametrized by  $\delta = \epsilon_d + U/2$ . The grey shaded regions indicate the  $|-\rangle$  GS. (a,b) Dispersion of the Andreev resonances. The plus and minus symbols denote the sign of the non-local current in the respective region. (c,d) Local rates for  $|e|V_{SD} \geq \zeta$ . (e,f) Non-local current  $\Delta I_1$  for  $|e|V_{SD} \geq \zeta$  and (g,h) for  $|e|V_{SD} \leq -\zeta$ .

In Fig. 7.7(e,g) we plot the gate evolution of the maximum non-local current for positive and negative bias, calculated from Eq. (7.3) with the assumption  $k_{EC} = k_{CPS}$ . Despite the oversimplification  $\Delta \rightarrow \infty$  the model captures the main features of our experimental findings. The sign of the non-local current alternates in the same order as in the experiment (see Fig. 7.5), going through two sharp transitions and one smooth transition.

The sharp reversal of  $\Delta I_1$  is the signature of the GS transition, in which the rates  $t_e$  and  $t_r$  are inverted. In the experiment this transition is smeared out by the broadening of the Andreev resonance not considered in our model. In the doublet GS the non-local conductance changes gradually from positive to negative values, owing to the gate evolution of the BdG amplitudes. As

the dot energy is increased the weight of the  $|-\rangle$  state is shifted from the  $|0\rangle$ -term to the  $|\uparrow\downarrow\rangle$ -term, thereby gradually moving the average location of the two electron charges confined in the ABS from the superconductor to the QD. This continuous change of the BdG amplitudes leads to a smooth reversal of the non-local current at the electron-hole (e-h) symmetry point ( $\delta = 0$ ), where  $t_e = t_r$ .

In case of a finite superconducting gap exchange interactions between the  $|\sigma\rangle$  state and quasiparticles can lead to a spin screening of the  $|\sigma\rangle$  state. This Kondo effect complicates the theoretical treatment of the problem. The wavefunction of the doublet state acquires a singlet admixture and the dispersion relation of the Andreev resonances, as well as the transport rates become renormalised. An analytical solution of the problem is not possible, but the numerical renormalization group method (NRG) provides a reliable approach to calculate the QD spectral densities [88].

In the right column of Fig. 7.7 we test our model with NRG results calculated in reference [96] for the parameters  $U = 1$ ,  $\Delta = 0.01$  and  $U/\pi\Gamma_S = 5$ . The dispersion of the Andreev resonances for these parameters, shown in Fig. 7.7(b), resemble our experiment. The local transport rates, plotted in Fig. 7.7(d), are given by the spectral weight of the respective Andreev resonance. To calculate the non-local current we assume again  $k_{\text{CPS}} = k_{\text{EC}}$ . Figure 7.7(f,h) shows that the qualitative behaviour of the non-local signal is altered only marginally when interactions with quasiparticles are considered. The main effect of the finite gap on our model originates from a suppression of the local transport rates when the Andreev resonance approaches the gap edge, i.e.  $t_{e/r} \rightarrow 0$  for  $\zeta \rightarrow \Delta$ . This leads to a cut-off of the non-local signal at the ends of the inspected gate range ( $\delta = \pm 0.5$ ) and a more rapid decay towards the e-h symmetry point compared to the  $\Delta \rightarrow \infty$  case. Both of these modifications in the line shape of the non-local signal improve the agreement with our experimental findings in Fig. 7.5.

## 7.4. Discussion and Conclusion

We experimentally investigated a CNT QD, strongly coupled to a superconducting niobium lead. By local transport spectroscopy through a normal conducting tunnel probe we could resolve individual ABSs in the excitation spectrum of the QD-S system. A second QD, coupled parallel to the same S-contact, allowed to excite these ABSs also by non-local processes, namely CPS and elastic co-tunnelling. We found appreciable non-local correlations in the conductance through both QDs. These non-local signals change sign with reversed bias and exhibit a complex gate dependence with a sign change at the GS transition and a sign change when the e-h symmet-

ric point is crossed. We qualitatively explain this rich behaviour in a simple rate equation model.

In our model, the sign of the non-local current is determined by the asymmetry between the local excitation and relaxation rates. In the limit  $\Delta \rightarrow \infty$ , this asymmetry is given by the difference of the BdG amplitudes,  $\gamma(v^2 - u^2)$ , where the pre-factor  $\gamma = \pm 1$  changes sign when the GS or the bias direction changes. One can ascribe a physical meaning to this term by rewriting it as  $2v^2 - 1$ , using the normalization condition  $u^2 + v^2 = 1$ . Multiplying with the electron charge, this corresponds to the charge difference between ES and GS,

$$\Delta Q = Q_{\text{ES}} - Q_{\text{GS}}, \quad (7.8)$$

where the average on-site charge in the  $|-\rangle$  state is given by the expectation value of the number operator,  $Q_- = e \langle - | \sum_{\sigma} d_{\sigma}^{\dagger} d_{\sigma} | - \rangle = 2e v^2$ . The QD charge in the doublet state is  $Q_{\sigma} = 1e$ .

While local spectroscopy measures the energy difference between the ES and the GS,  $\zeta = E_{\text{ES}} - E_{\text{GS}}$ , the non-local signals provide a spectroscopic tool to investigate the charge difference between both states. However, a quantitative determination of  $\Delta Q$  is hindered by the lack of knowledge about  $t_{nl}$ . Still we are able to *qualitatively* follow the gate evolution of  $\Delta Q$ , which is a direct witness of the competition between repulsive Coulomb interactions and the superconducting pairing, associated with an attractive electron-electron interaction.

The  $|-\rangle$  state, being subject to quantum fluctuations of the charge, allows continuous changes of the mean QD charge. We were able to indirectly observe this gradual charging of the ABS by following the smooth crossover from a positive to a negative non-local signal when the QD is in the doublet GS. When  $\Delta Q$  becomes negative, the QD holds more charge in the GS than in the first ES – a situation that can only occur in the presence of attractive interactions. At the GS transition, which is identified by the continuous crossing of the two Andreev resonances in local spectroscopy, the sign of  $\Delta Q$  is inverted. The resulting abrupt reversal of the non-local current constitutes a novel experimental probe of the discontinuity characteristic for such quantum phase transitions.

In conclusion, we established a new spectroscopy method to study ABSs in QDs. Our method complements local tunnelling spectroscopy and provides access to the qualitative evolution of the BdG amplitudes, yielding a novel experimental view on the superconducting proximity effect in QDs.

## Summary and outlook

In this thesis we studied a special type of carbon nanotube (CNT) based double quantum dot (QD) devices. The two QDs, QD1 and QD2, are connected to a common superconducting electrode (S), but otherwise well decoupled from each other. Each of the QDs is connected to a normal metal drain N1 and N2. Devices with such a geometry are commonly referred to as Cooper pair splitters. However, whether, and how well, such devices actually split Cooper pairs is mostly determined by geometry independent factors, such as the coupling constants,  $\Gamma_{Si}$ ,  $\Gamma_{Ni}$  ( $i = 1, 2$ ) and  $\Gamma_{12}$ , as well as the superconducting energy gap  $\Delta$ .

In Chapter 6 we presented a device that marks so far the best performing Cooper pair splitter, benchmarked in terms of splitting efficiency. In the context of the visionary experiments by Hofstetter *et al.* [63] and Herrmann *et al.* [64] our work must be seen as a second generation experiment. It was published only one month before Das *et al.* [65] demonstrated CPS by noise cross-correlation measurements in a InAs nanowire device. The logical next step for traditional Cooper pair splitting experiments is the implementation of spin sensitive measurements. Ferromagnetic contacts are one option for this purpose, but they are hard to control [112] and in the end the achievable spin polarizations might be too low for a Bell test [153]. Alternatively, the QD itself can be used as spin filter by means of the Zeeman effect. For this approach, a spin splitting of the QD levels must be induced by an external magnetic field without quenching the superconductor. In Chapter 7 we reported non-local signals in external magnetic fields up to 500 mT, a field strength that is already sufficient to resolve Zeeman splitting

in weakly coupled CNT QDs. Thus, niobium contacted CNTs bear a great prospects as spin sensitive Cooper pair splitters. In this context, the spin-orbit interactions in CNT QDs might provide a neat advantage over InAs based QDs, which excel with a larger  $g$ -factor. It was shown that a Bell test can be implemented in Cooper pair splitters which are fabricated from bent CNTs [154]. The proposed scheme requires no noise measurements and supports imperfect splitting efficiency and disorder. In a simplified picture, the spin-orbit interactions enhance the magnetic field along the CNT axis. Bent tubes allow therefore to perform non-collinear spin projections, a key ingredient of any Bell test. This spin-orbit induced  $g$ -factor anisotropy was already exploited in recent experiments with bent nanotubes [121, 155].

In Chapter 7 we investigated Cooper pair splitter device in the "wrong" coupling regime. Superconducting correlations leaked onto QD1, as a result of a too strong coupling between QD1 and S. This led to the formation of Andreev bound states (ABSs). The ABS adds a local first order transport channel and the respective QD is no longer a good filter to enforce CPS. However, ABSs are a very interesting topic in their own right. They are characterised by their energy and by two Bogoliubov-de Gennes amplitudes. Previous studies mostly focused on the energy dispersion of these states [56, 70–73, 101]. By means of non-local conductance measurements we could also probe the Bogoliubov-de Gennes amplitudes, albeit only in a qualitative manner.

To further study the interplay between ABSs and CPSs it would be very interesting to realize a Cooper pair splitter where both QDs are coupled strongly to S, but weakly to N1 and N2. In such a device a state that we nicknamed the *Andreev molecule* could form. One may first consider a conventional double QD, where the a tunnel coupling between the two charge states (1,0) and (0,1) gives rise to a molecular state. If the two QDs are coupled via a superconductor, then crossed Andreev reflections mix the charge states (1,1) and (0,0). This can also lead to a molecular state – the *Andreev molecule*. Such systems have recently been topic of interesting proposals which predicted the existence of a so-called triplet blockade [87], the existence of so-called "poor man's Majorana bound states" [68] and the possibility to non-locally couple spin qubits [69].

## Bibliography

- [1] R. P. Feynman, *Simulating physics with computers*, [Int. J. Theor. Phys.](#) **21**, 471 (1982).
- [2] A. Einstein, B. Podolsky, and N. Rosen, *Can quantum-mechanical description of physical reality be considered complete?*, [Phys. Rev.](#) **47**, 777 (1935).
- [3] N. David Mermin, *Is the moon there when nobody looks? Reality and the quantum theory*, [Physics Today](#) **38**, 38 (1985).
- [4] N. Bohr, *Can quantum-mechanical description of physical reality be considered complete?*, [Phys. Rev.](#) **48**, 696 (1935).
- [5] J. S. Bell, *On the Einstein Podolsky Rosen Paradox*, [Physics](#) **1**, 195 (1964).
- [6] A. Aspect, P. Grangier, and G. Roger, *Experimental realization of Einstein-Podolsky-Rosen-Bohm Gedankenexperiment: A new violation of Bell's inequalities*, [Phys. Rev. Lett.](#) **49**, 91 (1982).
- [7] M. A. Rowe, D. Kielpinski, V. Meyer, C. A. Sackett, W. M. Itano, C. Monroe, and D. J. Wineland, *Experimental violation of a Bell's inequality with efficient detection*, [Nature](#) **409**, 791 (2001).

- [8] M. Ansmann, H. Wang, R. C. Bialczak, M. Hofheinz, E. Lucero, M. Neeley, A. D. O’Connell, D. Sank, M. Weides, J. Wenner, A. N. Cleland, and J. M. Martinis, *Violation of Bell’s inequality in josephson phase qubits*, *Nature* **461**, 504 (2009).
- [9] R. Ursin, F. Tiefenbacher, T. Schmitt-Manderbach, H. Weier, T. Scheidl, M. Lindenthal, B. Blauensteiner, T. Jennewein, J. Perdigues, P. Trojek, B. Omer, M. Furst, M. Meyenburg, J. Rarity, Z. Sodnik, C. Barbieri, H. Weinfurter, and A. Zeilinger, *Entanglement-based quantum communication over 144 km*, *Nat. Phys* **3**, 481 (2007).
- [10] A. K. Ekert, *Quantum cryptography based on Bell’s theorem*, *Phys. Rev. Lett.* **67**, 661 (1991).
- [11] C. H. Bennett, G. Brassard, C. Crépeau, R. Jozsa, A. Peres, and W. K. Wootters, *Teleporting an unknown quantum state via dual classical and Einstein-Podolsky-Rosen channels*, *Phys. Rev. Lett.* **70**, 1895 (1993).
- [12] D. Loss and D. P. DiVincenzo, *Quantum computation with quantum dots*, *Phys. Rev. A* **57**, 120 (1998).
- [13] A. Steane, *Quantum computing*, *Reports on Progress in Physics* **61**, 117 (1998).
- [14] G. Vidal, *Efficient classical simulation of slightly entangled quantum computations*, *Phys. Rev. Lett.* **91**, 147902 (2003).
- [15] L. P. Kouwenhoven, D. G. Austing, and S. Tarucha, *Few-electron quantum dots*, *Reports on Progress in Physics* **64**, 701 (2001).
- [16] A. K. Geim and K. S. Novoselov, *The rise of graphene*, *Nat. Mater.* **6**, 183 (2007).
- [17] C. Schönberger, *Charge and spin transport in carbon nanotubes*, *Semiconductor Science and Technology* **21**, S1 (2006).
- [18] P. R. Wallace, *The band theory of graphite*, *Phys. Rev.* **71**, 622 (1947).
- [19] J.-C. Charlier, X. Blase, and S. Roche, *Electronic and transport properties of nanotubes*, *Rev. Mod. Phys.* **79**, 677 (2007).
- [20] D. J. Wales, M. A. Miller, and T. R. Walsh, *Archetypal energy landscapes*, *Nature* **394**, 758 (1998).

- 
- [21] C. Schönenberger, *Bandstructure of graphene and carbon nanotubes : An exercise in condensed matter physics*, Lecture notes (2000), online available: <http://www.nanoelectronics.ch/education/Nanotubes/cnt.php>.
- [22] S. G. Lemay, J. W. Janssen, M. van den Hout, M. Mooij, M. J. Bronikowski, P. A. Willis, R. E. Smalley, L. P. Kouwenhoven, and C. Dekker, *Two-dimensional imaging of electronic wavefunctions in carbon nanotubes*, *Nature* **412**, 617 (2001).
- [23] J. Svensson and E. E. B. Campbell, *Schottky barriers in carbon nanotube-metal contacts*, *Journal of Applied Physics* **110**, 111101 (2011).
- [24] S. Ilani and P. L. McEuen, *Electron transport in carbon nanotubes*, *Annual Review of Condensed Matter Physics* **1**, 1 (2010).
- [25] J. W. G. Wilder, L. C. Venema, A. G. Rinzler, R. E. Smalley, and C. Dekker, *Electronic structure of atomically resolved carbon nanotubes*, *Nature* **391**, 59 (1998).
- [26] C. Zhou, J. Kong, and H. Dai, *Intrinsic electrical properties of individual single-walled carbon nanotubes with small band gaps*, *Phys. Rev. Lett.* **84**, 5604 (2000).
- [27] V. V. Deshpande, B. Chandra, R. Caldwell, D. S. Novikov, J. Hone, and M. Bockrath, *Mott insulating state in ultraclean carbon nanotubes*, *Science* **323**, 106 (2009).
- [28] W. Mönch, *On the physics of metal-semiconductor interfaces*, *Reports on Progress in Physics* **53**, 221 (1990).
- [29] F. m. c. Léonard and J. Tersoff, *Role of fermi-level pinning in nanotube schottky diodes*, *Phys. Rev. Lett.* **84**, 4693 (2000).
- [30] F. m. c. Léonard and A. A. Talin, *Size-dependent effects on electrical contacts to nanotubes and nanowires*, *Phys. Rev. Lett.* **97**, 026804 (2006).
- [31] S. Suzuki, C. Bower, Y. Watanabe, and O. Zhou, *Work functions and valence band states of pristine and cs-intercalated single-walled carbon nanotube bundles*, *Applied Physics Letters* **76**, 4007 (2000).
- [32] X. Cui, M. Freitag, R. Martel, L. Brus, and P. Avouris, *Controlling energy-level alignments at carbon nanotube/au contacts*, *Nano Letters* **3**, 783 (2003).

- [33] Z. Chen, J. Appenzeller, J. Knoch, Y.-m. Lin, and P. Avouris, *The role of metal–nanotube contact in the performance of carbon nanotube field-effect transistors*, *Nano Letters* **5**, 1497 (2005).
- [34] M. Jung, J. Schindele, S. Nau, M. Weiss, A. Baumgartner, and C. Schönenberger, *Ultraclean single, double, and triple carbon nanotube quantum dots with recessed Re bottom gates*, *Nano Letters* **13**, 4522 (2013).
- [35] S. Heinze, J. Tersoff, R. Martel, V. Derycke, J. Appenzeller, and P. Avouris, *Carbon nanotubes as schottky barrier transistors*, *Phys. Rev. Lett.* **89**, 106801 (2002).
- [36] A. Javey, J. Guo, Q. Wang, M. Lundstrom, and H. Dai, *Ballistic carbon nanotube field-effect transistors*, *Nature* **424**, 654 (2003).
- [37] W. Kim, A. Javey, R. Tu, J. Cao, Q. Wang, and H. Dai, *Electrical contacts to carbon nanotubes down to 1nm in diameter*, *Applied Physics Letters* **87**, 173101 (2005).
- [38] Z. Zhang, X. Liang, S. Wang, K. Yao, Y. Hu, Y. Zhu, Q. Chen, W. Zhou, Y. Li, Y. Yao, J. Zhang, and L.-M. Peng, *Doping-free fabrication of carbon nanotube based ballistic cmos devices and circuits*, *Nano Letters* **7**, 3603 (2007).
- [39] L. Ding, S. Wang, Z. Zhang, Q. Zeng, Z. Wang, T. Pei, L. Yang, X. Liang, J. Shen, Q. Chen, R. Cui, Y. Li, and L.-M. Peng, *Y-contacted high-performance n-type single-walled carbon nanotube field-effect transistors: Scaling and comparison with sc-contacted devices*, *Nano Letters* **9**, 4209 (2009), pMID: 19995085.
- [40] *Tables of physical & chemical constants*, Kaye & Laby Online, version 1.0 (2005), online available: <http://www.kayelaby.npl.co.uk/>.
- [41] V. Derycke, R. Martel, J. Appenzeller, and P. Avouris, *Controlling doping and carrier injection in carbon nanotube transistors*, *Applied Physics Letters* **80**, 2773 (2002).
- [42] Y.-F. Chen and M. S. Fuhrer, *Tuning from thermionic emission to ohmic tunnel contacts via doping in schottky-barrier nanotube transistors*, *Nano Letters* **6**, 2158 (2006).
- [43] T. Meng, C.-Y. Wang, and S.-Y. Wang, *First-principles study of contact between ti surface and semiconducting carbon nanotube*, *Journal of Applied Physics* **102**, 013709 (2007).

- [44] J. J. Palacios, P. Tarakeshwar, and D. M. Kim, *Metal contacts in carbon nanotube field-effect transistors: Beyond the schottky barrier paradigm*, *Phys. Rev. B* **77**, 113403 (2008).
- [45] V. Vitale, A. Curioni, and W. Andreoni, *Metal-carbon nanotube contacts: The link between schottky barrier and chemical bonding*, *J. Am. Chem. Soc.* **130**, 5848 (2008).
- [46] W. Zhu and E. Kaxiras, *Schottky barrier formation at a carbon nanotube-metal junction*, *Applied Physics Letters* **89**, 243107 (2006).
- [47] W. Zhu and E. Kaxiras, *The nature of contact between pd leads and semiconducting carbon nanotubes*, *Nano Letters* **6**, 1415 (2006).
- [48] I. Suarez-Martinez, C. P. Ewels, X. Ke, G. Van Tendeloo, S. Thies, W. Drube, A. Felten, J.-J. Pireaux, J. Ghijsen, and C. Bittencourt, *Study of the interface between rhodium and carbon nanotubes*, *ACS Nano* **4**, 1680 (2010).
- [49] A. D. Franklin and Z. Chen, *Length scaling of carbon nanotube transistors*, *Nat. Nano* **5**, 858 (2010).
- [50] B. Babić and C. Schönenberger, *Observation of fano resonances in single-wall carbon nanotubes*, *Phys. Rev. B* **70**, 195408 (2004).
- [51] R. Hanson, L. P. Kouwenhoven, J. R. Petta, S. Tarucha, and L. M. K. Vandersypen, *Spins in few-electron quantum dots*, *Rev. Mod. Phys.* **79**, 1217 (2007).
- [52] C. W. J. Beenakker, *Theory of coulomb-blockade oscillations in the conductance of a quantum dot*, *Phys. Rev. B* **44**, 1646 (1991).
- [53] J. Paaske, *Cotunnelling and kondo effect in quantum dots*, Lecture notes (2010), published online: [http://www.thp.uni-due.de/~koenig/DPG\\_School\\_10/index.html](http://www.thp.uni-due.de/~koenig/DPG_School_10/index.html).
- [54] S. De Franceschi, S. Sasaki, J. M. Elzerman, W. G. van der Wiel, S. Tarucha, and L. P. Kouwenhoven, *Electron cotunneling in a semiconductor quantum dot*, *Phys. Rev. Lett.* **86**, 878 (2001).
- [55] A. Martín-Rodero and A. Levy Yeyati, *Josephson and andreev transport through quantum dots*, *Advances in Physics*, *Advances in Physics* **60**, 899 (2011).

- [56] J.-D. Pillet, C. H. L. Quay, P. Morfin, C. Bena, a. L. Yeyati, and P. Joyez, *Andreev bound states in supercurrent-carrying carbon nanotubes revealed*, *Nat. Phys.* **6**, 965 (2010).
- [57] W. Chang, V. E. Manucharyan, T. S. Jespersen, J. Nygård, and C. M. Marcus, *Tunneling spectroscopy of quasiparticle bound states in a spinful josephson junction*, *Phys. Rev. Lett.* **110**, 217005 (2013).
- [58] V. Mourik, K. Zuo, S. M. Frolov, S. R. Plissard, E. P. A. M. Bakkers, and L. P. Kouwenhoven, *Signatures of Majorana fermions in hybrid superconductor-semiconductor nanowire devices*, *Science* **336**, 1003 (2012).
- [59] A. Das, Y. Ronen, Y. Most, Y. Oreg, M. Heiblum, and H. Shtrikman, *Zero-bias peaks and splitting in an al-inas nanowire topological superconductor as a signature of Majorana fermions*, *Nat. Phys.* **8**, 887 (2012).
- [60] P. Jarillo-Herrero, J. A. van Dam, and L. P. Kouwenhoven, *Quantum supercurrent transistors in carbon nanotubes*, *Nature* **439**, 953 (2006).
- [61] J.-P. Cleuziou, W. Wernsdorfer, V. Bouchiat, T. Ondarcuhu, and M. Monthieux, *Carbon nanotube superconducting quantum interference device*, *Nat. Nano.* **1**, 53 (2006).
- [62] R. Maurand, T. Meng, E. Bonet, S. Florens, L. Marty, and W. Wernsdorfer, *First-Order  $0-\pi$  Quantum Phase Transition in the Kondo Regime of a Superconducting Carbon-Nanotube Quantum Dot*, *Physical Review X* **2**, 011009 (2012).
- [63] L. Hofstetter, S. Csonka, J. Nygård, and C. Schönberger, *Cooper pair splitter realized in a two-quantum-dot Y-junction*, *Nature* **461**, 960 (2009).
- [64] L. G. Herrmann, F. Portier, P. Roche, A. L. Yeyati, T. Kontos, and C. Strunk, *Carbon nanotubes as Cooper-pair beam splitters*, *Phys. Rev. Lett.* **104**, 026801 (2010).
- [65] A. Das, Y. Ronen, M. Heiblum, D. Mahalu, A. V. Kretinin, and H. Shtrikman, *High-efficiency Cooper pair splitting demonstrated by two-particle conductance resonance and positive noise cross-correlation*, *Nat. Commun.* **3**, 1165 (2012).
- [66] J. Schindele, A. Baumgartner, and C. Schönberger, *Near-unity Cooper pair splitting efficiency*, *Phys. Rev. Lett.* **109**, 157002 (2012).

- 
- [67] A. Cottet, T. Kontos, and A. L. Yeyati, *Subradiant split Cooper pairs*, *Phys. Rev. Lett.* **108**, 166803 (2012).
- [68] M. Leijnse and K. Flensberg, *Parity qubits and poor man's Majorana bound states in double quantum dots*, *Phys. Rev. B* **86**, 134528 (2012).
- [69] M. Leijnse and K. Flensberg, *Coupling spin qubits via superconductors*, *Phys. Rev. Lett.* **111**, 060501 (2013).
- [70] T. Dirks, T. Hughes, S. Lal, B. Uchoa, Y.-F. Chen, C. Chialvo, P. Goldbart, and N. Mason, *Nat. Phys.* **7**, 386v1 (2011).
- [71] J.-D. Pillet, P. Joyez, R. Žitko, and M. F. Goffman, *Tunneling spectroscopy of a single quantum dot coupled to a superconductor: From kondo ridge to andreev bound states*, *Phys. Rev. B* **88**, 045101 (2013).
- [72] E. J. H. Lee, X. Jiang, M. Houzet, R. Aguado, C. M. Lieber, and S. De Franceschi, *Spin-resolved andreev levels and parity crossings in hybrid superconductor-semiconductor nanostructures*, *Nat Nano* **9**, 79 (2014).
- [73] A. Kumar, M. Gaim, D. Steininger, A. Levy Yeyati, A. Martín-Rodero, A. K. Hüttel, and C. Strunk, *Temperature dependence of andreev spectra in a superconducting carbon nanotube quantum dot*, arXiv:1308.1020 (2013).
- [74] C. W. J. Beenakker, *Three "universal" mesoscopic Josephson effects*, in *Transport Phenomena in Mesoscopic Systems*, edited by H. Fukuyama and T. Ando (Springer, 2012).
- [75] M. Tinkham, *Introduction to superconductivity* (Dover Publications, inc., 2004).
- [76] S. Hunklinger, *Festkörperphysik* (Oldenbourg, 2007).
- [77] K. H. Onnes, *Leiden Commun.* **124c** (1911).
- [78] W. Meissner and R. Ochsenfeld, *Ein neuer Effekt bei Eintritt der Supraleitfähigkeit*, *Naturwissenschaften* **21**, 787 (1933).
- [79] J. Bardeen, L. N. Cooper, and J. R. Schrieffer, *Theory of superconductivity*, *Phys. Rev.* **108**, 1175 (1957).
- [80] L. N. Cooper, *Bound electron pairs in a degenerate fermi gas*, *Phys. Rev.* **104**, 1189 (1956).

- [81] C. W. J. Beenakker, *Why does a metal-superconductor junction have a resistance?*, [arXiv:cond-mat/9909293](#) (1999).
- [82] B. Pannetier and H. Courtois, *Andreev reflection and proximity effect*, [Journal of Low Temperature Physics](#) **118**, 599 (2000).
- [83] G. Falci, D. Feinberg, and F. W. J. Hekking, *Correlated tunneling into a superconductor in a multiprobe hybrid structure*, [Europhys. Lett.](#) **54**, 255 (2001).
- [84] P. Recher, E. V. Sukhorukov, and D. Loss, *Andreev tunneling, coulomb blockade, and resonant transport of nonlocal spin-entangled electrons*, [Phys. Rev. B](#) **63**, 165314 (2001).
- [85] L. Hofstetter, *Hybrid Quantum Dots in InAs Nanowires*, [Ph.D. thesis](#), University of Basel (2011).
- [86] O. Sauret, D. Feinberg, and T. Martin, *Quantum master equations for the superconductor quantum dot entangler*, [Phys. Rev. B](#) **70**, 245313 (2004).
- [87] J. Eldridge, M. G. Pala, M. Governale, and J. König, *Superconducting proximity effect in interacting double-dot systems*, [Phys. Rev. B](#) **82**, 184507 (2010).
- [88] P. Buset, W. J. Herrera, and A. L. Yeyati, *Microscopic theory of Cooper pair beam splitters based on carbon nanotubes*, [Phys. Rev. B](#) **84**, 115448 (2011).
- [89] M. R. Gräber, W. A. Coish, C. Hoffmann, M. Weiss, J. Furer, S. Oberholzer, D. Loss, and C. Schönenberger, *Molecular states in carbon nanotube double quantum dots*, [Phys. Rev. B](#) **74**, 075427 (2006).
- [90] P. Samuelsson and M. Büttiker, *Semiclassical theory of current correlations in chaotic dot-superconductor systems*, [Phys. Rev. B](#) **66**, 201306 (2002).
- [91] D. Feinberg, *Andreev scattering and cotunneling between two superconductor-normal metal interfaces: the dirty limit*, [The European Physical Journal B - Condensed Matter and Complex Systems](#) **36**, 419 (2003).
- [92] P. Recher, D. Saraga, and D. Loss, *Creation and detection of mobile and non-local spin-entangled electrons*, in [Fundamental Problems of Mesoscopic Physics](#), NATO Science Series II: Mathematics, Physics

- and Chemistry, Vol. 154, edited by I. Lerner, B. Altshuler, and Y. Gefen (Springer Netherlands, 2004) pp. 179–202.
- [93] M. S. Kalenkov and A. D. Zaikin, *Nonlocal andreev reflection at high transmissions*, *Phys. Rev. B* **75**, 172503 (2007).
- [94] D. S. Golubev, M. S. Kalenkov, and A. D. Zaikin, *Crossed andreev reflection and charge imbalance in diffusive normal-superconducting-normal structures*, *Phys. Rev. Lett.* **103**, 067006 (2009).
- [95] T. Meng, S. Florens, and P. Simon, *Self-consistent description of andreev bound states in josephson quantum dot devices*, *Phys. Rev. B* **79**, 224521 (2009).
- [96] J. Bauer, A. Oguri, and A. Hewson, *Spectral properties of locally correlated electrons in a Bardeen-Cooper-Schrieffer superconductor*, *J. Phys.: Cond. Matter* **19**, 486211 (2007).
- [97] A. Braggio, M. Governale, M. G. Pala, and J. König, *Superconducting proximity effect in interacting quantum dots revealed by shot noise*, *Solid State Communications* **151**, 155 (2011).
- [98] A. Martín-Rodero and A. L. Yeyati, *The andreev states of a superconducting quantum dot: mean field versus exact numerical results*, *Journal of Physics: Condensed Matter* **24**, 385303 (2012).
- [99] D. Futterer, J. Swiebodzinski, M. Governale, and J. König, *Renormalization effects in interacting quantum dots coupled to superconducting leads*, *Phys. Rev. B* **87**, 014509 (2013).
- [100] L. Bretheau, C. O. Girit, H. Pothier, D. Esteve, and C. Urbina, *Exciting andreev pairs in a superconducting atomic contact*, *Nature* **499**, 312 (2013).
- [101] R. S. Deacon, Y. Tanaka, A. Oiwa, R. Sakano, K. Yoshida, K. Shibata, K. Hirakawa, and S. Tarucha, *Tunneling spectroscopy of andreev energy levels in a quantum dot coupled to a superconductor*, *Phys. Rev. Lett.* **104**, 076805 (2010).
- [102] J. Kong, H. T. Soh, A. M. Cassell, C. F. Quate, and H. Dai, *Synthesis of individual single-walled carbon nanotubes on patterned silicon wafers*, *Nature* **395**, 878 (1998).
- [103] J. Furer, *Growth of Single-Wall Carbon Nanotubes by Chemical Vapor Deposition for Electrical Devices*, *Ph.D. thesis*, University of Basel (2006).

- [104] B. Babić, J. Furer, M. Iqbal, and C. Schönenberger, *Suitability of carbon nanotubes grown by chemical vapor deposition for electrical devices*, [AIP Conference Proceedings](#) **723**, 574 (2004).
- [105] S. Naha and I. K. Puri, *A model for catalytic growth of carbon nanotubes*, [Journal of Physics D: Applied Physics](#) **41**, 065304 (2008).
- [106] T. Brintlinger, Y.-F. Chen, T. Dürkop, E. Cobas, M. S. Fuhrer, J. D. Barry, and J. Melngailis, *Rapid imaging of nanotubes on insulating substrates*, [Applied Physics Letters](#) **81**, 2454 (2002).
- [107] D. S. Macintyre, O. Ignatova, S. Thoms, and I. G. Thayne, *Resist residues and transistor gate fabrication*, [J. Vac. Sci. Technol. B](#) **27**, 2597 (2009).
- [108] I. Maximov, A. A. Zakharov, T. Holmqvist, L. Montelius, and I. Lindau, *Investigation of polymethylmethacrylate resist residues using photoelectron microscopy*, [Journal of Vacuum Science & Technology B](#) **20**, 1139 (2002).
- [109] H. Aurich, *Carbon nanotube spin-valve with optimized ferromagnetic contacts*, [Ph.D. thesis](#), University of Basel (2012).
- [110] W. W. Hu, K. Sarveswaran, M. Lieberman, and G. Bernstein, *Sub-10 nm electron beam lithography using cold development of poly(methylmethacrylate)*, [J. Vac. Sci. Technol. B](#) **22**, 1711 (2004).
- [111] J. S. Wi and K. B. Kim, *Enhanced development properties of IPA (isopropyl alcohol) on the PMMA electron beam resist*, [Electronic Materials Letters](#) **3**, 1 (2007).
- [112] J. Samm, J. Gramich, A. Baumgartner, M. Weiss, and C. Schönenberger, *Fabrication and characterisation of nanospintronic devices*, [arXiv:1312.0159](#) (2013).
- [113] T. Yamaguchi, K. Yamazaki, and H. Namatsu, *Influence of molecular weight of resist polymers on surface roughness and line-edge roughness*, [Journal of Vacuum Science & Technology B](#) **22**, 2604 (2004).
- [114] C. Enss and S. Hunklinger, *Low-Temperature Physics* (Springer, 2005).
- [115] H. Bluhm and K. A. Moler, *Dissipative cryogenic filters with zero dc resistance*, [Review of Scientific Instruments](#) **79**, 014703 (2008).

- [116] F. Kuemmeth, S. Ilani, D. C. Ralph, and P. L. McEuen, *Coupling of spin and orbital motion of electrons in carbon nanotubes*, [Nature](#) **452**, 448 (2008).
- [117] V. V. Deshpande and M. Bockrath, *The one-dimensional wigner crystal in carbon nanotubes*, [Nat. Phys.](#) **4**, 314 (2008).
- [118] S. Pecker, F. Kuemmeth, A. Secchi, M. Rontani, D. C. Ralph, P. L. McEuen, and S. Ilani, *Observation and spectroscopy of a two-electron wigner molecule in an ultraclean carbon nanotube*, [Nat. Phys.](#) **9**, 576 (2013).
- [119] G. A. Steele, G. Gotz, and L. P. Kouwenhoven, *Tunable few-electron double quantum dots and klein tunnelling in ultraclean carbon nanotubes*, [Nat. Nano](#) **4**, 363 (2009).
- [120] F. Pei, E. A. Laird, G. A. Steele, and L. P. Kouwenhoven, *Valley-spin blockade and spin resonance in carbon nanotubes*, [Nat. Nano](#) **7**, 630 (2012).
- [121] E. A. Laird, F. Pei, and L. P. Kouwenhoven, *A valley-spin qubit in a carbon nanotube*, [Nat Nano](#) **8**, 565 (2013).
- [122] J. Cao, Q. Wang, and H. Dai, *Electron transport in very clean, as-grown suspended carbon nanotubes*, [Nat Mater](#) **4**, 745 (2005).
- [123] J. Waissman, M. Honig, S. Pecker, A. Benyamini, A. Hamo, and S. Ilani, *Realization of pristine and locally tunable one-dimensional electron systems in carbon nanotubes*, [Nat. Nano.](#) **8**, 569 (2013).
- [124] S. Nau, *As-grown Carbon Nanotubes with Superconducting Contacts*, [Ph.D. thesis](#), University of Basel (2014).
- [125] O. Knopfmacher, *Sensing with Silicon Nanowire Field-Effect Transistors*, [Ph.D. thesis](#), University of Basel (2011).
- [126] D. B. Farmer and R. G. Gordon, *Atomic layer deposition on suspended single-walled carbon nanotubes via gas-phase noncovalent functionalization*, [Nano Letters](#) **6**, 699 (2006).
- [127] F. Kuemmeth, H. Churchill, P. Herring, and C. Marcus, *Carbon nanotubes for coherent spintronics*, [Materials Today](#) **13**, 18 (2010).
- [128] L. Xie, L. Jiao, and H. Dai, *Selective etching of graphene edges by hydrogen plasma*, [J. Am. Chem. Soc.](#) **132**, 14751 (2010).

- [129] R. Yang, L. Zhang, Y. Wang, Z. Shi, D. Shi, H. Gao, E. Wang, and G. Zhang, *An anisotropic etching effect in the graphene basal plane*, [Advanced Materials](#) **22**, 4014 (2010).
- [130] D. Hug, *Zigzag Edges in Graphene and Graphite Defined with a Cold Hydrogen Plasma*, Ph.D. thesis, University of Basel (2013).
- [131] C. Kanai, K. Watanabe, and Y. Takakuwa, *Ab initio calculations on etching of graphite and diamond surfaces by atomic hydrogen*, [Phys. Rev. B](#) **63**, 235311 (2001).
- [132] G. Zhang, P. Qi, X. Wang, Y. Lu, D. Mann, X. Li, and H. Dai, *Hydrogenation and hydrocarbonation and etching of single-walled carbon nanotubes*, [J. Am. Chem. Soc.](#) **128**, 6026 (2006).
- [133] W. Liang, M. Bockrath, and H. Park, *Shell filling and exchange coupling in metallic single-walled carbon nanotubes*, [Phys. Rev. Lett.](#) **88**, 126801 (2002).
- [134] D. H. Cobden and J. Nygård, *Shell filling in closed single-wall carbon nanotube quantum dots*, [Phys. Rev. Lett.](#) **89**, 046803 (2002).
- [135] S. Takei, B. M. Fregoso, H.-Y. Hui, A. M. Lobos, and S. Das Sarma, *Soft superconducting gap in semiconductor Majorana nanowires*, [Phys. Rev. Lett.](#) **110**, 186803 (2013).
- [136] W. Liang, M. Bockrath, D. Bozovic, J. H. Hafner, M. Tinkham, and H. Park, *Fabry-perot interference in a nanotube electron waveguide*, [Nature](#) **411**, 665 (2001).
- [137] M. Field, C. G. Smith, M. Pepper, D. A. Ritchie, J. E. F. Frost, G. A. C. Jones, and D. G. Hasko, *Measurements of coulomb blockade with a noninvasive voltage probe*, [Phys. Rev. Lett.](#) **70**, 1311 (1993).
- [138] S. Kawabata, *Test of Bell's inequality using the spin filter effect in ferromagnetic semiconductor microstructures*, [J. Phys. Soc. Jap.](#) **70**, 1210 (2001).
- [139] P. Samuelsson, E. V. Sukhorukov, and M. Büttiker, *Orbital entanglement and violation of Bell inequalities in mesoscopic conductors*, [Phys. Rev. Lett.](#) **91**, 157002 (2003).
- [140] J. Schnakenberg, *Network theory of microscopic and macroscopic behavior of master equation systems*, [Rev. Mod. Phys.](#) **48**, 571 (1976).

- 
- [141] V. Novotny and P. Meincke, *Single superconducting energy gap in pure niobium*, [Journal of Low Temperature Physics](#) **18**, 147 (1975).
- [142] K. Grove-Rasmussen, H. I. Jørgensen, B. M. Andersen, J. Paaske, T. S. Jespersen, J. Nygård, K. Flensberg, and P. E. Lindelof, *Superconductivity-enhanced bias spectroscopy in carbon nanotube quantum dots*, [Phys. Rev. B](#) **79**, 134518 (2009).
- [143] E. Pallecchi, *Multiwall Carbon Nanotube Josephson Junctions with Niobium Contacts*, [Ph.D. thesis](#), University of Regensburg (2009).
- [144] A. F. Morpurgo, J. Kong, C. M. Marcus, and H. Dai, *Gate-controlled superconducting proximity effect in carbon nanotubes*, [Science](#) **286**, 263 (1999).
- [145] D. R. Schmid, P. L. Stiller, C. Strunk, and A. K. Hüttel, *Magnetic damping of a carbon nanotube nano-electromechanical resonator*, [New Journal of Physics](#) **14**, 083024 (2012).
- [146] B. H. Schneider, S. Etaki, H. S. J. van der Zant, and G. A. Steele, *Coupling carbon nanotube mechanics to a superconducting circuit*, [Sci. Rep.](#) **2**, (2012).
- [147] K. Izydor Wysokiński, *Thermoelectric transport in the three terminal quantum dot*, [Journal of Physics Condensed Matter](#) **24**, 335303 (2012).
- [148] L. Hofstetter, S. Csonka, A. Baumgartner, G. Fülöp, S. d’Hollosy, J. Nygård, and C. Schönenberger, *Finite-bias Cooper pair splitting*, [Phys. Rev. Lett.](#) **107**, 136801 (2011).
- [149] T. S. Jespersen, K. Grove-Rasmussen, J. Paaske, K. Muraki, T. Fujisawa, J. Nygard, and K. Flensberg, *Gate-dependent spin-orbit coupling in multielectron carbon nanotubes*, [Nat. Phys.](#) **7**, 348 (2011).
- [150] J. A. van Dam, Y. V. Nazarov, E. P. A. M. Bakkers, S. de Franceschi, and L. P. Kouwenhoven, *Supercurrent reversal in quantum dots*, [Nature](#) **442**, 667 (2006).
- [151] H. I. Jørgensen, T. Novotný, K. Grove-Rasmussen, K. Flensberg, and P. E. Lindelof, *Critical Current  $0-\pi$  Transition in Designed Josephson Quantum Dot Junctions*, [Nano Letters](#) **7**, 2441 (2007).
- [152] L. C. Venema, J. W. G. Wildöer, J. W. Janssen, S. J. Tans, H. L. J. T. Tuinstra, L. P. Kouwenhoven, and C. Dekker, *Imaging electron wave functions of quantized energy levels in carbon nanotubes*, [Science](#) **283**, 52 (1999).

- [153] W. Klobus, A. Grudka, A. Baumgartner, D. Tomaszewski, S. C., and J. Martinek, *Entanglement witnessing and quantum cryptography with non-ideal ferromagnetic detectors*, arXiv:1310.5640 (2013).
- [154] B. Braunecker, P. Buset, and A. Levy Yeyati, *Entanglement detection from conductance measurements in carbon nanotube Cooper pair splitters*, *Phys. Rev. Lett.* **111**, 136806 (2013).
- [155] R. Lai, H. O. H. Churchill, and C. M. Marcus, *g-tensor control in bent carbon nanotube quantum dots*, arXiv:1210.6402 (2012).
- [156] X. Li, X. Tu, S. Zaric, K. Welsher, W. S. Seo, W. Zhao, and H. Dai, *Selective synthesis combined with chemical separation of single-walled carbon nanotubes for chirality selection*, *J. Am. Chem. Soc.* **129**, 15770 (2007).
- [157] M. Burkhardt, *Carbon nanotubes blockcourse report* (2008), unpublished.
- [158] R. A. López, *Conducting polymers as charge dissipator layers for electron beam lithography*, *Ph.D. thesis*, Friedrich-Alexander-Universität Erlangen-Nürnberg (2006).

## Detailed fabrication recipes

### A.1. Wafer characteristics

- *Substrate material* highly doped Si
- *Dopant* p, boron
- *Resistivity* 0.003 – 0.005  $\Omega\text{m}$
- *Capping layer* 400 nm thermally grown oxide

### A.2. Wafer cleaning

1. Sonicate for 10 min in acetone.
2. Rinse with IPA, blow-dry.
3. 30 min UV ozone cleaning (Model 42-220, Jelight Company, USA).

### A.3. CVD catalyst

The CVD catalyst is made from 3 stock solutions,

- 30 mg of  $\text{Al}_2\text{O}_3$  (particle size: 4 nm) solved in 20 ml IPA
- 93 mg (0.23 mmol) of  $\text{Fe}(\text{NO}_3)_3 \cdot 9\text{H}_2\text{O}$  solved in 20 ml IPA
- 27 mg (0.14 mmol) of  $\text{MoO}_2\text{Cl}_2$  solved in 20 ml IPA

which are sonicated for two hours before 0.5 ml of each solution is mixed and 38 ml IPA are added. Changing the amount of added IPA is an efficient means to tune the CNT density on the wafer. However, we achieved very convenient densities with the give recipe.

In the beginning of my thesis I worked with an alternative recipe: the molybdenum solution ( $\text{MoO}_2\text{Cl}_2$  in IPA) is replaced by a ruthenium solution (48 mg  $\text{RuCl}_3\text{-H}_2\text{O}$  in 20 ml IPA) and growth is carried out at  $850^\circ\text{C}$ . However, it was shown in reference [156] that this recipe yields very narrow CNTs with a diameter distribution centred around 1.1 nm that ranges from 0.7 nm to 1.8 nm. FeMo tubes usually have a wider diameters ranging from 1 nm to 3 nm [156]. During a lab course Markus Weiss and co-workers confirmed that very narrow tubes with less than 1 nm diameter grow from the FeRu catalyst [157] (although the diameter distribution was much wider than in [156]). At the same time experiments show consistently that a smaller diameter correlates with a larger contact resistances [23, 37]. I therefore recommend to use the FeMo catalyst when aiming for a low contact resistance. However, other members of our working group also realized nice devices with the FeRu catalyst.

### A.4. CVD growth

1. Sonicate catalyst solution for 3 h to break up catalysts clusters.
2. Place 1-2 droplets of the catalyst solution onto the already spinning wafer with 4000 rpm.
3. Place wafer in quartz tube of the CVD reactor.
4. Check leak tightness and set the desired flow rates:
  - 1500 sccm for Ar (read 1041/h at the flow meter<sup>1</sup>)
  - 1000 sccm for  $\text{CH}_4$  (read 44.71/h at the flow meter)
  - 500 sccm for  $\text{H}_2$  (read 81/h at the flow meter)
5. Heat furnace to  $950^\circ\text{C}$  under Ar flow.
6. Replace Ar flow by  $\text{CH}_4$  and  $\text{H}_2$  for 10 min.
7. Switch off  $\text{CH}_4$ , leave on  $\text{H}_2$  and switch on Ar.
8. Switch off heating.
9. At  $T < 550^\circ\text{C}$   $\text{H}_2$  flow can also be switched off.
10. Switch off gas flow and take out wafer at  $T < 300^\circ\text{C}$ .

The amount and density of CNTs can vary strongly between different wafers. It is therefore recommended to grow on 3 to 4 wafers in parallel. Before proceeding one can check quickly in the SEM if the growth result was satisfying.

---

<sup>1</sup>The flow meters are gauged for air. When different gases are used one must consider the density of the respective gas to calculate the actual flow rate [103]

## A.5. E-beam lithography

During the duration of this PhD project we tried several resist systems and exposure parameters. Below we will give only one recipe which we believe to be the most suitable for the fabrication of CPS devices.

### Bilayer resist

1. Spin 200 nm PMMA(50K) (AR-P 631.09 from Allresist) diluted in chlorobenzene (4000 rpm, 40 sec, 4 sec ramp).
2. Bake for 2 min on a hot plate at 180°C.
3. Spin 100 nm PMMA(950K) (AR-P 671.09 from Allresist) diluted in chlorobenzene (4000 rpm, 40 sec, 4 sec ramp).
4. Bake for 2 min on a hot plate at 180°C.

The thickness refers to the baked resist and should be checked from time to time. To adjust the thickness one may change the dilution ratio in chlorobenzene or change the frequency of the spinner.

### Exposure

– <i>Used microscopes</i>	Supra 35 and Supra 40 from Zeiss
– <i>Acceleration voltage</i>	20 kV
– <i>Area dose</i>	230 $\mu\text{C}/\text{cm}^2$
– <i>Line dose</i>	950 pC/cm, exposed twice
– <i>Working distance</i>	9 mm or 17 mm
– <i>Aperture (small)</i>	10 $\mu\text{m}$
– <i>Aperture (large)</i>	120 $\mu\text{m}$

### Design guidelines

The specified area dose leads to a significant overexposure and narrow contact strips turn out about 30% wider than designed. Thus, when one aims for a 180 nm wide contact it should be designed with 140 nm width. The intentional overdosing improves the cleanliness of the contact area (see section 4.2).

A specific problem that one may encounter during EBL is posed by abrupt shifts of the e-beam during exposure. This leads to distorted patterns, as shown in Fig. A.1, that are most likely caused by a charging (and sudden decharging) of the PMMA resist (see e.g. [158], p. 12-14). To make the design fault tolerant against such distortions one may define the order in which the different structures (usually rectangles and trapezoids) are exposed. First the small structures that directly contact the tube are written. Since these

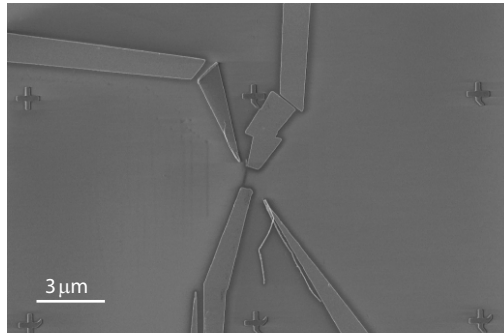


**Figure A.1.:** Example of a structure that is disrupted by sudden jumps of the e-beam position during exposure. These jumps have typical magnitudes of a few hundred of nanometers. By using the ordering function of the Elphy software the design can be made fault tolerant against such jumps.

structures are very small charging effects are negligible. Then one successively proceeds with the surrounding structures which are designed with sufficient overlaps (e.g.  $3\ \mu\text{m}$  overlaps). The Elphy software provides an ordering function for this purpose.

### Development

1. Dip 60 sec into 1:3 mixture of MIBK:IPA.
2. Dip in pure IPA to stop development, blow-dry.



## Solution for the CPS master equation model

In this appendix we provide the Matlab code for the semi-classical master equation model discussed in Chapter 6. The code contains the explicit formulas for the occupation probabilities, calculated with the maximal tree method [140]. From the electronic version of this thesis the code may just be copy-pasted into Matlab.

```
function CPS_master()  
%-----  
% set transition amplitues  
%-----  
p_LPT1 = 0.01; p_LPT2 = 0.01;  
p_N1 = 0.1; p_N2 = 0.1;  
p_CPS= 0.03; p_12_d= 0.001;  
%-----  
% include density of states of the QDs  
%-----  
% define "gate range"  
x=-0.7:0.005:0.7;  
y=-0.7:0.005:0.7;  
[X,Y]=meshgrid(x,y);  
  
% density of states of QD1
```

```

w = 0.05; % set resonance width
rho1=w./(Y.^2+w.^2); % define Lorentzian peak shape
rho1=rho1/max(max(rho1)); % normalize the peak height

% density of states of QD2
w = 0.04;
rho2=w./(X.^2+w.^2);
rho2=rho2/max(max(rho2));

% gate dependend transition probabilities:
p_LPT1=p_LPT1*rho1; p_LPT2=p_LPT2*rho2;
p_CPS=rho1.*rho2*p_CPS; % model assumption
p_N1=p_N1*ones(size(p_LPT1)); p_N2=p_N2*ones(size(p_LPT2));
p_12=rho2.*p_12_d;
p_21=rho1.*p_12_d;

%-----
% calculate occupation probabilities
%-----

Q_00 = p_LPT1.*p_N1.*p_N2 + p_LPT2.*p_N1.*p_N2 ...
      + p_N1.*p_N2.^2 + (p_N1.^2).*p_N2 ...
      + (p_N2.^2).*p_12 + (p_N1.^2).*p_21 ...
      + p_N1.*p_N2.*p_12 + p_N1.*p_N2.*p_21;

Q_01 = (p_LPT2.^2).*p_N1 + p_LPT2.*p_N1.^2 ...
      + p_LPT2.*p_N1.*p_N2 ...
      + p_LPT1.*p_LPT2.*p_N1 + (p_N1.^2).*p_CPS ...
      + p_LPT2.*p_N1.*p_CPS + p_LPT2.*p_N2.*p_12 ...
      + p_LPT2.*p_N1.*p_12 + p_LPT1.*p_N1.*p_12 ...
      + p_LPT1.*p_N2.*p_12 + p_N2.*p_CPS.*p_12...
      + p_N1.*p_CPS.*p_12;

Q_10 = p_LPT1.*p_N1.*p_N2 + p_LPT1.*p_N2.^2 ...
      + (p_LPT1.^2).*p_N2 ...
      + p_LPT1.*p_LPT2.*p_N2 + p_LPT2.*p_N2.*p_21 ...
      + p_LPT1.*p_N2.*p_CPS + p_LPT2.*p_N1.*p_21 ...
      + (p_N2.^2).*p_CPS + p_N1.*p_LPT1.*p_21 ...
      + p_N2.*p_LPT1.*p_21 + p_N1.*p_CPS.*p_21 ...
      + p_N2.*p_CPS.*p_21;

Q_11 = p_LPT1.*p_LPT2.*p_N2 + (p_LPT1.^2).*p_LPT2 ...

```

---

```

+ p_LPT1.*p_LPT2.^2 ...
+ p_LPT1.*p_LPT2.*p_N1 + p_LPT2.*p_N2.*p_CPS ...
+ (p_LPT1.^2).*p_12 + p_LPT1.*p_LPT2.*p_CPS ...
+ p_LPT1.*p_LPT2.*p_21 + p_LPT1.*p_LPT2.*p_12 ...
+ p_N1.*p_N2.*p_CPS + (p_LPT2.^2).*p_21 ...
+ p_N1.*p_LPT1.*p_CPS ...
+ p_N1.*p_CPS.*p_21 + p_N2.*p_CPS.*p_12...
+ p_LPT2.*p_CPS.*p_21 + p_LPT1.*p_CPS.*p_12;

N = Q_00 + Q_01 + Q_10 + Q_11;
Q_00 = Q_00./N;
Q_01 = Q_01./N;
Q_10 = Q_10./N;
Q_11 = Q_11./N;

%-----
% calculate conductances
%-----

G1 = p_N1.*(Q_10 + Q_11);
G2 = p_N2.*(Q_01 + Q_11);

G_CPS=p_CPS.*Q_00;

G_LPT1=p_LPT1.*(Q_01 + Q_00);
G_LPT2=p_LPT2.*(Q_10 + Q_00);

G_12=p_12.*Q_10; % from QD2 to QD1
G_21=p_21.*Q_01; % from QD1 to QD2

ind=find(x==0);
delG2=G2(:,ind)-min(G2(:,ind));
delG1=G1(ind,:)-min(G1(ind,:));
%-----
% plot results
%-----
figure
hold on
plot(x,delG2,'r-')
plot(x,delG1,'b-')
plot(x,G_CPS(:,ind),'g-')

```

```
figure
surface(X,Y,G1); shading flat;
set(gca,'view',[30 60]);
figure
surface(X,Y,G2); shading flat;
set(gca,'view',[30 60]);
```



## Additional data to Chapter 7

In this appendix we discuss the bias dependence of the non-local conductance correlations from Chapter 7. Figure C.1(a,b) shows the simultaneously recorded differential conductances  $G_1$  and  $G_2$  as a function of  $V_{SG2}$  and  $V_{SD}$  at  $V_{BG} = -2.284$  V. The lever-arm of  $V_{SG2}$  to QD1 is about 8 times weaker than to QD2. Therefore the Andreev resonances in Fig. C.1(a) appear very broad and smeared out compared to the Coulomb diamonds in Fig. C.1(b). This separation of energy scales makes it easy to identify conductance correlations  $\Delta G_1(G_2)$ , e.g. the ones indicated by the black arrows in Fig. C.1(a), where a shallow imprint of the left diamond from Fig. C.1(b) is observed. Fig. C.1(c,d) show cross sections at constant bias voltages that demonstrate the sign reversal of  $\Delta G_1(G_2)$  with opposite bias. We note that otherwise the bias dependence of the non-local conductance is surprisingly weak. The intensity of the non-local conductance line is approximately constant between the Andreev resonance and the gap edge. Another intriguing feature in Fig. C.1 is the slightly tilted vertical line, running exactly through the crossing point of the Andreev resonances,  $\pm\zeta = 0$ . Such lines, also visible in the data from reference [56], may be explained as follows. In the region  $|\zeta| \leq |eV_{SD}| \leq |\Delta|$  the Andreev resonance is the only conductance channel and the local current through the device is constant. The two Andreev resonances,  $\zeta$  and  $-\zeta$ , have different conductances. When the two resonances cross, the current through the Andreev channel changes as a step function, yielding a peak in differential conductance. Thus, this line can be interpreted as a finite bias signature of the GS transition. Its slope is given by the capacitive cross-talk from the source contact. However, the

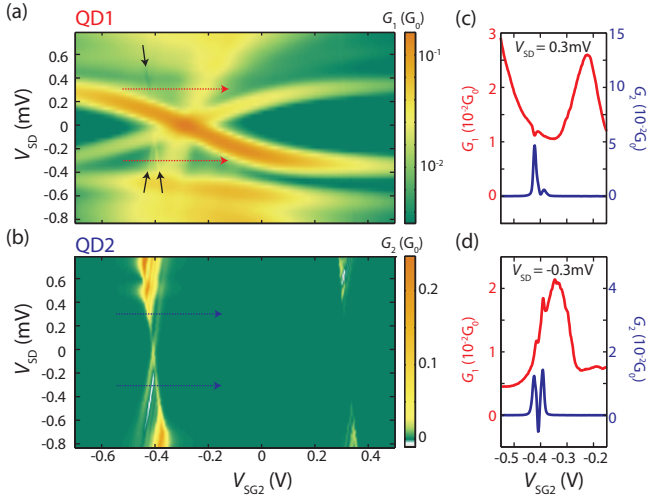


**Figure C.1.:** (a,b) Simultaneously recorded differential conductances  $G_1$  and  $G_2$  as a function of side gate voltage,  $V_{SG2}$ , and source drain bias,  $V_{SD}$ , at  $V_{BG} = -2.284$  V. The black arrows in (a) guide the eye to conductance correlations  $\Delta G_1(G_2)$ . (c) Cross sections of  $G_1$  and  $G_2$  for  $V_{SD} = +0.3$  mV. The large peak in  $G_2$  correlates with a dip in  $G_1$ , i.e. the non-local signal  $\Delta G_1(G_2)$  is negative. (d) Cross section for  $V_{SD} = -0.3$  mV, yielding positive conductance correlations.

reason for the conductance difference between  $\zeta$  and  $-\zeta$ , also observed in [56, 70–72, 101], remains unclear. One possible explanation might be a soft superconducting gap for which quasiparticle states at energies  $E < \Delta$  are available [135]. This scenario would also allow tunnelling processes that break the e-h symmetry of the local sub-gap transport, e.g. the tunnelling of an electron from N1 to QD1 to a quasiparticle state in S. In this case the complete transport cycle,  $GS \rightarrow ES \rightarrow GS$ , has a probability proportional to either  $v^4$  or  $u^4$ .

# Curriculum Vitae

Jens Oliver Schindele  
Born 8 June 1983 in Leimen (Germany)

## Education

- 1989–2002 Primary and secondary school in Osterburken, Mosbach and Heidelberg
- 2003–2009 Studies of physics at the University of Heidelberg
- 07/2009 Diploma in physics at University of Heidelberg  
Diploma thesis in the group of Prof. C. Enss: "Dielectric polarization fluctuations of organic glass formers"
- 2010–2014 PhD in experimental Physics at the University of Basel  
PhD thesis in the group of Prof. C. Schönemberger:  
"Observation of Cooper Pair Splitting and Andreev Bound States in Carbon Nanotubes"

## Civilian service

- 2002–2003 Civilian service at the German Cancer Research Center in Heidelberg

## Positions

- 2009–2010 Research assistant at the *Physikalisches Institut* Heidelberg
- 2010–2014 Teaching assistant for physics at the University of Basel



## Publications

### Publications

- *Fluctuation-Dissipation Theorem in Liquid and Glassy Glycerol: Frequency-Dependent Dielectric Permittivity and Dielectric Polarization Fluctuation Measurements*, J. Schindele, A. Reiser and C. Enss, Phys. Rev. Lett. **107**, 095701 (2011).
- *Near-Unity Cooper Pair Splitting Efficiency*, J. Schindele, A. Baumgartner and C. Schönenberger, Phys. Rev. Lett. **109**, 157002 (2012).
- *Ultraclean Single, Double, and Triple Carbon Nanotube Quantum Dots with Recessed Re Bottom Gates*, M. Jung, J. Schindele, S. Nau, M. Weiss, A. Baumgartner and C. Schönenberger, Nano Lett. **13**, 4522 (2013).
- *Nonlocal Spectroscopy of Andreev Bound States*, J. Schindele, A. Baumgartner, R. Maurand, M. Weiss and C. Schönenberger, Phys. Rev. B **89**, 045422 (2014).

### Talks

- *Was ist Quantum?*  
School lesson at the Leonhard Gymnasium on the occasion of the start of the NCCR QSIT, Basel 23 March 2011
- *Cooper pair splitting with carbon nanotubes*  
Talk at the QSIT junior meeting, Passugg, 24 June 2011

- *Highly efficient Cooper pair splitting with carbon nanotube quantum dots*  
Talk at the DPG spring meeting, Berlin, 26 March 2012
- *Highly efficient Cooper pair splitting with carbon nanotube quantum dots*  
Talk at the SE<sup>2</sup>ND workshop "Spin-orbit Interactions and Entanglement Generation in Solid State Devices", Copenhagen, 2 May 2012
- *Non-local excitations of Andreev bound states*  
Talk at the QSIT Lunch Seminar, ETH Zürich, 4 July 2013.
- *Probing Andreev bound states with a Cooper pair splitter*  
Talk at the Swiss-Japanese nanoscience workshop "Materials Phenomena at Small Scale", Tsukuba, 10 October 2013.

## Poster Contributions

- *Cooper pair splitting with carbon nanotube quantum dots*, J. Schindele, A. Baumgartner and C. Schönenbergerposter, poster at the Next Nano Stars event, Basel, 21 March 2013
- *Cooper pair splitting with carbon nanotube quantum dots*, J. Schindele, A. Baumgartner and C. Schönenbergerposter, poster at the Swiss Nano Convention, Basel, 25 May 2013

## Acknowledgements

First and foremost, I am very grateful to my thesis advisor Christian Schönenberger. There are two attributes which I really admire about him. His enthusiasm, his sharp mind and his nose for things. I know Christian will now speak up and complain that these are actually three attributes – but I just wanted to give a brief demonstration of his mind’s never resting sharpness. He pushed me not with pressure, but with enthusiasm. He guided me not by giving orders, but by asking the right questions and by sharing his experience. It was truly inspiring to work in such an environment and I feel privileged that I had the chance to be a part of his research group.

I would like to thank Prof. Alfredo Levy Yeyati and Dr. Takis Konotos for making the effort to read my thesis. It was a honour to have two so distinguished researchers in my PhD committee. I also thank Andreas Baumgartner for his work on the manuscript of the ”near-unity”-paper and for the time he invested in my PhD project.

A big thanks goes out to Péter Makk for proofreading this thesis, for running with me up to St. Chrischona, for at least trying to properly use his feet when climbing with me and for teasing me to join him doing sport activities on the weekend. Along the same line I have to thank Romain Maurand for being a good friend and an inspiring physicist. It was a great pleasure to ride the passenger seat of your *tracteur*... I am also grateful to Markus Weiss and Minkyung Jung for their support and collaboration.

Science would be no fun at all if there wouldn’t be the fellow scientists. It turns out that the best fellow scientists are located in office 1.25 of Basel’s physics department: Samuel d’Hollosy, Jörg Gramich, Julia Samm, Stefan Nau, Matthias Bräuniger, Gábor Fábíán, Peter Rickhaus, Simon Zihlmann and Clevin Handschin. The same holds for all other members of the na-

noelectronics group: Michel Calame, Wangyang Fu, Gulibusitan Abulizi, Thomas Hasler, Vishal Ranjan, Ralph Stoop, Kishan Thodkar, Anton Vladyka, Mathias Wipf, Samuel Vogel and Cornelia Nef.

I also want to thank some of the people who left the group with a doctoral hat on their heads, while I was still sweating in the lab: Lukas Hofstetter, Hagen Aurich, Jan Brunner, Jón Ágústsson, Frank Freitag, Oren Knopfmacher and Alexey Tarasov. I've had the greatest of times with you.

I also need to mention the fantastic people who work at the department: Astrid Kalt and Barbara Kammermann, who took care of all administrative matters encountered during the last years, Daniel Sacker, with whom I spent countless hours at the BesTec, Dominik Sifrig, who provided me with liquid helium even when I forgot to order beforehand, and Michael Steinacher, who discovered that a Fischer cable at the Kelvinox had a bad shield. By wrapping this cable with aluminium foil he boosted the efficiency of my CPS device to unprecedented values. And before I forget: thank you, Dorothée Hug, for your support with the hydrogen plasma.

My family and friends who supported me throughout the years have also their share of making this work a success and I am very thankful to them.

The greatest discovery I made during my PhD was that I stumbled across you, Nina. When I am with you all the nano science appears as small as it actually is.